



# **NAVAL POSTGRADUATE SCHOOL**

**MONTEREY, CALIFORNIA**

## **THESIS**

**CARBON FIBER AND TUNGSTEN DISULFIDE NANOSCALE  
ARCHITECTURES FOR ARMOR APPLICATIONS**

by

Michael J. Moberg

June 2012

Thesis Advisor:

Second Reader:

Claudia Luhrs

Young Kwon

**Approved for public release; distribution is unlimited**

THIS PAGE INTENTIONALLY LEFT BLANK

<b>REPORT DOCUMENTATION PAGE</b>			<i>Form Approved OMB No. 0704-0188</i>	
Public reporting burden for this collection of information is estimated to average 1 hour per response, including the time for reviewing instruction, searching existing data sources, gathering and maintaining the data needed, and completing and reviewing the collection of information. Send comments regarding this burden estimate or any other aspect of this collection of information, including suggestions for reducing this burden, to Washington headquarters Services, Directorate for Information Operations and Reports, 1215 Jefferson Davis Highway, Suite 1204, Arlington, VA 22202-4302, and to the Office of Management and Budget, Paperwork Reduction Project (0704-0188) Washington DC 20503.				
<b>1. AGENCY USE ONLY (Leave blank)</b>		<b>2. REPORT DATE</b> June 2012	<b>3. REPORT TYPE AND DATES COVERED</b> Master's Thesis	
<b>4. TITLE AND SUBTITLE</b> Carbon Fiber and Tungsten Disulfide Nanoscale Architectures for Armor Applications			<b>5. FUNDING NUMBERS</b>	
<b>6. AUTHOR(S)</b> Michael J. Moberg				
<b>7. PERFORMING ORGANIZATION NAME(S) AND ADDRESS(ES)</b> Naval Postgraduate School Monterey, CA 93943-5000			<b>8. PERFORMING ORGANIZATION REPORT NUMBER</b>	
<b>9. SPONSORING /MONITORING AGENCY NAME(S) AND ADDRESS(ES)</b> N/A			<b>10. SPONSORING/MONITORING AGENCY REPORT NUMBER</b>	
<b>11. SUPPLEMENTARY NOTES</b> The views expressed in this thesis are those of the author and do not reflect the official policy or position of the Department of Defense or the U.S. Government. IRB Protocol number ____N/A____.				
<b>12a. DISTRIBUTION / AVAILABILITY STATEMENT</b> Approved for public release; distribution is unlimited			<b>12b. DISTRIBUTION CODE</b>	
<b>13. ABSTRACT (maximum 200 words)</b>  <p>The objective of this research was to generate shock-resistant materials based on inorganic fullerene type tungsten disulfide (IF-WS<sub>2</sub>) and carbon nanocomposite structures for personal protection armor systems. The aim was to develop a new generation of composites that combine the known energy absorbing properties of carbon nanofibers, with the shock absorbing properties reported for IF-WS<sub>2</sub> structures. Various methods were explored to generate the desired WS<sub>2</sub>-carbon fiber composite. Experimentation revealed that in situ growth of carbon fibers from a nickel catalyst with tungsten disulfide particulates had to be performed from particular precursors and fabrication conditions to avoid undesirable byproducts that hinder fiber growth. As a result, tungsten oxide was used as tungsten source, nickel as carbon fiber growth catalyst, ethylene as hydrocarbon and fuel rich oxidative conditions for growth, all followed by a sulfurization process. Fabrication of fibers was performed at moderate temperatures (ca. 550 degrees C) with a sulfurization step at 900 degrees C in a tubular furnace.</p> <p>Microstructural characterization of the samples was primarily conducted using X-ray diffraction and electron microscopy. In order to determine more properties of the nanocomposites, the samples were dispersed into an epoxy matrix. Nano-indentation was utilized as a method of determining mechanical properties of the composites while a gas gun was used to determine shock propagation effects. The inclusion of WS<sub>2</sub>/C nanocomposites into epoxy matrixes showed a significant improvement in modulus and hardness values when compared to bare carbon fiber epoxy composites. WS<sub>2</sub>/C fiber epoxy nanocomposites preserved their integrity during gas gun tests while samples without WS<sub>2</sub> fractured.</p>				
<b>14. SUBJECT TERMS</b> Tungsten Sulfide, Nanocomposite, Carbon Nanofiber, Nanoindentation, Shock Testing, Armor			<b>15. NUMBER OF PAGES</b> 121	
			<b>16. PRICE CODE</b>	
<b>17. SECURITY CLASSIFICATION OF REPORT</b> Unclassified	<b>18. SECURITY CLASSIFICATION OF THIS PAGE</b> Unclassified	<b>19. SECURITY CLASSIFICATION OF ABSTRACT</b> Unclassified	<b>20. LIMITATION OF ABSTRACT</b> UU	

THIS PAGE INTENTIONALLY LEFT BLANK

**Approved for public release; distribution is unlimited**

**CARBON FIBER AND TUNGSTEN DISULFIDE NANOSCALE  
ARCHITECTURES FOR ARMOR APPLICATIONS**

Michael J. Moberg  
Ensign, United States Navy  
B.S.M.E., United States Naval Academy, 2011

Submitted in partial fulfillment of the  
requirements for the degree of

**MASTER OF SCIENCE IN MECHANICAL ENGINEERING**

from the

**NAVAL POSTGRADUATE SCHOOL  
June 2012**

Author: Michael J. Moberg

Approved by: Associate Professor Claudia Luhrs  
Thesis Advisor

Distinguished Professor Young Kwon  
Second Reader

Professor Knox Millsaps  
Chair, Department of Mechanical and Aerospace Engineering

THIS PAGE INTENTIONALLY LEFT BLANK

## ABSTRACT

The objective of this research was to generate shock-resistant materials based on inorganic fullerene type tungsten disulfide (IF-WS<sub>2</sub>) and carbon nanocomposite structures for personal protection armor systems. The aim was to develop a new generation of composites that combine the known energy absorbing properties of carbon nanofibers, with the shock absorbing properties reported for IF-WS<sub>2</sub> structures. Various methods were explored to generate the desired WS<sub>2</sub>-carbon fiber composite. Experimentation revealed that in situ growth of carbon fibers from a nickel catalyst with tungsten disulfide particulates had to be performed from particular precursors and fabrication conditions to avoid undesirable byproducts that hinder fiber growth. As a result, tungsten oxide was used as tungsten source, nickel as carbon fiber growth catalyst, ethylene as hydrocarbon and fuel rich oxidative conditions for growth, all followed by a sulfurization process. Fabrication of fibers was performed at moderate temperatures (ca. 550 degrees C) with a sulfurization step at 900 degrees C in a tubular furnace.

Microstructural characterization of the samples was primarily conducted using X-ray diffraction and electron microscopy. In order to determine more properties of the nanocomposites, the samples were dispersed into an epoxy matrix. Nano-indentation was utilized as a method of determining mechanical properties of the composites while a gas gun was used to determine shock propagation effects. The inclusion of WS<sub>2</sub>/C nanocomposites into epoxy matrixes showed a significant improvement in modulus and hardness values when compared to bare carbon fiber epoxy composites. WS<sub>2</sub>/C fiber epoxy nanocomposites preserved their integrity during gas gun tests while samples without WS<sub>2</sub> fractured.

THIS PAGE INTENTIONALLY LEFT BLANK



## TABLE OF CONTENTS

<b>I.</b>	<b>INTRODUCTION.....</b>	<b>1</b>
<b>A.</b>	<b>BODY ARMOR AND THE UTILITY OF SPECIFICALLY TAILORED NANOSCALE ARCHITECTURES.....</b>	<b>1</b>
1.	The Development of Personal Protective Systems .....	1
2.	Nanoparticles and Architectures .....	4
a.	<i>Carbon Nanotubes and Nanofibers.....</i>	<i>4</i>
b.	<i>Tungsten Disulfide.....</i>	<i>5</i>
3.	Thesis Outline.....	7
<b>II.</b>	<b>CARBON NANOFIBER AND WS<sub>2</sub> NANOPARTICLE SYNTHESIS AND CHARACTERIZATION METHODS.....</b>	<b>11</b>
<b>A.</b>	<b>SYNTHESIS OF NANOSTRUCTURES.....</b>	<b>11</b>
1.	Carbon Nanofibers.....	11
a.	<i>Growth of Carbon Nanofibers in the Presence of Oxygen ...</i>	<i>12</i>
b.	<i>Synthesis of Carbon Nanofibers in the Absence of Oxygen.....</i>	<i>13</i>
2.	Tungsten Disulfide .....	14
a.	<i>Decomposition of an Ammonium Tetrathiotungstate Precursor .....</i>	<i>14</i>
b.	<i>Sulfurization of a Tungsten Oxide Precursor.....</i>	<i>15</i>
<b>B.</b>	<b>SYNTHESIS OF NANOPARTICLE COMPOSITES .....</b>	<b>16</b>
1.	Synthesis of Carbon Nanofibers <i>in situ</i> with Tungsten Disulfide ..	17
2.	Synthesis of Carbon Nanofibers <i>in situ</i> with Tungsten Oxide and Subsequent Sulfurization .....	18
<b>C.</b>	<b>SAMPLE PREPARATION FOR MECHANICAL TESTING .....</b>	<b>20</b>
1.	Preparation of Carbon Nanofiber and Tungsten Disulfide Pellets .....	21
2.	Mounting Nanomaterials into an Epoxy Matrix.....	22
a.	<i>Mixing an Epoxy Matrix with Dispersed Nanomaterials.....</i>	<i>22</i>
b.	<i>Finishing Processes for Epoxy Matrixes .....</i>	<i>23</i>
<b>D.</b>	<b>CHARACTERIZATION METHODS AND OPERATING CONDITIONS.....</b>	<b>25</b>
1.	X-Ray Diffraction.....	26
2.	Scanning Electron Microscopy .....	26
3.	Thermogravimetric Analysis .....	28
4.	Surface Area Analysis by BET Gas Adsorption .....	28
<b>III.</b>	<b>PROCEDURES FOR MECHANICAL TESTING OF NANOPARTICLES AND NANOPARTICLE COMPOSITES IN AN EPOXY MATRIX.....</b>	<b>31</b>
<b>A.</b>	<b>NANO-INDENTATION.....</b>	<b>32</b>
1.	Background of Nano-Indentation.....	33
2.	Operating Conditions and Summary of Experimental Data Acquisition .....	37

B.	HIGH SHOCK (GAS GUN) TESTING.....	38
1.	Background of Gas Gun Testing .....	38
2.	Operating Conditions .....	41
IV.	RESULTS ANALYSIS AND DISCUSSION .....	45
A.	EXAMINATION AND DISCUSSION OF NANOPARTICLES AND NANOPARTICLE COMPOSITES .....	45
1.	Growth and Characterization of Carbon Nanofibers .....	45
a.	<i>Comments about Nickel Nanoparticle Catalyst</i> .....	45
b.	<i>Carbon Nanofibers Synthesized in the Presence of Oxygen</i> .....	48
c.	<i>350-Degree Carbon Growth Step</i> .....	50
d.	<i>Carbon Nanofibers Synthesized in the Absence of Oxygen</i> ..	55
2.	Characterization of Tungsten Disulfide.....	56
a.	<i>Commercial Tungsten Disulfide</i> .....	57
b.	<i>Synthesis of Tungsten Disulfide</i> .....	58
3.	Synthesis of Nanoparticle Composites .....	59
a.	<i>Carbon Nanofibers in situ with Tungsten Disulfide</i> .....	60
b.	<i>Sulfurized Carbon Nanofibers with a Nickel Nanoparticle Catalyst</i> .....	67
c.	<i>Sulfurized Carbon Nanofibers with Tungsten Oxide in situ with a Nickel Nanoparticle Catalyst</i> .....	69
4.	TGA Testing .....	74
5.	Sample Selection for Continued Testing.....	75
B.	SAMPLES FOR MECHANICAL TESTING .....	76
a.	<i>Carbon Nanofiber and Tungsten Disulfide Pellets</i> .....	76
b.	<i>Mounting Nanomaterials into an Epoxy Matrix</i> .....	77
C.	MECHANICAL TESTING OF NANOPARTICLES AND NANOPARTICLE COMPOSITES IN AN EPOXY MATRIX.....	80
1.	Nanoindentation.....	80
a.	<i>Flat Punch Complex Modulus</i> .....	80
b.	<i>Modulus and Hardness at Depth</i> .....	82
2.	Gas Gun Testing.....	86
V.	CONCLUSIONS .....	93
VI.	RECOMMENDATIONS FOR FUTURE RESEARCH.....	95
	LIST OF REFERENCES .....	97
	INITIAL DISTRIBUTION LIST .....	101

## LIST OF FIGURES

Figure 1.	Illustration of the various regimes in the breakdown of ceramic armor after insult with a ballistic penetrator. After [2].	2
Figure 2.	A computer simulation of a projectile impacting a ballistic fabric from the Army High Performance Computing Research Center. The fabric deforms on impact and fails when the stress waves reach the fixed connections. From [3].	3
Figure 3.	Transmission electron microscopy image of the formation of graphitic lattice planes on a carbon nanofiber.	5
Figure 4.	Transmission electron microscopy image of tungsten disulfide inorganic fullerenes. It is possible to see the hollow interior of the particle as well as the layers that comprise the onion like structure. From [13].	6
Figure 5.	Transmission electron microscopy image of tungsten disulfide inorganic fullerenes after exposure to 21 GPa shock pressure. The broken edges of the structure are indicated with arrows. From [14].	7
Figure 6.	The thesis outline flowchart. This chart will be used to indicate the aspect of the thesis being discussed. This section provides justification of the thesis topic.	9
Figure 7.	The Lindberg Blue M Tube Furnace utilized for synthesis of carbon nanofibers.	11
Figure 8.	This section of the research discusses the carbon nanofiber synthesis.	12
Figure 9.	This section will discuss the tungsten disulfide synthesis processes.	14
Figure 10.	This section discusses the <i>in situ</i> growth of nanocomposites.	16
Figure 11.	The Branson Ultrasonic Corporation Model 2510R-MTH Sonicator utilized to sonicate the tungsten oxide precursor and nickel nanoparticle catalyst.	18
Figure 12.	Eppendorf Model 5418 Centrifuge utilized to extract the precursor and catalyst for the nanocomposite synthesis.	19
Figure 13.	A flow diagram of the carbon fiber and tungsten disulfide composite synthesis.	20
Figure 14.	This section discusses the process of mounting the nanocomposites for the purpose of mechanical testing.	21
Figure 15.	The Struers Specifix 20 mounting epoxy kit used to create composites with the carbon nanofibers and tungsten disulfide spheres. Also depicted are the cups used to mix the epoxy prior to pouring and the one and one quarter inch diameter molds used for curing the samples.	22
Figure 16.	Epoxy pucks formed using the outlined method and one weight percent loading. The puck on the left contains nanoparticles while the sample on the right is pure epoxy. The upper surfaces of both samples have been ground and polished for nanoindentation.	24
Figure 17.	An image depicting the internal structure of the sample holders.	25
Figure 18.	This section outlines characterization techniques.	25
Figure 19.	This section discusses mechanical testing techniques.	32

Figure 20.	A generalized load versus displacement curve generated by nanoindentation. Stiffness can be seen to be the slope of the initial unloading curve. From [22]. ....	33
Figure 21.	A summary of nanoindentation tips. Images collected from [23]. ....	34
Figure 22.	A picture of the gas gun setup. The breech is smaller cylinder on the right and the sample holder is the larger vessel on the left side of the barrel. From [26]. ....	39
Figure 23.	The left case is the slug moving prior to impact while the right case is the state at impact. The speeds are represented symbolically as arrows and the shock is represented by a series of arcs. ....	40
Figure 24.	The Hugoniot plot for an aluminum-aluminum interaction. The shock is represented as the line with a positive slope, while the rarefaction is mirrored around the impedance match state. ....	42
Figure 25.	The Hugoniot plot for an aluminum-aluminum and epoxy interaction. The shock is the line with a positive slope, while the rarefaction is mirrored around the impedance match state. The additional line represents the epoxy and the intersection with the rarefaction curve gives the shock pressure. ....	43
Figure 26.	This section characterizes the carbon nanofibers synthesis. ....	45
Figure 27.	SEM image of commercial nickel nanoparticles. These particles formed large agglomerations as seen in the top left image. Some particles were micron scale, such as the sphere shown in the top right image, but the majority were on the scale of 100 nm as seen in the bottom image. ....	47
Figure 28.	Carbon nanofibers grown from a nickel nanoparticle catalyst. The left image shows the inclusion of larger micron size fibers while the right image shows the smaller fibers on the order of 10 nm. ....	50
Figure 29.	SEM images depicting the impact of sintering on the nickel catalyst when heated to a temperature of 350 degrees Celsius. ....	51
Figure 30.	SEM images of nickel nanoparticles after FIB milling. The full trapezium can be seen in the left image and the refinements to upper surface can be seen in the right image. ....	52
Figure 31.	Images of the FIB milled surface taken with the SEM. These images show the porosity of the agglomeration as well as the structure of the included particles. The vertical lines are a result of the FIB milling. ....	53
Figure 32.	EDX of a region of the FIB milled surface. Nickel is the dominant element in this spectrum, but traces of oxygen and carbon are also shown. The lower SEM image indicates the region where the analysis was conducted. ....	54
Figure 33.	EDX of a region of the FIB milled surface. This spectrum shows a much higher incidence of carbon as well as nickel and traces of oxygen. The lower SEM image indicates the point where the analysis was conducted. ....	55
Figure 34.	This section characterizes the tungsten disulfide synthesis. ....	57
Figure 35.	SEM image of commercially purchased tungsten disulfide. The particles have a microstructure resembling large platelets. ....	58

Figure 36.	Offset XRD patterns from two different syntheses of tungsten disulfide. The lower came from tungsten oxide while the upper came from ammonium tetrathiotungstate.....	59
Figure 37.	This section will discuss the characterization of nanoparticle composites.....	60
Figure 38.	XRD pattern from the carbon growth with commercial tungsten disulfide. While the tungsten disulfide and nickel catalyst are still present, tungsten oxide and nickel sulfide are also present. ....	61
Figure 39.	The binary phase diagram for nickel and sulfur. In the range of experimentation, nickel and sulfur will form into a nickel sulfide. Phase diagram courtesy of ASM Alloy Phase Diagrams Center. From [29]. ....	62
Figure 40.	EDX illustrating the presence of nickel sulfide. ....	63
Figure 41.	EDX illustrating the presence of tungsten sulfide. ....	64
Figure 42.	EDX illustrating the manner of formation of nickel sulfide from a tungsten disulfide particle.....	65
Figure 43.	SEM images of nickel sulfide formations. The left image shows the agglomeration on sintered spherical nickel particles with nanoparticles in the background while the right image shows the nickel sulfide formation on sintered platelets of nickel particles. ....	66
Figure 44.	A flow diagram of the carbon fiber and tungsten disulfide composite synthesis. ....	67
Figure 45.	SEM images of sulfurized carbon nanofibers grown with a nickel nanoparticle catalyst. The left image shows the fiber distribution, while the right image shows the inclusion of a different type of nickel sulfide. ....	68
Figure 46.	XRD pattern from carbon fibers and the sulfurized carbon fibers. While the predominant peaks are from the carbon nanofibers, two forms of nickel sulfide are also present. ....	69
Figure 47.	XRD patterns for each of the three loadings of tungsten disulfide and carbon nanofibers. The bottom line has the highest loading, the middle line the middle loading, and the upper line the lowest loading. ....	71
Figure 48.	SEM images from the three different loadings of tungsten sulfide. The upper left image is the highest loading, the upper right image is the middle loading, and the lower image is the lowest loadings. ....	72
Figure 49.	SEM image of tungsten disulfide particles present in the composite with the loaded loading of tungsten disulfide particles.....	73
Figure 50.	SEM image showing the variability of the morphology of the tungsten disulfide particles. ....	74
Figure 51.	TGA analysis of pure carbon fibers, sulfurized fibers, and the tungsten disulfide and carbon fiber nanocomposite. All three are thermally stable until approximately 500 degrees Celsius. ....	75
Figure 52.	A discussion of nanocomposite mounting methods.....	76
Figure 53.	The attempt to form epoxy pucks with a three weight percent loading of nanoparticles. In this case the epoxy did not set correctly. The left image demonstrate the harder region of semi-set epoxy. The surface of puck in the right image shows a high density of carbon fibers and an unset epoxy.....	78

Figure 54.	This section will discuss the mechanical testing of the mounted nanocomposites.....	80
Figure 55.	The loss modulus at a frequency of 6.708 Hz. The scale is normalized to the pure epoxy which has the largest loss factor of two percent. ....	81
Figure 56.	The elastic modulus from the basic modulus and hardness testing. The scale is normalized to the pure epoxy. ....	84
Figure 57.	The hardness from the basic modulus and hardness testing. The scale is normalized to the pure epoxy.....	85
Figure 58.	An image of the deform aluminum sample holder. The surface was initially flat, and the ring on the surface is a result of the displacement of metal from the impact of the 480 gram slug traveling at 370 meters per second. ....	88
Figure 59.	Images of the epoxy slices with only carbon nanofibers, left, and sulfurized nanofibers, right, fired upon in the gas gun. The surfaces show signs of impact and provide information about the relative effectiveness of the nanocomposites. ....	88
Figure 60.	Images of the lowest and highest loadings of tungsten disulfide from left to right, respectively. The surface of the lowest loading shows little damage while the highest loading is heavily cracked. ....	89
Figure 61.	The upper image illustrates the crack that formed on the edge of the slice with the lowest loading of tungsten disulfide. The lower image illustrates the difference in the crack patterns found on cracks that reached the edge of the highest loading. ....	90

## LIST OF TABLES

Table 1.	Summary of nanocomposite loadings by weight percent. The highest loading has the most tungsten disulfide, 3% while the middle and lowest loadings have 1.6% and 0.7%, respectively.....	20
----------	---	----

THIS PAGE INTENTIONALLY LEFT BLANK



## **LIST OF ACRONYMS AND ABBREVIATIONS**

Å - Angstroms

BET - Surface area measurement based on Brunauer, Emmett and Teller gas adsorption theory

CNF - Carbon Nanofiber

CNT - Carbon Nanotube

FIB - Focused Ion Beam

GPa - Gigapascal

IF - Inorganic Fullerene

kV - Kilovolts

mm - Millimeter

nm - Nanometer

RPM - Rotation per Minute

sccm - Standard Cubic Centimeters per Minute

SEM - Scanning Electron Microscopy/Microscope

TEM - Transmission Electron Microscope

TGA - Thermogravimetric Analysis

TPa - Terapascal

UHP - Ultra High Purity

WS<sub>2</sub> - Tungsten Disulfide

XRD - X-Ray Diffractometry/Diffractometer

THIS PAGE INTENTIONALLY LEFT BLANK

## ACKNOWLEDGMENTS

First and foremost, I would like to thank Professor Luhrs for all of her assistance in this process. I spent many hours in her office discussing processes, techniques, and sifting through results. Without her guidance it is safe to say that I would not have been able to accomplish the goals this research set out to achieve.

I would also like to thank Professor Kwon for his assistance in forming this document into its final shape as a second reader.

Thank you to the Office of Naval Research for providing the support required to complete this research.

Throughout this process, Professor Menon was also a continuing source of assistance. With his help I was trained to use a number of characterization techniques and he was even willing to spend the time to revive the TEM and offer the capabilities of the FIB.

Professor Brewer's assistance was essential to the determination of results for this research. His training on nanoindentation as well as the time he took to help verify the results of the testing was greatly appreciated. Jennifer Hay at Agilent Technologies was also instrumental in providing the programs needed to conduct testing.

I would like to thank Professor Hooper and the students in the gas gun lab, especially LTJG Patrick Smith, for their assistance in explaining the principles of shock propagation and for conducting testing of various samples.

I would also like to offer thanks to LTJG Ashley Maxson, Dr. Park, and the rest of the NPS faculty and staff for always being willing to offer a word of advice or a helping hand throughout the thesis process.

Finally, thank you to my fiancée, ENS Rebecca King, and to my family for being a source of support and sanity during many late nights working in the Watkins Hall computer lab.

THIS PAGE INTENTIONALLY LEFT BLANK

# **I. INTRODUCTION**

## **A. BODY ARMOR AND THE UTILITY OF SPECIFICALLY TAILORED NANOSCALE ARCHITECTURES**

### **1. The Development of Personal Protective Systems**

There is a current and ongoing pursuit of lightweight and strong materials to be used in armor. The history of metallic plate armor used to protect the human body dates back to the 5th century, while the design and materials evolved through the middle ages and the Renaissance [1]. While these methods functioned to deflect swords and maces for the legions of Rome and the medieval knights of Europe, they are no longer viable in the era of high velocity penetrators. Current technology relies on the independent use or combination of ceramic or metal plates and high strength fabrics. In order to make further advancements, it will be necessary to view the issue of personal protection systems from a nanoscale perspective.

Ceramic armor is in many ways a technological continuation of the same methodologies used in ancient plate armor. As an armor plate is impacted by a projectile it must absorb or dissipate the incident kinetic energy. In the past, the hardest and strongest materials available were bronze and iron, but as technology advanced more sophisticated materials have been developed. The field is now dominated by oxides and carbides such as alumina, boron carbide, silicon carbide, and titanium diboride [2]. While these materials are far harder than their predecessors, there is a tradeoff in fracture toughness, or the material's ability to resist fracture once a crack has formed. As a result, it has become necessary to add a backing layer with higher ductility than the ceramic. In many ceramic armors, the ceramic plate is adhered to the ductile layer to improve overall properties, but at the same time the interactions between the materials can also lead to failure. When a penetrator impacts a ceramic plate, the shock wave from the impact propagates through the material, reaching the backing plate. While part of the energy is dissipated at the plates' interface, a portion of the energy is deflected by the backing plate causing more damage during the return propagation into the ceramic than the direct

contact with the penetrator (Figure 1). The shock waves that begin to propagate through the hard ceramic when impacted with a projectile travels at a different speed than in the ductile backing. While the initial shock wave compresses the material, this difference in propagation speeds directs a series of tensile waves back into the ceramic. These tensile waves often cause the ceramic to crack and fail, preying on the inherent deficiencies in fracture toughness and tensile strength of the material [2].

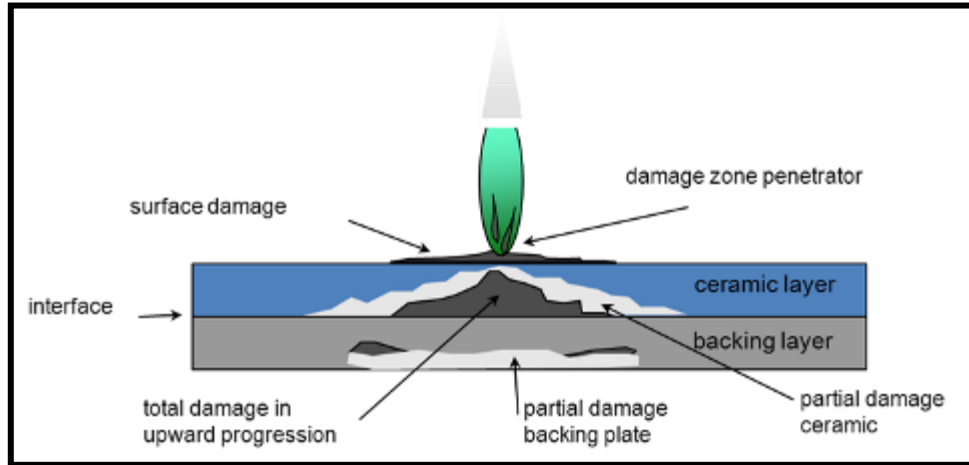


Figure 1. Illustration of the various regimes in the breakdown of ceramic armor after insult with a ballistic penetrator. After [2].

A different approach to providing protection has come in the form of ballistic fabrics. While ceramic armor serves to stop a projectile through hardness, ballistic fibers act to dissipate the energy of the projectile. When a projectile impacts a fabric, the energy is transmitted in the form of stress waves along the length of the fiber. As the stress wave moves down a fiber some of the energy is transmitted to each of the fibers in contact with the affected fiber as a result of the fabric weave. The energy is also dissipated by friction in between the fiber as they try to move within the weave as a result of the force of the projectile. This process will often cause the first layers of fabric impacted to be penetrated, but as the projectile continues to impact additional layers, more and more of the energy is dissipated until it is finally brought to a stop (Figure 2).

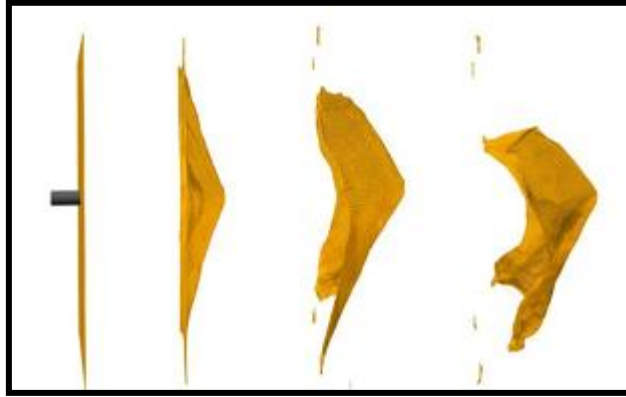


Figure 2. A computer simulation of a projectile impacting a ballistic fabric from the Army High Performance Computing Research Center. The fabric deforms on impact and fails when the stress waves reach the fixed connections. From [3].

In both approaches, there is a significant concern with blunt force trauma to whatever lies behind the armor material. In the case of personnel armor, the transmission of force and shock waves through the armor can still cause damage to the wearer even if the projectile is stopped. Blunt trauma to the human body can result in injuries to skeletal and muscular structures as well as damage to internal organs. This process is mainly a factor of the deformation of the armor and the transmission of shock waves into the human body. In order to combat this phenomenon, there has been interest in nanoscale materials and architectures. By synthesizing materials at the nanometer scale, it is possible to carefully control the architecture of the particles. The coinciding synthesis of multiple particles from combined catalysts, or thorough mixing of preformed components, creates the possibility to form a nanoscale co-continuous composite. Co-continuous composites offer unique collections of properties including stiffness, impact resistance, and strength while at the same time maintaining the ability to dissipate energy. Most notably, co-continuous composites provide a balance of stiffness and energy absorption, properties that are not well balanced in particle or fiber reinforced composites [4]. It has also been shown that the high energy absorption is a product of the durability of the material as many small cracks develop at the junction in between the different particles in the composite, absorbing energy but arresting prior to the development of a

critical flaw size. Two materials that are of particular note for strength and energy absorption and dissipation are carbon nanotubes/nanofibers and inorganic fullerene tungsten disulfide.

## **2. Nanoparticles and Architectures**

### ***a. Carbon Nanotubes and Nanofibers***

Carbon nanotubes, and closely related carbon nanofibers offer some of the highest strength to weight ratios found in all engineering materials. A carbon nanotube is comprised of carbon arranged in a graphitic crystal structure that has curled and interconnected, forming a cylinder. These tubes are hollow in the middle and can have any number of graphitic rings, or walls. The diameters of these tubes can range from nanometers to tens of nanometers, or even microns, depending on the conditions the tubes developed in and the number of walls. Due to the extremely small size of these particles, assessment of the mechanical properties has been difficult, and the determination of properties for the material has relied on methods such as thermal vibration analysis and atomic force microscopy. The average Young's modulus for multiwall carbon nanotubes has been experimentally determined to be 1.8 TPa [5, 6]. While carbon nanotubes are usually only microns in length, it is possible to spin the fibers into a yarn that maintains much of the theoretical strength of the tubes. Further research has studied the impact on a carbon nanotube from a small diamond bullet to determine the viability of use in ballistic fabric. This testing illustrated the incredible energy absorbing characteristics of the material, and it was determined that in order to completely stop a 9 mm bullet a total of 6 layers of woven nanotube yarn would be required. The total thickness of such armor would only be 600 microns [7]. While carbon nanotubes offer outstanding properties, carbon nanofibers also have a modulus on the order to 800 GPa [6]. Nanofibers are similar to nanotubes, but instead of having ideally connected curled graphitic sheets they are comprised of stacked graphitic layers which form into fibers (Figure 3). Despite the reduction in modulus, fibers are easier to synthesize and can offer other benefits to the development of ballistic armor.



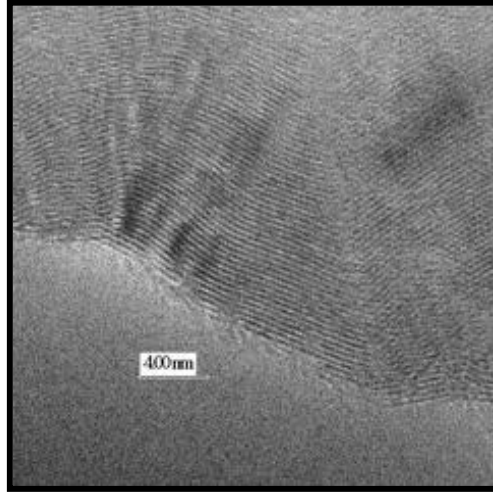


Figure 3. Transmission electron microscopy image of the formation of graphitic lattice planes on a carbon nanofiber.

Depending on the operating conditions, and the precursor used to catalyze the growth, the size of the nanofibers can be controlled. There are myriad possibilities for different sized fibers in armor applications, but there are three that are the most promising. The first possibility is to use large, several hundred nanometer diameter or even micron diameter carbon fibers. The next possibility is the growth of small, tens of nanometer diameter, carbon fibers. These smaller fibers can form a tight three dimensional mesh with the surrounding fibers, holding the armor sample together. The final possibility is the combination of large and small fibers. The combination of fiber size appears especially interesting as it will capitalize on all of the benefits of both of the other possibilities. Further, a varied particle size will help to attenuate shock propagation reducing the plausibility of blunt force trauma.

#### ***b. Tungsten Disulfide***

After the discovery of carbon based organic fullerene structures, it was originally thought that the phenomenon was specific to carbon. The existence of an inorganic fullerene material made of elements other than carbon was first proposed in 1992 by Tenne and coworkers [8, 9, 10, 11, 12]. Among the materials proposed to form such a structure was tungsten disulfide. In addition to the spherical structures, many

multi-layer polyhedra were found to form of tungsten disulfide nanostructure including sheets, cages, tubes, and fibers [13]. Since that time, tungsten disulfide and a host of other materials have been shown to form inorganic fullerene structures. The form of the spherical inorganic fullerenes is similar to that of a hollow onion. The metal sulfides bond into a sheet which forms a roughly spherical, hollow shape (Figure 4). This process is usually achieved by the sulfurization of a metal oxide precursor whose initial shape influences the shape of the formed sulfides. These closed-hollow structures have a number of properties that can be exploited for use in a variety of applications.

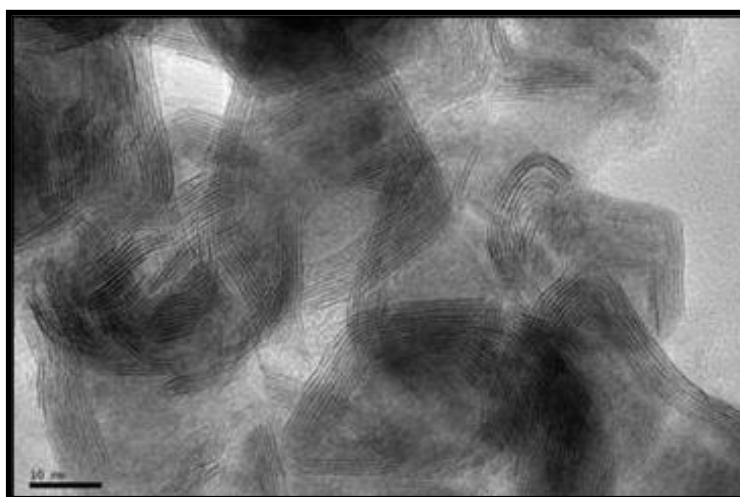


Figure 4. Transmission electron microscopy image of tungsten disulfide inorganic fullerenes. It is possible to see the hollow interior of the particle as well as the layers that comprise the onion like structure. From [13].

One of the most common uses for inorganic fullerenes is as a solid lubricant. Each of the layers forming the fullerene is only loosely attached to the layers above and below by secondary bonding with covalent bonding in plane. The application of shear stress will cause a surface layer to be sloughed off preventing wear on the lubricated component. Further, the shape of the fullerenes can prevent further wear from occurring. The natural spherical shape of the particles causes them to function as nanometric ball bearings rolling with the motion of the components. The excellent mechanical properties of the fullerene prevents them from flattening and breaking down as they roll until a number of surface layers have been removed [8]. It has also been

shown that multilayer tungsten disulfide polyhedra have outstanding shock resistance properties superior to those of even carbon nanotubes [14]. In order to determine the shock absorbing characteristics, a tungsten disulfide powder was exposed to shock pressures of 21 and 35 GPa. Transmission electron microscopy was used to analyze the particles after impact to determine the level of damage to the polyhedra. While the particles were crushed at 36 GPa, the majority of the tungsten disulfide structures were intact after exposure to 21 GPa. Damage to the structure was noted on the edges where small groups of planes had fractured and began to separate from the bulk particle (Figure 5). At the same 21 GPa shock pressure, carbon nanotubes were crushed and began to reform into diamond [14]. The ability to absorb shock and maintain integrity after high shock loading is essential in a material used in a personal protective armor, and the incorporation of inorganic fullerenes into a nanocomposite could serve to further limit the likelihood of trauma over pure carbon nanotubes.

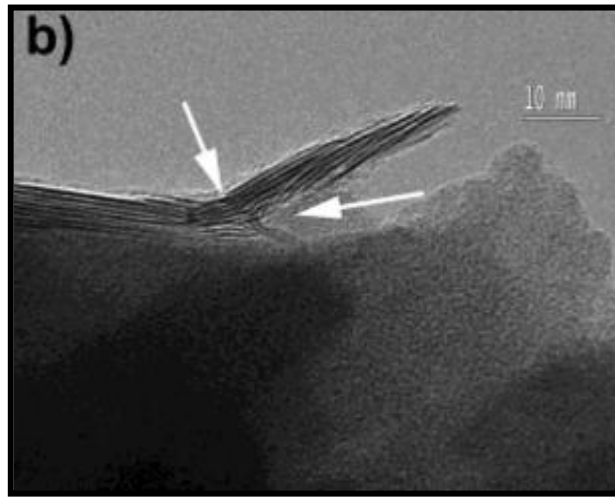


Figure 5. Transmission electron microscopy image of tungsten disulfide inorganic fullerenes after exposure to 21 GPa shock pressure. The broken edges of the structure are indicated with arrows. From [14].

### 3. Thesis Outline

The focus of this research was to generate materials for personal protection through the inclusion of shock wave absorbing materials based on inorganic fullerene

tungsten disulfide and carbon composite structures. The aim was to develop a new generation of nanocomposites that combine the mechanical properties known of carbon nanofibers, with the shock absorbing properties reported for inorganic fullerene type tungsten disulfide structures. Emphasis was placed on designing a material that will dissipate the shock waves after impact. Rather than stopping a penetrator, which can be successfully achieved with other means, this material will be designed to help prevent blunt force trauma. The research was highly experimental and as a result, many processes were attempted in order to generate a thorough understanding of the operative mechanisms. The objective of the research was to synthesize a specifically engineered composite able to maintain its integrity while dissipate lingering shock fronts or pressure waves by mechanisms related to the specific particulate structures (CNF and WS<sub>2</sub>) and effects of their mixed granularity. In order to accomplish this pursuit, it was necessary to develop a number of synthesis protocols for both of the constituent particles as well as the nanocomposite. These protocols relied on the appropriate balance of atmosphere, temperature treatment, and the correct processing of the precursors. Additional protocols were developed to prepare the samples for testing using different instrumentation. The testing and analysis of the data for the nanocomposite would also be essential to draw relevant conclusions about the applicability of these materials in future personal protection systems.

The hypothesis to test: The integration of carbon nanofibers with tungsten disulfide nanoparticles in a composite will result in a material with improved shock dissipating properties over the individual components.

This thesis outlines the entirety of the steps taken to develop and characterize a series of new nanocomposites. Chapter II, Carbon Nanofiber And WS<sub>2</sub> Nanoparticle Synthesis And Characterization Methods, discusses the processes and operating conditions employed for the synthesis of the desired nanoparticles and outlines the characterization techniques used to develop an understanding of the synthesized materials. This section also explains the methodology for the selection of the samples that were used for final testing. Chapter III, Procedures for Mechanical Testing of Nanoparticles and Nanoparticle Composites In An Epoxy Matrix, reviews the approaches

used to prepare and mechanically test the selected samples in order to determine the material properties. The following section, Chapter IV, discusses the results from the characterization and mechanical testing of materials. It also presents a comparative study to determine which sample had the best overall performance and attempts to explain why this sample performed better than others. The final portions of the paper, Chapter V, summarize the results of the research and make recommendations for future research.

The basic aspects of the research can be found in flow chart form in Figure 6. In order to provide continuity throughout the thesis, the aspect of the research being addressed in a given section will be indicated by using this flow chart. The aspect that is being addressed will be indicated by shading.

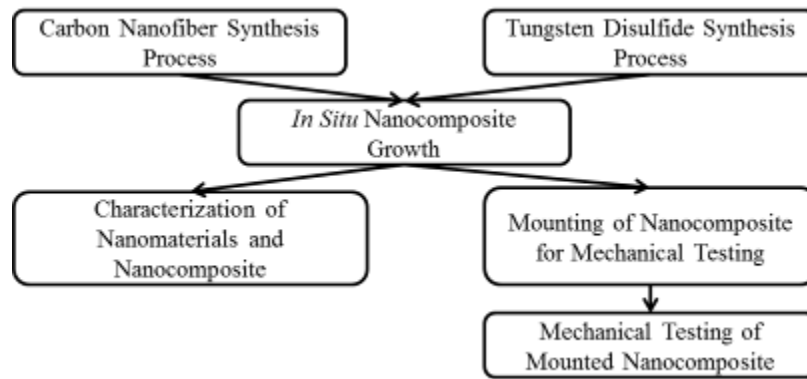


Figure 6. The thesis outline flowchart. This chart will be used to indicate the aspect of the thesis being discussed. This section provides justification of the thesis topic.

THIS PAGE INTENTIONALLY LEFT BLANK

## **II. CARBON NANOFIBER AND WS<sub>2</sub> NANOPARTICLE SYNTHESIS AND CHARACTERIZATION METHODS**

### **A. SYNTHESIS OF NANOSTRUCTURES**

The synthesis of nanoparticles took place in a Lindberg Blue M 1200 degree Celsius tubular furnace with a single point temperature control (Figure 7). The bore size was one inch outside diameter and the heated length was 12 inches. A one inch outside diameter quartz tube was placed into the bore of the furnace. Stainless steel fittings with a high temperature O-rings were used to close the system and provide a one quarter inch inlet for gases used during experiments. All syntheses were performed using controlled atmospheres. The gas flows were measured with Matheson flow meters and provided with an initial pressure of 20 psi from gas cylinders.



Figure 7. The Lindberg Blue M Tube Furnace utilized for synthesis of carbon nanofibers.

#### **1. Carbon Nanofibers**

For each batch of carbon nanofibers produced, 50 mg of nickel nanopowder (Sigma Aldrich catalog number 577995–5G, particle size less than 100 nm and a 99% pure trace metal bias) was used as catalyst. Nickel particles were contained in a sintered

alumina combustion boat (Coors, 10 ml). The combustion boat was placed into the center of the quartz tube and the quartz tube was positioned into the furnace ensuring that the furnace thermocouple was centrally located under the sample. The furnace was closed and the fittings were connected to each end of the quartz tube. Through these fittings, a series of metered gasses were passed over the sample. The initial step in the synthesis was to purge the system with nitrogen gas (Praxair, UHP). The system was purged for a minimum of 20 minutes with a flow rate of 300 sccm of nitrogen. The general steps for the carbon nanofiber synthesis followed the methodology previously published by our research group (Figure 8) [15].

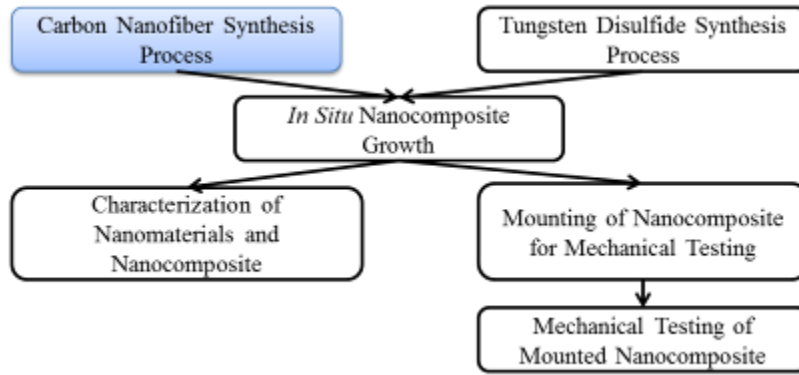


Figure 8. This section of the research discusses the carbon nanofiber synthesis.

*a. Growth of Carbon Nanofibers in the Presence of Oxygen*

After a period of 20 minutes and maintaining the flow of nitrogen used to purge the system, the furnace temperature was increased to 350 degrees Celsius [10]. Once the desired temperature was achieved, a mixture of 98% argon and 2% hydrogen gas (Praxair, UHP) was introduced with a flow rate of 37 sccm of argon to ensure that nickel particles were in a metallic state and no traces of nickel oxide were present. Once the flow of argon-hydrogen gas was initiated, the nitrogen flow was stopped. The flow of argon-hydrogen was maintained at 350 degrees Celsius for a period of 60 minutes.

At the conclusion of 60 minutes the flow of argon-hydrogen gas was terminated and the flow of nitrogen gas was resumed at the reduced value of 44 sccm.



For the growth, a fuel rich atmosphere was created with ethylene. The flow of ethylene gas was maintained at 15 sccm of ethylene. Additionally, a flow of oxygen gas at a flow rate of 2 sccm of oxygen was introduced to the system. The aforementioned flows are maintained at 350 degrees Celsius for a period of 15 minutes. After 15 minutes, the temperature is increased to 550 degrees Celsius. The amount of time that the sample was left in this growth environment was variable. Most syntheses were run for a period of 45 minutes, however for larger yield syntheses this step was extended to 90 minutes.

After the desired length of time, the oxygen and then ethylene gas were turned off. At this point, the furnace was also turned off allowing the system to return to room temperature. The flow of nitrogen gas was maintained until the system had returned to a temperature below 100 degrees Celsius in order to deter any chemical reactions in between the sample and the atmosphere. Small, electric fans were placed on the sides of the furnace in order to pass cool ambient air over the ends of the quartz tube. This additional air flow served to remove heat from the tube, expediting the cooling process. Once the sample had cooled, the nitrogen flow was stopped and the sample was carefully removed and collected from the combustion boat.

#### ***b. Synthesis of Carbon Nanofibers in the Absence of Oxygen***

Another method of synthesizing carbon nanofibers, a variation of a method previously published by Atwater et al. that used palladium instead of a nickel catalyst in a hydrogen environment was also investigated [16]. As before, a measured quantity of nickel nanopowder was placed into a combustion boat and loaded into the tube furnace. The fittings were connected to the ends of the quartz tube and the system was purged with nitrogen for a minimum of 20 minutes at a flow rate of 300 sccm of nitrogen. After a period of 20 minutes and maintaining the flow of nitrogen, the furnace temperature was increased to 350 degrees Celsius. Once the system reached 350 degrees Celsius, a mixture of 98% argon, and 2% hydrogen gas, at a flow rate of 37 sccm of argon was initiated and the flow of nitrogen was halted. For 30 minutes the flow of argon-hydrogen was maintained at a temperature of 350 degrees Celsius.

After 30 minutes under argon-hydrogen, the flow of nitrogen was resumed at the rate of 300 sccm of nitrogen. The flow of argon-hydrogen gas was increased to 50 sccm of argon. In order to provide carbon to the system, ethylene was added at a flow rate of 15 sccm of ethylene. These flow rates were maintained at 350 degrees Celsius for a period of 15 minutes. After 15 minutes had elapsed, the furnace temperature was increased to 550 degrees Celsius for a period of 45 minutes. At the end of 45 minutes, the ethylene and argon-hydrogen gasses were secured. The flow of nitrogen was maintained and the furnace was turned off allowing the system to cool. The nitrogen flow was stopped after the furnace reached a temperature below 100 degrees Celsius and the sample was carefully removed and collected from the combustion boat.

## 2. Tungsten Disulfide

Although tungsten disulfide was a commercially available powder (Sigma Aldrich the lot number S36006–366 with 99% purity), syntheses were conducted to produce nanoparticles given the need to utilize a smaller particle size. As a result, two additional methods were followed in order to synthesize tungsten disulfide from various precursors (Figure 9).

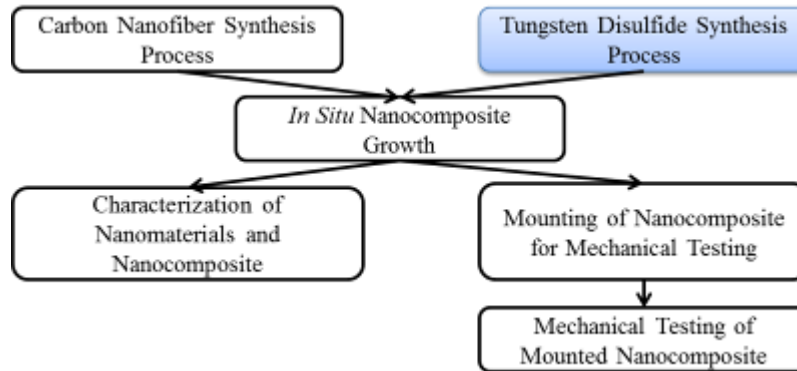


Figure 9. This section will discuss the tungsten disulfide synthesis processes.

### a. *Decomposition of an Ammonium Tetrathiotungstate Precursor*

The first method developed to create tungsten disulfide nanoparticles was to decompose an ammonium tetrathiotungstate precursor similar to research found in

[17]. The commercially available ammonium tetrathiotungstate was obtained from Sigma-Aldrich under the lot number 3162500–50 in a crystalline form with a 99.9% pure trace metal basis. In order to produce the desired tungsten disulfide, it was necessary to decompose the ammonium from the tetrathiotungstate and to reduce the excess sulfur.

Procedurally, the ammonium tetrathiotungstate was placed into a combustion boat, which was then placed inside of the quartz tube in the furnace. After connecting the fittings to the end of the quartz tube, the system was purged with nitrogen gas for a minimum of 20 minutes with a flow rate of 300 sccm of nitrogen. The temperature of the furnace was then increased to 550 degrees Celsius. Once the furnace reached the specified temperature, a mixture of 98% argon and 2% hydrogen gas was introduced at a flow rate of 37 sccm of argon. After a period of 120 minutes, the argon-hydrogen gas was stopped and the nitrogen gas flow was resumed. At this point the furnace was also shut down and the sample was allowed to cool in the presence of nitrogen gas. In order to prevent the possibility of tungsten oxide forming, the sample was cooled under nitrogen until it reached room temperature conditions. Once the sample was fully cooled, it was removed from the furnace and the contents of the combustion boat were carefully collected.

#### ***b. Sulfurization of a Tungsten Oxide Precursor***

Another method to synthesize tungsten disulfide was to sulfurize tungsten oxide (Sigma-Aldrich lot number 550086–5G particle size less than 100 nm). To ensure the smallest possible particle size, the powder was ground in a mortar and pestle for a period of 15 minutes. The ground tungsten oxide powder was removed from the mortar and then loaded into a combustion boat. Once the sample was loaded, the combustion boat was placed inside of the quartz tube and placed into the furnace.

In order to sulfurize the sample, it was necessary to obtain a source of sulfur. The source selected for this study was hydrogen sulfide gas [13, 18, 19]. Due to the hazardous nature of hydrogen sulfide, additional preparations were made to reduce the risk of the gas escaping into the laboratory. These preparations entailed passing the exhausted gasses through two different solutions to scrub out any hydrogen sulfide. The

first scrubber used had a 5–10% concentration of sodium hypochlorite in the form of commercially available Clorox Bleach. The second solution was comprised of two grams of potassium permanganate dissolved in 100 mL of water. Once the gas had passed through the scrubbing solutions it was vented into the fume hood.

Once the pipe fittings were connected to the ends of the quartz tube and the system was purged with nitrogen gas at 300 sccm of nitrogen for a minimum of 20 minutes. After 20 minutes had elapsed, the furnace temperature was raised to 900 degrees Celsius. Once the temperature was reached, the flow of nitrogen was reduced to 150 sccm of nitrogen and the flow of hydrogen sulfide gas was started at a rate of 15 sccm of hydrogen sulfide. The system was then left to run for 60 minutes. At the conclusion of 60 minutes, the hydrogen sulfide gas was secured and the furnace was turned off allowing the nitrogen to continue flowing. As with the previous synthesis method, the nitrogen was allowed to run until the sample had reached room temperature before being removed from the furnace in order to prevent oxidation.

## B. SYNTHESIS OF NANOPARTICLE COMPOSITES

Once the methodology for the synthesis of each of the individual nanoparticles had been determined, it was necessary to determine a process for *in situ* growth (Figure 10).

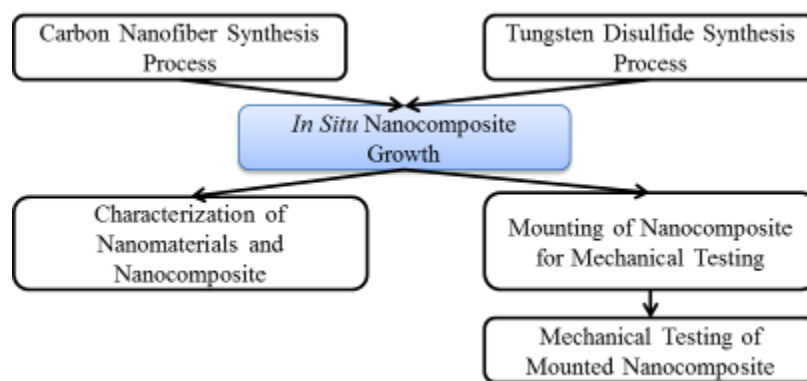


Figure 10. This section discusses the *in situ* growth of nanocomposites.

## 1. Synthesis of Carbon Nanofibers *in situ* with Tungsten Disulfide

The protocol for the synthesis of the carbon nanofibers *in situ* with tungsten disulfide had two variants. Each variant was determined by the source of the tungsten disulfide. The first used the commercially derived tungsten disulfide obtained from Sigma Aldrich. The second utilized the synthesis procedure from the decomposition of ammonium tetrathiotungstate.

The growth procedure for the nanocomposite with the *in situ* tungsten disulfide was quite similar to the normal procedure for the carbon nanofiber growth with only the nickel nanoparticle catalyst. At the onset, quantities of nickel nanoparticles and the commercial tungsten disulfide were measured and then added together into the mortar. In order to ensure that uniform distribution and reduced particles sizes were present in the sample, the combination of the two materials were ground in the mortar with a pestle for a period of 10 minutes. This mixture was removed from the mortar and placed into a combustion boat which was subsequently loaded into the quartz tube and then the furnace. From this point forward, the procedure followed is identical to that used in section II.A.1.a.

In the second synthesis, the process for deriving tungsten disulfide from ammonium tetrathiotungstate was revisited. The first step in this process was to measure quantities of the ammonium tetrathiotungstate and the nickel nanoparticles. These materials were placed into a mortar and then ground together for a period of 10 minutes in order to reduce particle size and the ensure uniform distribution. Once the sample had been ground, it was removed from the mortar and placed into a combustion boat which was placed inside of the quartz tube in the furnace. The rest of the procedure follows that found in section II.A.1.a.

It should be noted that the procedure in section II.A.2.a. outlines that the sample be placed into an argon-hydrogen gas for a period of 120 minutes in order to decompose the ammonium tetrathiotungstate precursor, while the procedure used only leaves the sample in the environment for a period of 60 minutes. This alteration in favor of consistency with the carbon nanofiber growth process is a result of later analysis of the

decomposed ammonium tetrathiotungstate. Based on this analysis, it was concluded that the smaller amount of ammonium tetrathiotungstate precursor present in the growth step would completely decompose within the 60 minute time frame allotted in the growth process.

## **2. Synthesis of Carbon Nanofibers *in situ* with Tungsten Oxide and Subsequent Sulfurization**

The procedure for the synthesis of carbon nanofiber *in situ* with tungsten oxide is closely akin to that of the procedure used for tungsten sulfide. There are some key procedural differences in the methods used to ensure a uniform distribution. The tungsten oxide samples required the additional step of sulfurizing in order to synthesize the appropriate tungsten disulfide. In order to grow the carbon nanofibers *in situ* with the tungsten oxide, it was necessary to measure a quantity of the tungsten oxide and the nickel nanoparticle catalyst. Tungsten oxide was placed into a mortar and was ground for a period of 10 minutes. Once ground, the tungsten oxide was mixed with the nickel particles using a spatula. The subsequent mixture was then transferred into a test tube and the minimal amount of ethanol required to form a solution with the particles was added. This test tube was then sealed and placed inside of a Branson Ultrasonic Corporation model 2510R-MTH Sonicator (Figure 11). The test tube was sonicated for a period of 10 minutes. Once 10 minutes had elapsed, the test tube was removed from the sonicator and placed into a centrifuge.



Figure 11. The Branson Ultrasonic Corporation Model 2510R-MTH Sonicator utilized to sonicate the tungsten oxide precursor and nickel nanoparticle catalyst.

The centrifuge used was an Eppendorf Model 5418 Centrifuge (Figure 12). Once the sample was placed into the centrifuge, an identical test tube to the one holding the sample was placed in the opposite position in the centrifuge in order to maintain balance in the system. The sample was centrifuged for a period of three minutes at a speed of 5000 RPM. After the centrifuge had completed its operations, the test tube was removed and the majority of the separated ethanol was extracted with a pipette and discarded. The sample was then removed from the bottom of the test tube with a spatula and placed onto a glass dish. A small amount of ethanol was added back into the test tube in order to aid in the removal of any remaining mixture from the test tube.



Figure 12. Eppendorf Model 5418 Centrifuge utilized to extract the precursor and catalyst for the nanocomposite synthesis.

After the sample was placed onto a glass dish, it was placed into a Thermo Scientific Model 3510 L-C Oven. The oven was maintained at a temperature of 80 degrees Celsius in order to evaporate any of the remaining ethanol. The sample was left in the oven for approximately 20 minutes, or until the sample had completely dried. The glass dish was then removed from the oven and allowed to cool to room temperature before the sample was removed and placed into a combustion boat. The synthesis from this point forward consists of the procedure outline in section II.A.1.a. After this process was completed, the procedure from section II.A.2.b. was executed. At the completion of this procedure, the sample was removed from the furnace and the contents of the

combustion boat were collected. This entire process is summarized in Figure 13. This research varied the loading of tungsten disulfide while maintaining a constant weight of nickel nanopowders. Three different loading of tungsten disulfide were used for characterization and mechanical testing (Table 1).

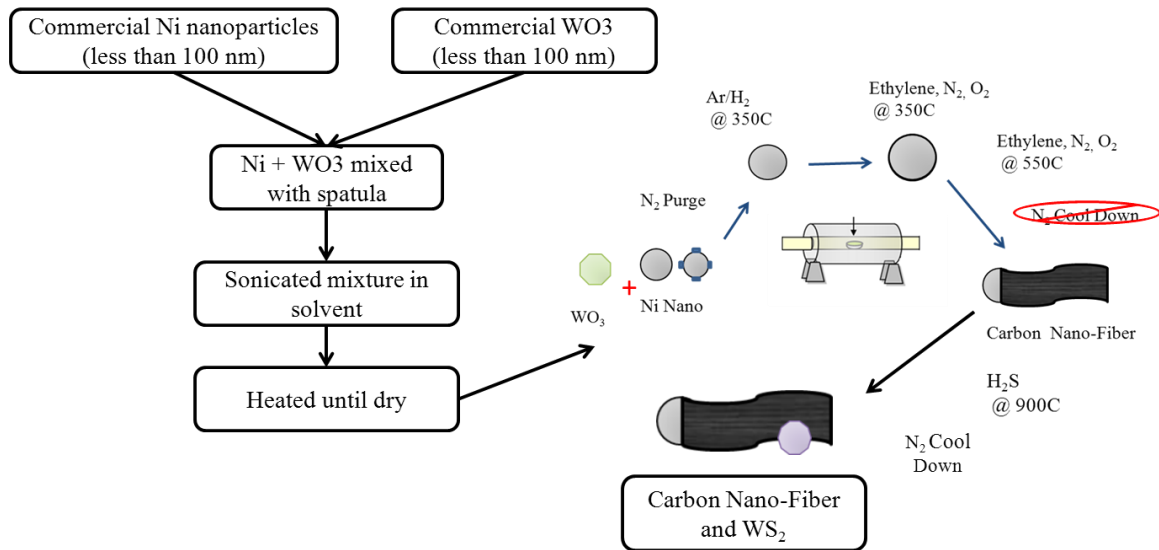


Figure 13. A flow diagram of the carbon fiber and tungsten disulfide composite synthesis.

Carbon Fiber and Tungsten Disulfide Nanocomposite Composition by Weight Percent			
	Carbon Fibers	Nickel	Tungsten Disulfide
<b>Highest Loading</b>	94%	3%	3%
<b>Middle Loading</b>	94.6%	3.2%	1.6%
<b>Lowest Loading</b>	96.4%	2.9%	0.7%

Table 1. Summary of nanocomposite loadings by weight percent. The highest loading has the most tungsten disulfide, 3% while the middle and lowest loadings have 1.6% and 0.7%, respectively.

### C. SAMPLE PREPARATION FOR MECHANICAL TESTING

For all of the mechanical analysis conducted, it was necessary to establish a method to form the nanocomposites into a state conducive to mechanical testing. The



selected mechanical testing methods, or instrumented indentation, and high shock testing required a bulk material. In order to meet the operating requirements of the testing apparatuses, procedures were developed for the compression of the nanocomposites into pellets and the more practical option of dispersing the nanocomposites into an epoxy matrix (Figure 14).

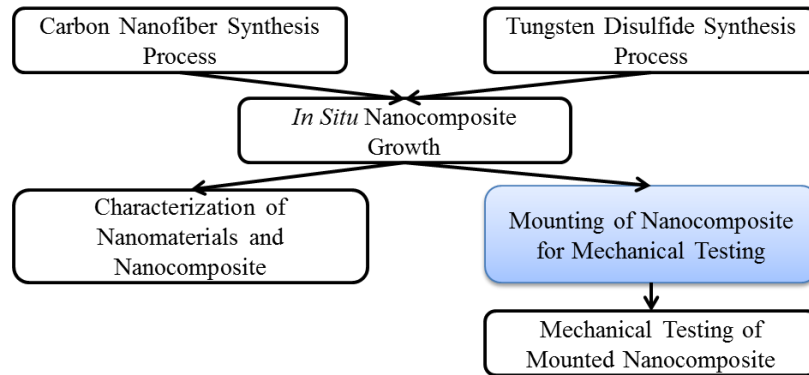


Figure 14. This section discusses the process of mounting the nanocomposites for the purpose of mechanical testing.

### 1. Preparation of Carbon Nanofiber and Tungsten Disulfide Pellets

One approach was to form the nanocomposite into a pellet to be used for further testing. A pellet die designed to create a pellet of 13 mm in diameter and with a thickness of 2 mm was loaded with the nanocomposite. After being loaded into the pellet die, the powder was subjected to a series of increasing pressures in the attempt to form a solid pellet. In order to apply the appropriate pressure, a hydraulic press was used. Three pressures were used to form pellets, 40 MPa, 45 MPa, and 50 MPa. In each case, the press was pressurized and then maintained for a period of three minutes. At the conclusion of three minutes, the pressure was relieved and the die was removed. After carefully disassembling the die, the pellet was removed.

## 2. Mounting Nanomaterials into an Epoxy Matrix

### *a. Mixing an Epoxy Matrix with Dispersed Nanomaterials*

The epoxy selected for use was the commercially available Struers Specifix-20 (Figure 15). The general use for this epoxy is sample mounting, and as such was appropriate for this research. Specifix-20 is a two part epoxy consisting of a resin and a hardening agent. By volume, the ratio of epoxy to resin is 26:5. A beneficial factor about the epoxy is the curing method. Unlike some epoxies that require heating or pressure, this epoxy is designed to cure under atmospheric conditions. Further, it has a working period of 60 minutes, allowing time for the sample to be handled and nanocomposite added and mixed prior to the onset of curing.



Figure 15. The Struers Specifix 20 mounting epoxy kit used to create composites with the carbon nanofibers and tungsten disulfide spheres. Also depicted are the cups used to mix the epoxy prior to pouring and the one and one quarter inch diameter molds used for curing the samples.

In order to form the epoxy samples, the required volume of the resin was measured and placed in a mixing cup. The hardening agent was then measured via pipette and added into the resin. When first mixed, the hardener causes the resin to transition from a clear liquid to one that is cloudy. At this point, the two components were mixed

together by manual agitation using the end of the plastic pipette used to add the hardener. Once the mixture had regained in clear appearance, the sample, still inside of the cup to prevent water from coming into contact with the epoxy, was placed into the sonicator. The epoxy was then sonicated for a period of three minutes.

At the conclusion of three minutes, the epoxy was treated in one of two ways. If the intent was to create a pure epoxy sample, it was poured into a one and one quarter inch diameter mold (Figure 15). If a nanomaterial or composite was to be added into the epoxy, then the appropriate amount of sample was added and returned to the sonicator. For a period of five minutes, the nanoparticle and epoxy composite was left to sonicate with occasional stirring using the pipette as before. After the five minutes had concluded, the sample was poured into a mold. Once the epoxy had been placed into a mold, it was left for a period of at least 24 hours to cure into a hard puck. A loading of 1.0% nanoparticles to 99% epoxy by weight was selected for testing.

***b. Finishing Processes for Epoxy Matrixes***

After the nanoparticles were successfully embedded into the epoxy matrix, it was still necessary to prepare the surface of the samples for testing. During the epoxy curing process, many of the samples hardened with large scratches across the surface or even voids were air bubbles had settled. Instrumented indentation requires a flat, level surface in order to provide accurate results. As a result, the surface of the epoxy pucks were ground and polished to provide a suitable surface. Each of the pucks was first ground on wetted 240-grit sandpaper. The puck was then ground on wetted 320-, 400-, and finally 600-grit sandpaper. After grinding, the pucks were polished using a one micron and then 0.05 micron polishing solution. The pucks were used for instrumented indentation in this state (Figure 16).

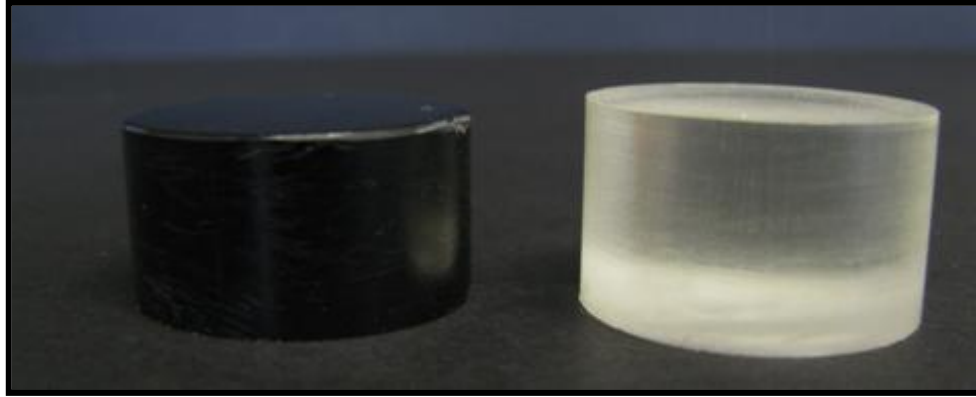


Figure 16. Epoxy pucks formed using the outlined method and one weight percent loading. The puck on the left contains nanoparticles while the sample on the right is pure epoxy. The upper surfaces of both samples have been ground and polished for nanoindentation.

In order to make samples of an adequate size for use in high shock testing, it was necessary to reduce the height of the epoxy puck. While the tall epoxy pucks were beneficial for use in the equipment utilized in instrumented indentation, a narrow disk was best suited to shock propagation. As a result, after the epoxy pucks were tested with nanoindentation, they were sectioned using a diamond saw. The first four millimeters of the upper surface was removed and maintained in the event that more indentation was required. The next four millimeters were cut out of the material for further use. The four millimeter slice was then carefully ground using the same progression of sandpaper grits in the aforementioned polishing process to ensure uniform thickness. A mirror polish was not required, and as a result, the samples were only briefly finished on a one micron polishing wheel.

Once the epoxy slices were adequately finished, sample holders were machined for use in high shock testing. Due to the nature of the shock waves produced, the sample holders are severely deformed and can only be used once. As a result, the holders are machined to the exact specifications of the samples. In order to prevent the loss of material, the epoxy slices were enclosed within a sample holder with a front surface thickness of five millimeters. The sample holders used in this research were constructed from 6061 Aluminum (Figure 17).



Figure 17. An image depicting the internal structure of the sample holders.

#### D. CHARACTERIZATION METHODS AND OPERATING CONDITIONS

Once the process of synthesizing a material was complete, it was necessary to characterize the resultant product. There are myriad ways to characterize a material depending on the properties that are desired. For the purposes of this research, the most important factors for characterization were the identification of phases contained in the materials and the analysis of the size and shape of the constituent nanoparticles. Another area of interest was the thermal stability and possible phase transition present in the nanocomposite. As a result, the three main characterization methods selected were X-ray diffraction, scanning electron microscopy, and thermo-gravimetric analysis (Figure 18).

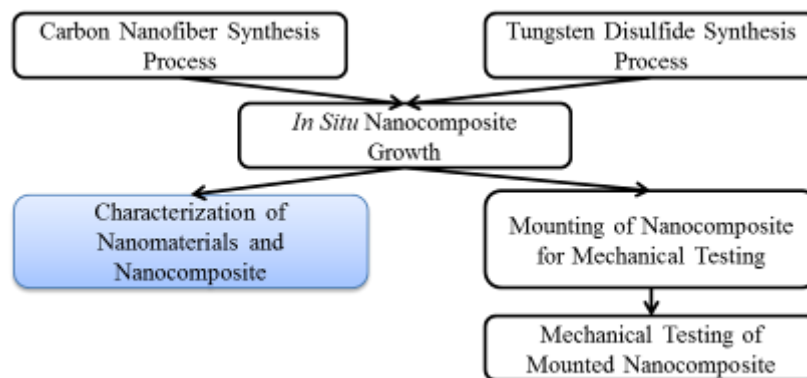


Figure 18. This section outlines characterization techniques.

## **1. X-Ray Diffraction**

X-Ray diffraction (XRD) is a characterization method that determines the crystal structure of a given sample. While XRD is commonly used to determine composition, it only does so by comparing an observed crystal system to a database of known materials and their corresponding crystal systems. In general, XRD diffraction starts when a current is passed through an X-ray tube and is incident on a metal source. Within the X-ray tube, electrons are knocked out of the inner valences of the metal source and as outer valence electrons change into a lower energy shell X-ray radiation is emitted. These X-rays are then directed into contact with a sample. As the sample is irradiated, the incident radiation is diffracted, a detector counts the number of X-rays at a given angle of incidence, or  $2\text{-}\Theta$  angle. The number of counts and the angle at which they occur can be translated into the crystallographic planes present in the material. Once the planes and the locations of each plane are known, the crystal lattice type and dimensions are determined and the sample can be identified [20].

The XRD utilized was a Philips 1830 Analytical X-Ray. The X-ray tube contained a copper source and the X-rays utilized had a primary wavelength, or K-Alpha, of  $1.54 \text{ \AA}$ . The XRD took place over a  $2\text{-}\Theta$  angle ranging from five to 70 degrees. The step size in between each measurement was 0.020 degrees and the time at each step was one second. The samples were placed into a silicon low background sample holder. This low background holder does not contain crystal planes that diffract within the range of the analysis, and as a result will not produce an observable influence in the data. The electrical current used to generate x-rays was set to a value of 30 mA, and the voltage was set to 35 kV.

## **2. Scanning Electron Microscopy**

Scanning electron microscopy (SEM) is a method of viewing the surface of a sample with high magnification using a beam of electrons. An electron gun is located at the top of a column above the sample to be reviewed. The electron gun uses either a tungsten filament, lanthanum hexaboride filament, or a field emission gun to generate the electron beam. The energy contained in the electron beam is dictated by the potential

applied to a series of plates near the electron gun. Commonly used voltages range from 2 kV to 30 kV, but potentials outside of this range can be used as well. The beam is controlled inside of the column using a series of lenses and electromagnetic coils to focus the beam and eliminate scattered electrons. The successfully directed and focused beam is then placed at a specific point on the surface of the sample [20].

When the electron beam is incident on the sample, a number of electrons are scattered, diffracted, or transmitted through the material. In this research, only a few of the different types of electrons were utilized for analysis. In order to obtain information about the surface of the sample, secondary electrons were used. Secondary electrons are electrons that are ejected from the orbit of a sample atom as a result of the incident electrons. These electrons have a much lower energy than the incident beam but contain important information about the contours of the surface. Another mode of detection is very closely related to the generation of secondary electrons. When an electron is displaced from its position in an orbital, an electron from a higher energy state will move to the lower energy state. This change in energy will result in the emission of an X-ray that is characteristic to the orbital conditions of a particular atom. By collecting these X-rays, it is possible to identify the elements present in a SEM sample. This process is known as energy dispersive X-ray spectroscopy (EDX), and is useful to identify the presence of an element even though it cannot identify structure like XRD analysis [20].

The same lenses and coils used to focus the electron beam can also be used to focus a beam of ions. The focused ion beam (FIB) is comprised of accelerated gallium ions. A pool of liquid gallium is located inside of the SEM and a tungsten filament is placed into the pool to ionize the material. These ions are accelerated away from the pool by establishing a potential. For this research, the potential was set at a value of 30 kV. The accelerated gallium ions are routed into the column and are focused onto the surface of a material. As the ions impact the surface, the surface material is pushed away making it possible to mill the surface of the sample with nanometer scale control. By varying the amperage supplied to the system the number of ions can be controlled allowing the

removal of the surface material to be controlled with varying levels of precision. This process can be useful for analysis of surface layers or exposing the internal structure of hollow particles.

In this research, a Zeiss Neon 40 SEM was utilized for characterization. Each of the samples was attached to the surface of an aluminum sample holder with double sided carbon tape. Once the sample was ready, it was placed under vacuum overnight to allow the sample to degas. A field emission gun was used to generate an electron beam and a potential of 20 kV was applied for most samples. The final images were resolved using a line integral function of the operating software. The size of particles was determined after image collection using the program *Image J*.

### **3. Thermogravimetric Analysis**

Thermogravimetric Analysis (TGA) is a method of understanding changes in mass as a product of varying temperature. Inside of a TGA is a furnace and a highly sensitive balance. A given material is placed inside of the instrument and it is slowly exposed to a changing temperature. As the temperature rises, processes such as evaporation, burning, or the formation of oxides occur, and result in changes to the sample's mass. This change is measured by a highly accurate balance within the instrument. The change in mass can then be plotted as a function of temperature in order to understand the thermal stability of the material. The TGA utilized for testing was the Netzsch STA 449 F3 Jupiter. The samples were tested under flows of 40 milliliters per minute argon and 20 milliliters per minute oxygen, establishing an environment more prone to oxidizing than atmospheric conditions. The temperature was ranged from 35 to 900 degrees Celsius at a rate of 5 degrees increase per minute.

### **4. Surface Area Analysis by BET Gas Adsorption**

BET is an acronym that stands for Brunauer, Emmett, and Teller, the three researchers who first worked through the process for developing a technique of determining the surface area of a material. This process relies on the adsorption of gasses



onto the surface of a material assuming that a monolayer of adsorbates form on the surface of the material. The governing equation for this process can be written as [21],

$$\frac{1}{W \left\{ \left( \frac{P_0}{P} \right) - 1 \right\}} = \frac{1}{W_m C} + \frac{C - 1}{W_m C} \left( \frac{P}{P_0} \right)$$

Eqn. 1

where:

W=Weight of Gas Adsorbed

$W_m$ = Weight of Adsorbate Constituting a Monolayer

$P_0/P$ =Relative Pressure of Adsorbed Gas

C=The BET Constant

The BET process measures the amount of an adsorbate gas, nitrogen in this case, that forms a layer onto the surface of a material as a function of the change in relative pressure of the system. The difference in pressure can be equated to a mass of adsorbate gas. The mass of gas is combined with the assumption of a monolayer to determine the required surface area of the sample for the indicated adsorption to occur. This method of determining surface area is useful because it is nondestructive to the sample and can provide information about processes, such as sintering.

THIS PAGE INTENTIONALLY LEFT BLANK

### **III. PROCEDURES FOR MECHANICAL TESTING OF NANOPARTICLES AND NANOPARTICLE COMPOSITES IN AN EPOXY MATRIX**

While the characterization techniques outlined above provide information about the microstructure and the composition of the nanocomposites, little information is provided about the mechanical properties. For the pursuit of final application in ballistic armor, the mechanical properties of the samples were a primary consideration in the design of these new materials. The most general method of determining material properties in an engineering material is uniaxial tension and compression testing. Sparing a detailed description, a specimen with specific dimensions is mounted and exposed to either tensile or compressive forces while carefully monitoring the strain. The results can be plotted of a stress versus strain plot and properties, such as Young's Modulus, yield strength and strain to failure, can be identified. A downside to this process is that a macro-scale specimen is needed to mount into the instrument. When considering nanoscale materials, especially nanoscale composites, this approach ceases to be practical. As a result, instrumented indentation, more specifically nanoindentation, was selected to provide information about the mechanical properties of the nanocomposite.

Another key property, of this type of personal protective armor material, is its ability to dissipate shock waves. As a material is struck by a projectile, shock waves will travel through the material emanating in all directions from the point of impact. These shock waves may propagate completely through the material and be transmitted to the person or system behind the protective armor, even if the projectile is stopped. In order to make observations of the shock resisting properties of the nanocomposite, the samples were exposed to shock waves through simulated ballistic impacts in gas gun testing. While the facilities are not currently in place to measure the degradation of a shock wave through a material, the samples were analyzed postmortem in order to gather information about the fracture surfaces and the influence of the various nanoparticle and composites on the fracture (Figure 19).

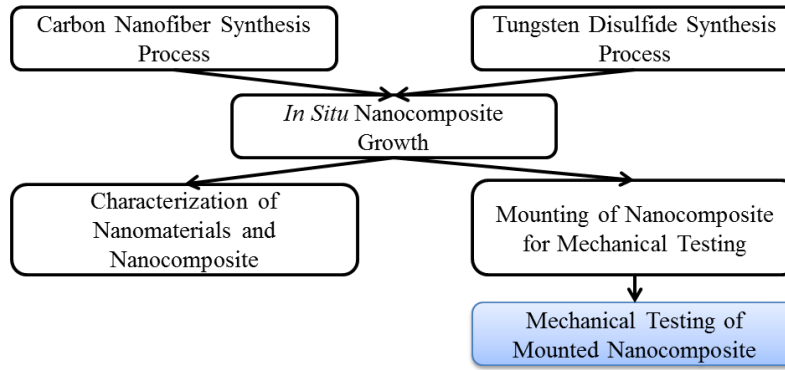


Figure 19. This section discusses mechanical testing techniques.

## A. NANO-INDENTATION

Nano-indentation has been utilized increasingly as an alternate method of determining material properties. One of the primary reasons for the shift to nanoindentation is that it can operate at high precision with extremely small amounts of material. While the nanoindenter is fundamentally a load controlled system, the displacement of the indenter tip can be measured in picometers. For the case of nanoparticles in an epoxy matrix, a larger sample size increases the likelihood of non-uniform distributions. The location of the indentation can also be carefully controlled to test regions of particular interest or ideal distribution. The majority of the information gleaned from this instrument can be represented on a load versus displacement curve (Figure 20). Of particular note is the stiffness of the material. The stiffness is represented as the initial slope of the unloading curve of the loading versus displacement plot. With the inclusion of the contact area and tip geometry, the desired properties of modulus and hardness can be determined.

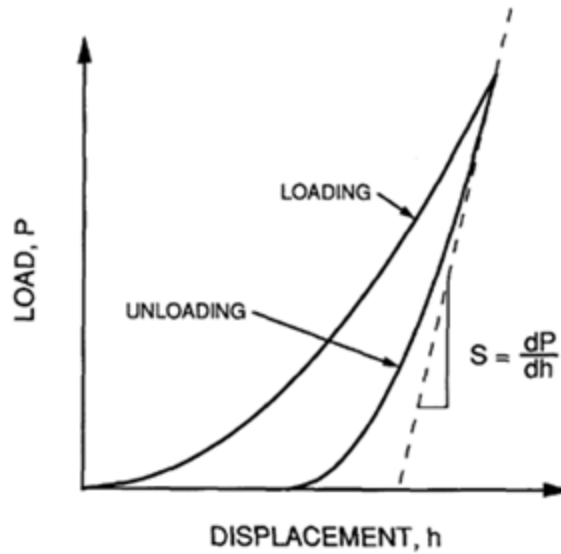


Figure 20. A generalized load versus displacement curve generated by nanoindentation. Stiffness can be seen to be the slope of the initial unloading curve. From [22].

## 1. Background of Nano-Indentation

There are three commonly used tips for nanoindentation, the Berkovich, Vickers, and the flat end cone, also known as a flat punch. The Berkovich and Vickers tips are three and four-sided pyramidal structures, respectively, while the flat punch is a cone with a removed tip (Figure 21). While the diameters of contact for the pyramidal tips are dependent on the depth of the indenter tip into the sample, the diameter of the flat punch is fixed at the size of the flat surface. For polymers, there are distinct advantages to using one tip configuration over another. Generally, the flat indenter tip is the best choice for this class of materials, and there are two major considerations that dictate the flat tip is preferable: the assurance of contact area, and the mitigation of transient effects. By using a flat tip, as long as the indenter has moved into the material, the contact area has to be the area of the indenter tip. By contrast, a Vickers tip has a different contact area depending on the distance that the indenter has moved into the material. On the other hand, there are some drawbacks to using a flat tip. Depending on the size of the indenter tip and the material selected, it is possible to achieve values of contact stiffness larger

than those of the machine. This difference in stiffness creates a problem as the measurement becomes a measure of the stiffness of the indenter frame rather than the stiffness of the material.

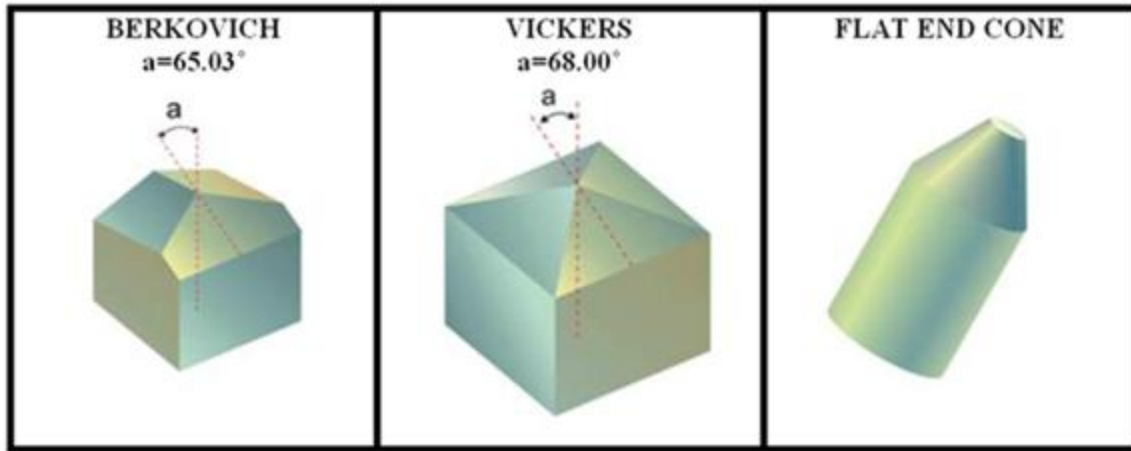


Figure 21. A summary of nanoindentation tips. Images collected from [23].

There have been many attempts to explain the phenomenon behind nanoindentation and to verify the generated results with first principle physics. Perhaps the best explanation and subsequent derivation can be found in the work by Oliver and Pharr [22]. A nanoindenter is capable of producing a highly accurate load versus displacement plot and given this data, it is possible to establish a general relationship for a flat cylinder;

$$P = \frac{4\mu a}{1 - \nu} * h$$

Eqn. 2

where: P=load  
a=radius  
h=displacement  
 $\mu$ =shear modulus  
 $\nu$ =Poisson's Ratio

By rearranging for the area of a circle and the definition of Young's modulus it can be shown that;

$$\frac{dP}{dh} = \frac{2}{\sqrt{\pi}} \sqrt{A} \frac{E}{(1 - \nu^2)}$$

Eqn. 3

where: A=area  
E=Young's Modulus for the specimen  
 $\frac{dP}{dh}$ =Stiffness

This result is important because it relates the Young's modulus to be a property of the stiffness, which can be found from the data, Poisson's ratio and the area of the tip. If the material properties of the indenter tip are known, it is possible to accurately define the reduced Young's modulus;

$$\frac{1}{E_r} = \frac{(1 - \nu^2)}{E} + \frac{(1 - \nu_i^2)}{E_i}$$

Eqn. 4

where:  $E_r$ =Reduced Young's Modulus  
 $E_i$ =Indenter Young's Modulus

The continuing analysis shows that the relationships hold true for not only flat tips, but any three dimensional revolution of a smooth function [22]. Further, it can be shown that the relationship holds true for the Berkovich and Vickers tips as well with the addition of a known geometric factor;

$$\frac{dP}{dh} = \beta * \frac{2}{\sqrt{\pi}} \sqrt{A} * E_r$$

Eqn. 5

where:  $\beta$ =geometric factor dependent on tip geometry

While this analysis does an excellent job of applying first principles to model complex behavior, it does make one critical assumption. When modeling materials such as a metal, it can be assumed that it will operate in a linear elastic regime. When modeling polymers however, this is not the case and in fact, one of the most useful ways to test polymers is with a dynamic viscoelastic method. As a result the most accurate way to describe the modulus of a polymer is not with a single value as is the case with metals, but rather as a complex modulus. The complex modulus is comprised of two distinct moduli, the storage modulus and the loss modulus. The storage modulus is a real term

that equates to the elastic energy storage while the loss modulus is an imaginary component that correlates to the energy that is dampened by the material through viscous deformation [24]. These relations are additive and following the derivation from [25];

$$E_c = E' + iE''$$

Eqn. 6

where:  $E_c$ =Complex Modulus  
 $E'$ =Storage Modulus  
 $E''$ =Loss Modulus

It is possible to solve for both the loss and storage moduli with the addition of a few terms. With the added detail, it is now necessary to include information about force amplitude, displacement amplitude, the phase angle of the system damping, and frequency of the indentation as the response is now time dependent. By adding these factors and some parameters of the indenter, it can be shown that the moduli equations become [25];

$$E' = \frac{S}{2\beta} \sqrt{\frac{\pi}{A}}$$

and,

$$E'' = \frac{\omega D_s}{2\beta} \sqrt{\frac{\pi}{A}}$$

Eqn. 7 & 8

assuming that,

$$\omega D_s = \left| \frac{F_0}{z_0} \right| \sin(\phi) - \omega D_i$$

and,

$$S = \left| \frac{F_0}{z_0} \right| \cos(\phi) + m\omega^2 - K_s$$

Eqn. 9 & 10

where:  $\omega$ =Harmonic Frequency  
 $F_0$ =Force Amplitude  
 $Z_0$ =Displacement Amplitude  
 $\phi$ =damping phase angle  
 $D_s$ =Damping of the System  
 $D_i$ =Damping of the Indenter  
 $K_s$ =Support Stiffness  
 $m$ =Mass of the Indenter



## **2. Operating Conditions and Summary of Experimental Data Acquisition**

Using these equations, it is possible to accurately analyze the load and displacement output of the nanoindenter and determine the frequency-dependent moduli of the material. If it can be determined that the material in question has a loss modulus that is insignificant, it is also a valid assumption to drop the term from the equation. In this case the complex modulus becomes the same as the storage modulus. Two programs provided by Agilent were utilized for the nanoindentation.

The first program was named *XP-CSM Flat Punch Complex Modulus JLHMod*. This program assumes that the modulus is comprised of both a loss and storage component. As a result, the operative equations are akin to those in the latter half of the derivation. This program required the use of a flat punch tip and the tip selected for use had a diameter of 50 microns. Within the program, the Poisson's ratio was set to a value of 4.00, a common value for epoxies, and a 2.0 micron pre-compression depth was selected. In order to develop the complex modulus, the sample can be tested at a series of different frequencies. Depending on the material, it is possible to have a frequency dependent complex modulus, and to test for this phenomenon, the frequency of the indenter tip was ranged from 1–45 Hz, in a series of 5 steps. The remaining program settings were left in their default state. A series of 20 points, with a spacing of 100 microns in both the horizontal and vertical directions, was selected for indentation. The spacing was increased to a larger value than the normal 50 microns in this instance, due to the desire to avoid any interference in between indentations as a result of the increased width of the indenter tip. Once the program had completed its run, images of the indented surface were collected in the event that surface conditions caused variances in the data.

The second program utilized was titled *XP-Basic Modulus/Hardness at Depth* and was designed to extract the modulus and hardness of a given sample. This program works upon the assumption that there is no loss modulus, and that the operative principles are essentially those found in the first half of the derivation. In order to correctly implement the program, a Berkovich indenter tip was utilized. The majority of the operating conditions were maintained in the default settings, with the exception that the Poisson's

ratio was again set at a value of 4.00 and the depth was set to a depth of 2000 nm. An array of points on the surface of the sample was then selected for indentation. A grid of 20 points was established with a standard spacing of 50 microns in both the horizontal and vertical directions. Once the program had finished, an image of the indented surface was then taken in order to document the locations in the event of variances in the data that were a result of the surface conditions.

## **B. HIGH SHOCK (GAS GUN) TESTING**

### **1. Background of Gas Gun Testing**

Personal protective armor materials must be able to dissipate shock waves to prevent blunt force trauma in order to be fully effective. When a solid material is struck by a projectile, shock waves will travel through the material emanating in all directions from the point of impact. In order to understand how to account for these shock waves and to develop materials to limit their effects, it is important to understand how shock waves propagate.

One of the best ways to develop information about the effect of shock waves on various materials, is to conduct testing in a gas gun. Simply explained, a gas gun is comprised of a long cylindrical barrel with a high pressure tank, or breech, on one end and a sample holder on the other (Figure 22). The breech is pressurized with an inert gas and when the appropriate conditions are met, the gas is released, propelling a slug down the barrel into the sample holder. When the slug impacts the surface of the holder, shock waves propagate through the sample and the effects of the shock can be determined. The gas gun model is well suited to research as it is repeatable, and if designed correctly, can model the shock in one dimension reducing the amount of required computations to extract results. In order to be modeled as a one dimensional problem, the sample holder must be of sufficient diameter that the shock will propagate through the sample prior to internal reflections. Also, the surfaces of the sample and the slug must impact at one instant across the surface.



Figure 22. A picture of the gas gun setup. The breech is smaller cylinder on the right and the sample holder is the larger vessel on the left side of the barrel. From [26].

Shock propagation in solids is different from those in liquids or gasses and cannot be modeled in a similar way to shock effects for supersonic flow. The main difference is that the particles in solid shock have a velocity component, while shock in a fluid does not. Another difference is the impact of rarefaction waves which reduce the pressure of the shock. When considering the solid shock process, it is helpful to first think of the slug moving down the barrel at a given speed. The speed that the slug is traveling is the particle speed, and the shock speed, the speed of the shock in the material, is zero. The instant that the slug becomes incident on the surface of the sample, this state is altered. Once the surfaces touch, a shock wave is generated moving away from both surfaces in question creating a condition where particle speed and shock speed are non-zero (Figure 23).

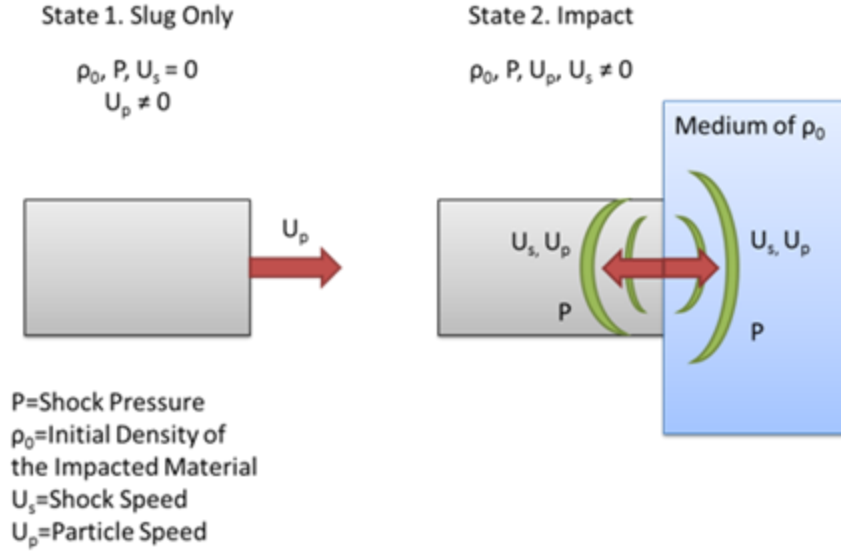


Figure 23. The left case is the slug moving prior to impact while the right case is the state at impact. The speeds are represented symbolically as arrows and the shock is represented by a series of arcs.

Using this reference frame, a series of equations can be developed for the physics of the interaction. The most important property for this analysis, is the momentum of the system which can be represented as [27];

$$P = \rho_0 * U_s * U_p$$

Eqn. 11

Another aspect of the interaction is the existence of a wave moving back into the slug, referred to as a rarefaction wave, while the shock wave moves into the sample. In order to avoid violating a fundamental law of thermodynamics, the momentum of the system must be conserved and as a result of the rarefaction, the shock must be comprised on only a portion of the energy in the slug. In order to develop the remaining information to account for this divergence of energy, the Hugoniot equations of state are utilized. This is an empirically determined expression which relates the shock speed to the particle speed in the form [27];

$$U_s = A + b * U_p$$

Eqn. 12

where:        A=Empirically Determined Constant  
               b= Empirically Determined Constant

Values for the empirically determined constants can be obtained from data tabulated for a number of different materials. In order to find these constants, a certain type of material was subjected to a battery of gas gun impacts under different conditions. The results from these tests were plotted and, assuming a linear fit, values were extracted. If this result is combined with the momentum equation, it is possible to develop a relationship in between the shock pressure and the particle speed [27];

$$P = \rho_0 * (AU_p + bU_p^2)$$

Eqn. 13

With this relationship, it is possible to plot both the shock and rarefaction waves. The shock wave will start at a particle speed of zero and as the speed increases, the shock pressure will rise. The rarefaction wave will have a maximum pressure when the particle speed is zero and will decrease until pressure is zero when the particle speed equivalent to that of the incident slug. The crossing point of the two curves, known as Hugoniot curves, indicates the pressure and particle speeds at the impact. This point is referred to as the impedance match state. In the case that the slug and the sample are made of the same material, the curves will be mirror images around the impedance match state which will occur at one half the speed of the incident slug.

## **2. Operating Conditions**

In each of the cases, the epoxy slice was loaded into an aluminum sample holder and secured inside of a chamber at the end of the barrel. Behind the sample holder was a series of aluminum honeycomb and rubber sheeting to help absorb and dissipate the energy from the slug. An aluminum slug with a nominal mass of 480 grams was used in each case. The slugs were cylindrical with a flat impact face and a cavity bored out of the rear. This cavity was created in order to allow the expanding gasses to better push the slug through the barrel. The breech was pressurized to 1300 psi, which corresponds to a slug velocity of 370 meters per second. Both the slug and the sample holder were made

of the same type of aluminum and as a result the impedance match state occurred at a particle velocity of 185 meters per second and a shock pressure of 2.796 GPa (Figure 24).

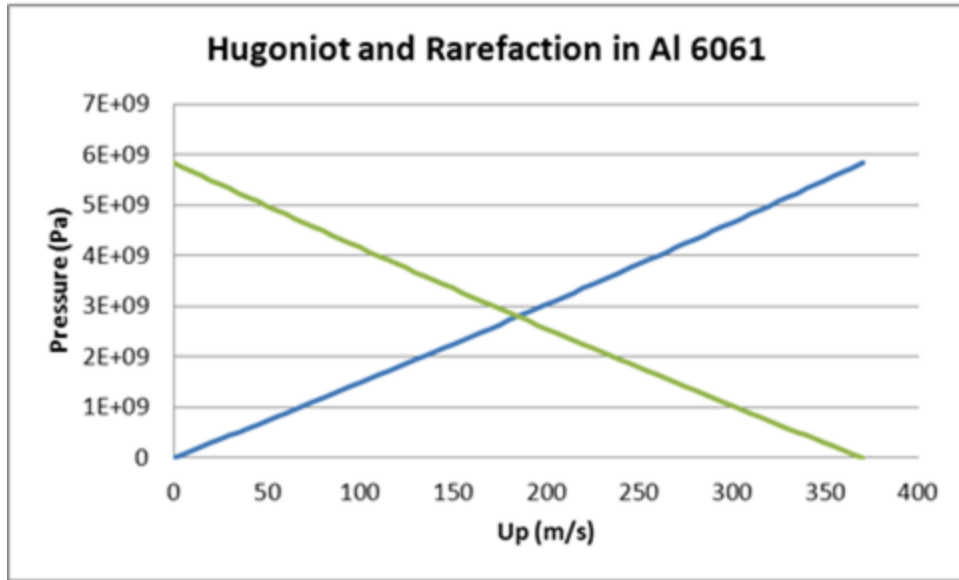


Figure 24. The Hugoniot plot for an aluminum-aluminum interaction. The shock is represented as the line with a positive slope, while the rarefaction is mirrored around the impedance match state.

For the case reviewed in this analysis, there was an additional complication. While the slug and the sample holder were comprised out of the same type of aluminum, the sample was an epoxy composite. In order to account for this difference, an additional plot was required. A similar plot to the previous case was generated with the new values for particle speed. A third line for the epoxy was also plotted onto the Hugoniot plot. In this case, the composite was assumed to have the same properties of a pure epoxy to determine the values of the empirically determined constants. This assumption was made in order to complete the estimate of the shock values. There is no method available to accurately determine the shock impedance values for the samples tested without experimental determination. To determine the value accurately, a complete characterization of the material across a range of slug speeds would be required which was outside of the scope of this research. Starting at the zero particle speed, the Hugoniot for the epoxy was plotted and intersected the rarefaction curve. This intersection represents the shock pressure and particle speed in the epoxy composite

(Figure 25). In this case, the shock pressure present in the sample is approximately 0.695 GPa and corresponded to a particle speed of 137.5 meters per second.

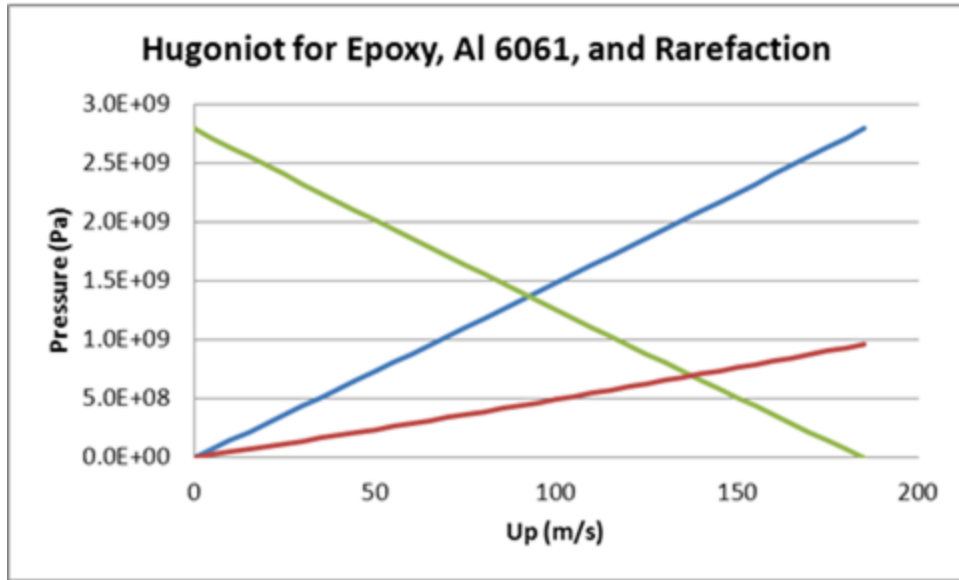


Figure 25. The Hugoniot plot for an aluminum-aluminum and epoxy interaction. The shock is the line with a positive slope, while the rarefaction is mirrored around the impedance match state. The additional line represents the epoxy and the intersection with the rarefaction curve gives the shock pressure.

THIS PAGE INTENTIONALLY LEFT BLANK



## IV. RESULTS ANALYSIS AND DISCUSSION

### A. EXAMINATION AND DISCUSSION OF NANOPARTICLES AND NANOPARTICLE COMPOSITES

#### 1. Growth and Characterization of Carbon Nanofibers

This section will discuss the growth and characterization of carbon nanofibers grown under different conditions as well as the analysis of the nickel catalyst (Figure 26).

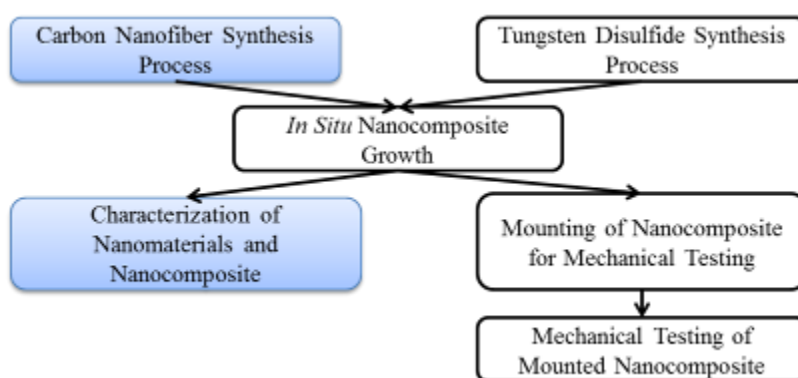


Figure 26. This section characterizes the carbon nanofibers synthesis.

##### *a. Comments about Nickel Nanoparticle Catalyst*

In order to initiate the growth of carbon nanofibers, a catalyst is required. Common metals that serve as a catalyst in this capacity are iron, palladium, and nickel among others. For this research a nickel nanopowder was selected as the catalyst. Nickel nanopowder was selected to be the catalyst over iron or palladium for a number of reasons. When compared to palladium, it was a more readily available material with similar properties. Nickel also produces more graphitic fibers at lower temperatures when compared to palladium. Iron produces either fibers or tubes, but in its nanoparticle form is extremely reactive and can self-ignite in air. In order to operate at low temperatures and to allow for handling of the precursors, nickel nanoparticles were selected.

The commercial nickel nanopowder used as a catalyst was specified for a particle size of 100 nm or less. To confirm the particle size, the sample was analyzed using SEM. In the sample, the vast majority of the nickel particles had diameters on the scale of 100 nm (Figure 27). These particle sizes were readily visible at high magnification, but at lower magnifications, they stacked and clustered producing structures that could be mistaken as large agglomerations. There were also a number of particles observed that were much larger. The most pronounced example was micron size nickel particles. These nickel particles formed into spheres and were scattered throughout the sample. Higher magnification also yielded the presence of nickel fragments smaller than 100 nm. The size of the carbon fiber produced will be a direct reflection of the size of the particle that was used to catalyze the reaction. As a result, the larger micron sized spheres will likely create micron diameter fibers while the 100 nm will create fibers of a similar size. The smaller nickel particles could also result in a fiber size less than 100 nm. The nickel nanopowder was utilized in this form despite the inclusion of larger particles to act on the possibility that a multi-modal distribution would provide a beneficial impact to the mechanical properties of the material.

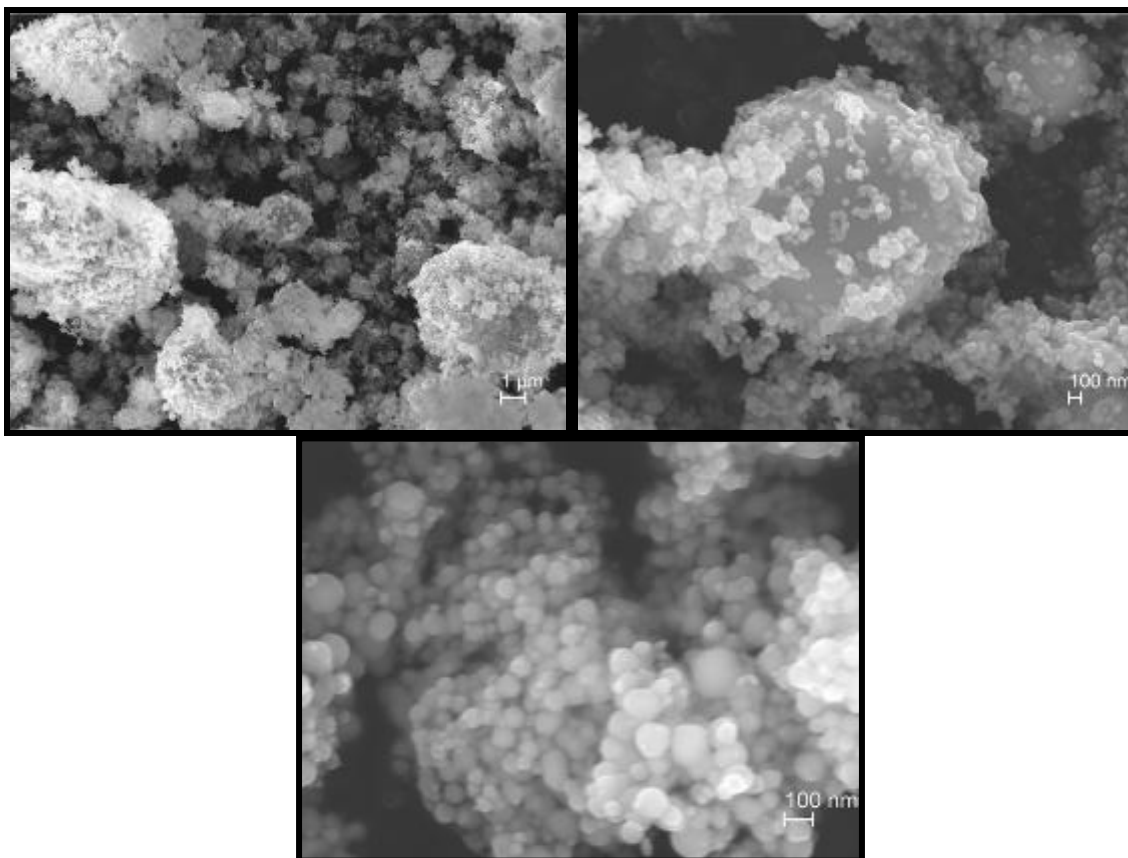


Figure 27. SEM image of commercial nickel nanoparticles. These particles formed large agglomerations as seen in the top left image. Some particles were micron scale, such as the sphere shown in the top right image, but the majority were on the scale of 100 nm as seen in the bottom image.

An important consideration of using the nickel nanoparticles as a catalyst is the possibility of sintering. Sintering is a process by which small particles merge together to form larger particles as a result of the application of temperature. This is especially prevalent in nanomaterials, as the ratio of surface area to mass is larger than in its bulk form, resulting in higher reactivity. In order to achieve a lower surface energy, the particles will sinter together to form larger particles even if exposed to temperatures far below the bulk melting temperature. This factor can result in a nanomaterial melting point several hundreds of degrees lower than what would be expected from the bulk [28].

The effect of sintering can be noted by studying the change in surface area of nickel nanoparticles with BET. To illustrate the effects of sintering on nickel

nanoparticles, three different heat treatments were compared to a control sample that had been maintained at room temperature. The samples were heated inside of the tubular furnace to 300, 500, and 700 degrees Celsius for a period of one hour. After that time the samples were removed and the surface area was calculated. For the baseline case, the surface area was determined to be 11.975 square meters per gram. For the 300 degrees case, the surface area decreased to 6.199 square meters per gram followed by a further reduction at 500 degrees to 3.441 meters per gram. The final 700 degrees test resulted in a surface area of zero. Based on these results, the nickel nanoparticle catalyst should be expected to sinter to some extent at the synthesis operating temperatures without the inclusion of procedures to mitigate the effect. As it will be discussed in the next section, slight modifications to the carbon growth step were made to prevent the formation of nickel agglomerates due to sintering, such as a 350 degree growth step before moving to the optimal 550 degree growth step.

***b. Carbon Nanofibers Synthesized in the Presence of Oxygen***

Each of the different steps in the growth process achieved a particular aim to promote the synthesis of carbon nanofibers. The purpose of the argon-hydrogen mixture was to provide a reducing environment. By creating this environment, any oxide layer that might have formed on the nickel nanoparticles was removed, preparing the sample for carbon deposition. The ethylene gas provided the carbon for the system in the form of a hydrocarbon fuel source. As the ethylene passed over the nickel nanoparticles, a decomposition reaction was catalyzed at the surface of the nickel. As the decomposition occurred, it deposited carbon onto the surface of the nickel. This deposited carbon forms into graphitic structures, and by collecting additional carbon from the ethylene gas, will grow into carbon fibers. Very small amounts of oxygen aid this process by providing the environment necessary for the continuation of the decomposition reaction (formation of radical species). It should be noted that larger amounts of oxygen will promote the solid carbon in the fibers to be burned off. AS a result, the flow ratios in between ethylene and oxygen were always maintained in fuel rich conditions.

There were also specific reasons for the temperatures at each stage of the process. At 550 degrees Celsius, carbon fiber growth is promoted on the surface of a metal catalyst [15]. The primary growth step occurs at this temperature in order to achieve the largest growth of fibers. The reason the temperature is first increased to 350 degrees Celsius is to form a layer of carbon around the nickel catalyst. When carbon begins to deposit onto the surface of the nickel nanoparticles, it prevents the nickel from sintering. If the particles do not sinter together, the overall fiber size will remain low. If the synthesis was allowed to heat to 550 degrees Celsius initially, the fiber size would increase significantly to microns or tens of microns in diameter instead of the preferred nanofibers. The occurrence of this event was confirmed with FIB milling and will be discussed in greater detail in the next section.

When the synthesis was allowed to run for a period of 90 minutes at a temperature of 550 degrees Celsius, the total yield of carbon nanofibers was approximately 2.11 grams, from 0.051 grams of nickel nanoparticle catalyst. Inside the constraints of the combustion boat, the fibers were well intertwined with one another and the bulk material was akin to that of tough foam. On the unconstrained growth on the upper portion of the combustion boat, the growth was more akin to a powder. SEM images suggest that the fibers grow primarily in three size groups. There are a few small large 1–5 micron diameter fibers and many distributed pockets of very small fibers 10–15 nm in diameter. The main and most widely spread constituent fiber diameter was on the order of 200 nm. This bi-modal distribution is similar to the multi-scale architecture found in [15] and is expected from the distribution of catalyst diameters. The most notable difference is that while previous experimentation took place on the surface of micron scale fibers sputtered with a metallic catalyst, these experiments were based from a metal catalyst alone [15]. The length of the fibers was difficult to determine, as the fibers twist and tangle together with few exposed ends. Although the exact length is not known, the fibers with a diameter on the order of 200 nm have an observed length of at least 7 microns (Figure 28).

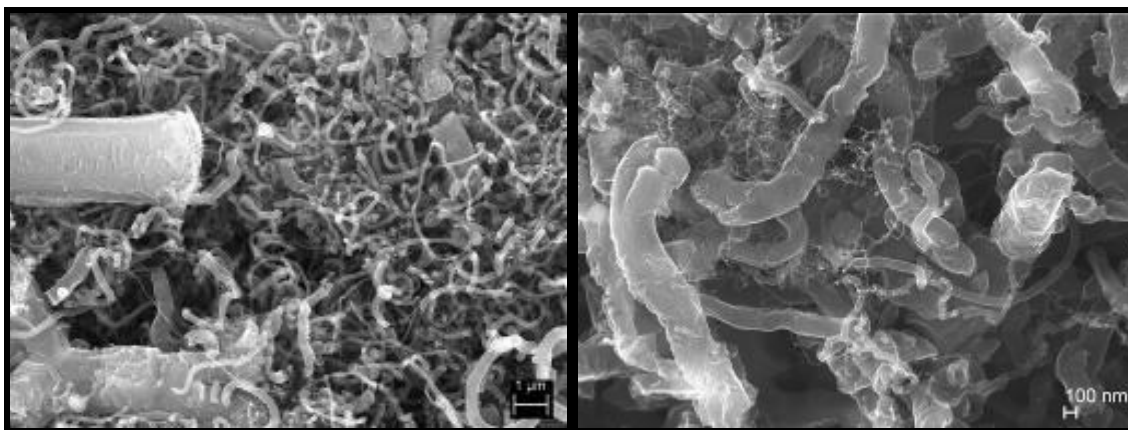


Figure 28. Carbon nanofibers grown from a nickel nanoparticle catalyst. The left image shows the inclusion of larger micron size fibers while the right image shows the smaller fibers on the order of 10 nm.

The distribution in the fiber size on the carbon nanofibers can be directly attributed to the size of the nickel nanoparticles used as a catalyst. The analysis of the nickel nanoparticles returned three notable particle sizes, and the powder was utilized without post treatment in the aim of developing multi-modal fibers. The largest particles were micron sized and correlate to the large nickel spheres. The clusters of small fibers also correlate to the presence of small nickel fragments. The predominate fiber size on the order to 200 nm is slightly larger than the main 100 nm constituent of the nickel particles, but still illustrates a clear relationship to catalyst size and fiber diameter.

### *c. 350-Degree Carbon Growth Step*

The additional growth step at a temperature of 350 degrees Celsius was characterized in this research and its effects have not been classified in the literature. The effectiveness of the 350 degree step can be illustrated with images from the SEM. These particles appear different than the pure nickel catalyst which can be attributed mainly to the sintering process (Figure 29). The surface of the sample did not show the small particles characteristic of the unprocessed nickel particles and instead the smaller particles began to sinter together. At this point the sintering of the particles is not complete, but shows clear signs of the process of necking. Necking is a stage in sintering where particles form a solid bridge but have not pulled together to reform into a single

spherical particle. While these images do show that some sintering has occurred, they do not differentiate from sintering that happened during the reducing step at 350 degrees or the carbon fiber growth step. In order to determine the timeline, additional methods of characterization were needed.

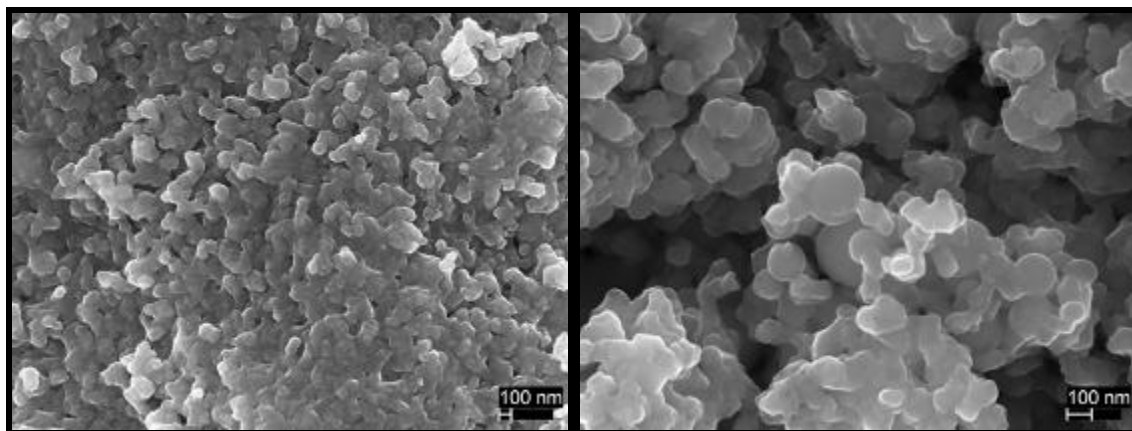


Figure 29. SEM images depicting the impact of sintering on the nickel catalyst when heated to a temperature of 350 degrees Celsius.

In order to determine if the sintering or deposition of carbon on the surface were different from the covered particles in an agglomeration FIB was utilized. In order to focus the FIB, the stage inside of the SEM was tilted to 54 degrees. This allowed the surface of the sample to be perpendicular to the ion beam. The images from the FIB and the in lens detector were collocated onto a single point to allow for analysis. The ion beam was focused onto an agglomeration of nickel particles and a section was milled away to expose the internal particles. The potential for the FIB was fixed at 30 kV and the initial milling step cut away a trapezium using a current of 2 nanoamps. This was the highest amperage used and was intended to provide a rough milling that could be refined in later steps. These operating conditions were able to cleanly cut through the nickel and the outline of the resulting trapezium was clearly formed (Figure 30). The deposits of material that appear as mounds inside of the trapezium represent the material that was displaced by later passes of the FIB. The final pass was at the upper surface, and because no subsequent passes were made it is devoid of these depositions. In order to refine the surface, the amperage was reduced in two steps. The first encompassed the

entire upper surface and operated at 100 picoamps. The second used 20 picoamps of current and only milled the right half of the upper surface.

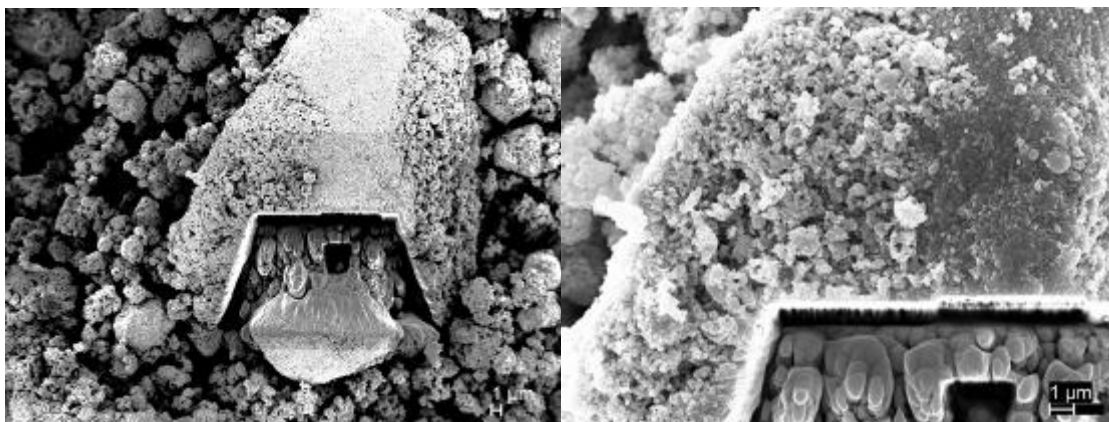


Figure 30. SEM images of nickel nanoparticles after FIB milling. The full trapezium can be seen in the left image and the refinements to upper surface can be seen in the right image.

Once the FIB milling was complete, the image was shifted to the in lens camera. This provided a view of the surface at an angle equivalent to the tilt of the stage. This image was stretched out of normal proportions as a result of the tilt and the image was compensated using the operating software. Once the SEM was appropriately oriented and focused, several characteristics were notable (Figure 31). The first was not a product of the material, but rather of the FIB milling. Vertical lines known as drapes are visible on the cut surface and are a product of the ion beam. As the gallium ions mill the surface of the material they leave a mark on the surface. If the rastering of the ions in the FIB is not aligned perfectly, some of these marks will remain. The next feature was the distribution of the particles and shape of the particles. Low magnification confirms that the agglomeration was actually comprised of a number of nickel nanoparticles with included porosity. As with the surface, there is clear evidence of sintering, and necking can be seen throughout the cross-section. The higher magnification image also shows that the surfaces of the particles inside of the pores have small features in contrast to the smooth geometry of the surface of the sample. This could indicate the presence of small fragments sintering onto the surface of larger particles or the deposition of carbon.



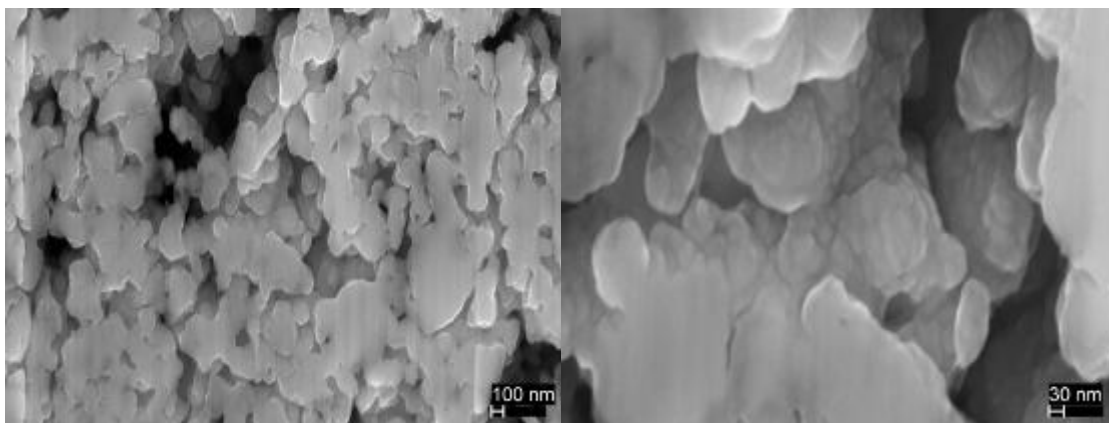


Figure 31. Images of the FIB milled surface taken with the SEM. These images show the porosity of the agglomeration as well as the structure of the included particles. The vertical lines are a result of the FIB milling.

In order to determine if carbon had actually formed on the surface of the nickel, during the growth step at 350 degrees, EDX was utilized. The goal of the EDX analysis was to identify the presence of carbon on the sample. If carbon was present it would most likely be in the form of a nanolayer surrounding the nickel particles and would be difficult to identify visually. The first attempt to determine the elemental content of the sample was conducted over an area, and later tests were conducted at specific points (Figure 32, 33). The area analysis showed the strongest return from nickel with smaller peaks from both oxygen and carbon. The strong nickel peak is expected as the vast majority of the sample is comprised of nickel. It should be noted that EDX cannot be used to identify the percentages of elements present without careful calibration of the instrument, which was not conducted for this research. Consequently, both oxygen and carbon can be confirmed to be in the sample, but the relative percentages of each in the bulk material cannot be determined with certainty. In the spot analysis, it was possible to identify regions of the material with large deposits of carbon. These larger deposits showed comparable returns for both carbon and nickel with a negligible amount of oxygen. The EDX confirmation of carbon deposits in the system supports the hypothesis that the nickel particles are being coated with a layer of carbon arresting further sintering. However, the carbon appears to have larger deposits in certain regions instead of even dispersal over the bulk. The oxygen in the sample also suggests the possibility of nickel

oxide forming in small quantities on the surface. Oxygen does not appear in any other analysis of fully synthesized samples, so it is likely that once the temperature is increased to 550 degrees Celsius it is consumed in the decomposition of the ethylene. In order to make a full determination of the reactions during this 350 degree step further analysis will be required.

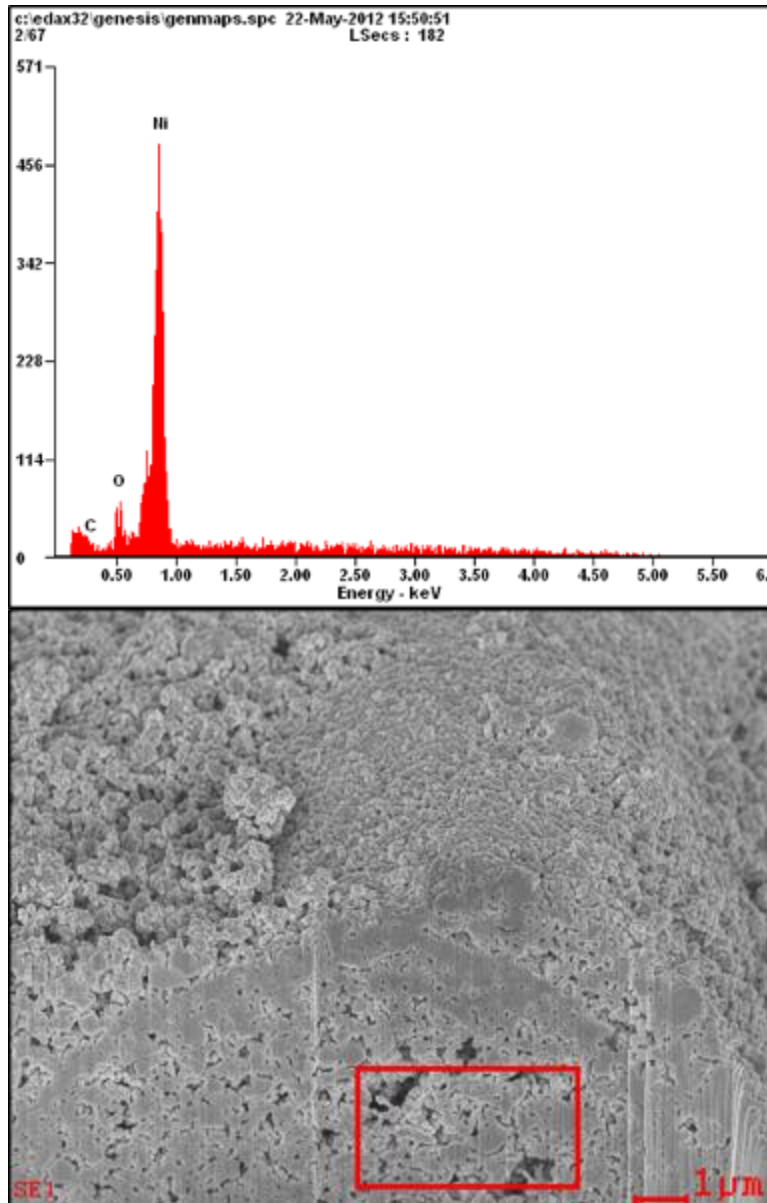


Figure 32. EDX of a region of the FIB milled surface. Nickel is the dominant element in this spectrum, but traces of oxygen and carbon are also shown. The lower SEM image indicates the region where the analysis was conducted.

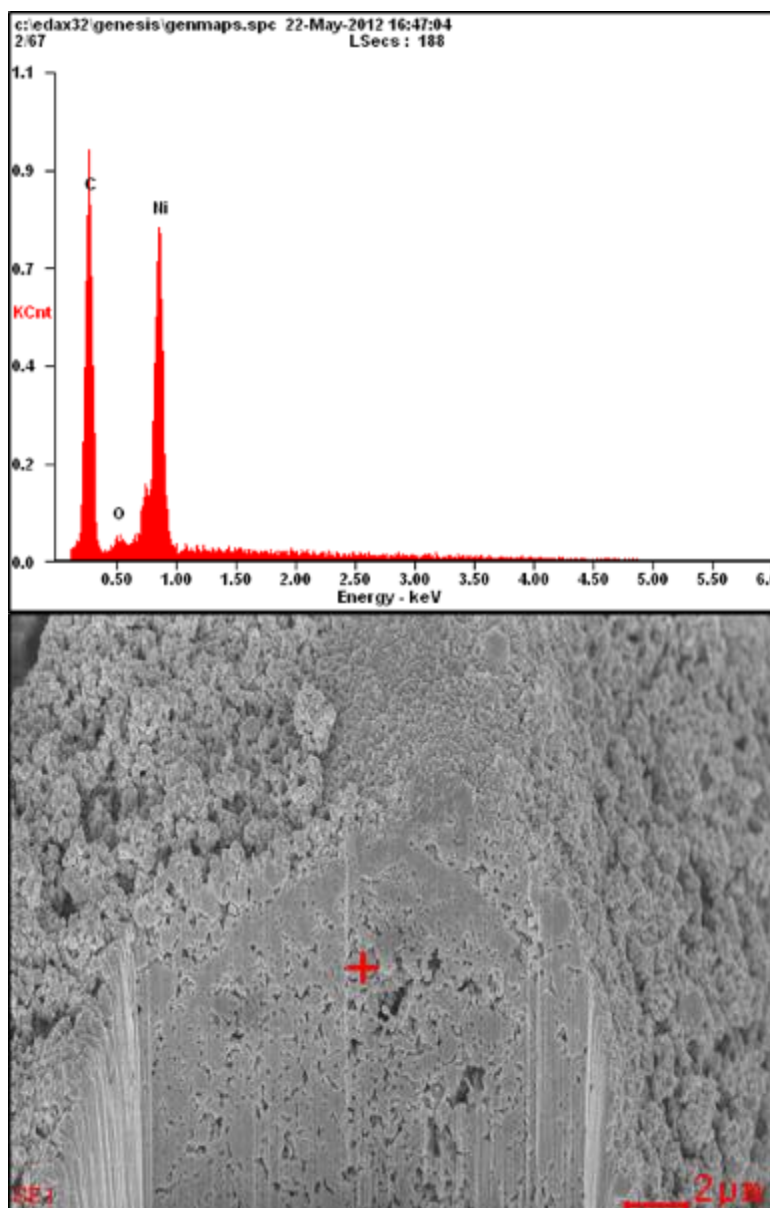


Figure 33. EDX of a region of the FIB milled surface. This spectrum shows a much higher incidence of carbon as well as nickel and traces of oxygen. The lower SEM image indicates the point where the analysis was conducted.

#### *d. Carbon Nanofibers Synthesized in the Absence of Oxygen*

In the previous method, the actual carbon fiber growth step occurred in the presence of oxygen gas. In later processes where tungsten disulfide might be present in a nanocomposite with the nickel nanopowder catalyst, it would be essential to avoid the use

of oxygen as it might oxidize the tungsten sulfide. One critical modification was made to the growth process found in the literature [16]. Instead of using palladium as a catalyst, the same nickel nanoparticles as the previous run were used. The synthesis conditions were otherwise unchanged. A trial synthesis was conducted in order to determine the efficacy of the alternate grow procedure.

In this method, carbon nanofibers were produced, but the yield was significant smaller than the previous method. For 0.051 grams of nickel nanoparticle catalyst utilized, only 0.083 grams of carbon fibers were produced. Given that this method produced less than four percent of the fibers from the method with oxygen, it was not pursued as a synthesis procedure. Even though the yields were very small by comparison, there still is a viable reason for continuing to pursue a carbon nanofiber synthesis process without the inclusion of oxygen gas. If an argon-hydrogen mixture is substituted for the oxygen gas, the possibility of converting tungsten disulfide into tungsten dioxide is eliminated. The removal of this possibility would increase the viability of including tungsten disulfide particles with carefully controlled structure into the nickel nanoparticle catalyst prior to the synthesis of carbon fibers. The process was optimized for the use of palladium, not nickel, and it is possible that if modifications were made to the temperature ranges and atmosphere, as a result of the change in catalyst, it would be possible to achieve better yields.

## **2. Characterization of Tungsten Disulfide**

This section will discuss the growth and characterization of tungsten disulfide grown under different conditions as well as the analysis of the commercial product (Figure 34).

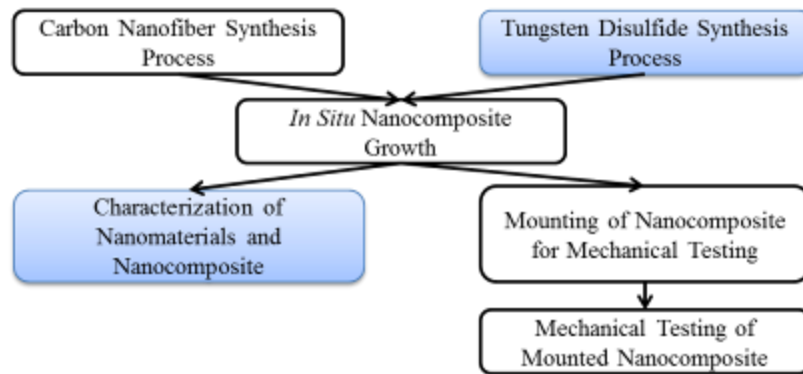


Figure 34. This section characterizes the tungsten disulfide synthesis.

*a. Commercial Tungsten Disulfide*

Tungsten disulfide can form into a number of different structures. For the purposes of this research, nanoscale tungsten disulfide inorganic fullerenes were desired. In order to acquire these structures, the commercial product was analyzed first. The tungsten disulfide purchased from Sigma Aldrich was analyzed with SEM and XRD. While the XRD pattern confirmed that the material was tungsten disulfide, the SEM showed that the material was not a viable precursor for the research. The first concern with the commercial material was the size of the particles. The product was comprised of particles averaging less than two microns in size. While the average size was consistent with the manufacturer specifications, SEM analysis showed the presence of many large particles on the order of 10 microns (Figure 35). Given the desire to form true nanoscale architectures, these particles were too large and would require further treatment to reduce particle size. Another concern was the structure of the particles. The particles found in the commercial sample were formed into platelets, not the desired inorganic fullerenes. While this shape does make sense for many of the other commercial applications of tungsten disulfide, such as a solid lubricant, it does not fit the needs of the project and as a result, other methods for acquiring the material were sought.

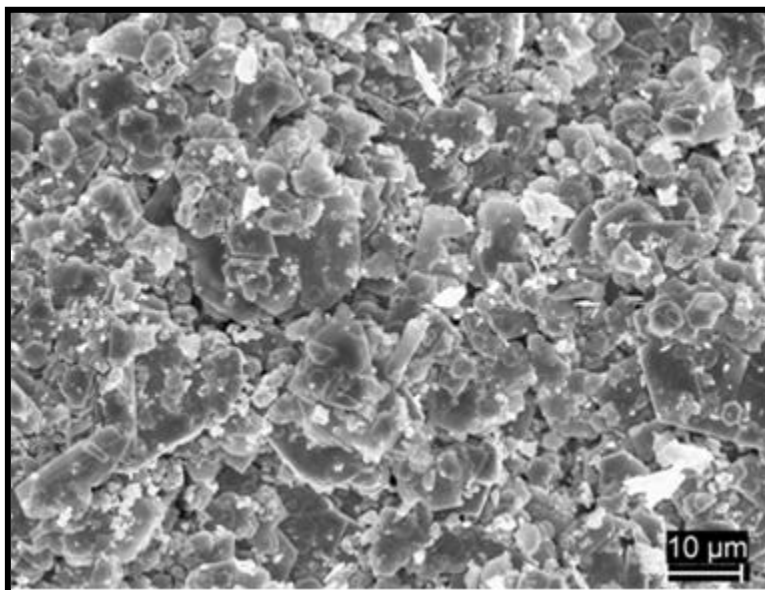


Figure 35. SEM image of commercially purchased tungsten disulfide. The particles have a microstructure resembling large platelets.

#### ***b. Synthesis of Tungsten Disulfide***

Two methods of synthesizing tungsten disulfide were explored. The first utilized an ammonium tetrathiotungstate precursor while the second utilized a tungsten oxide precursor. Each of the two methods had advantages and disadvantages. Procedurally, the decomposition of the ammonium tetrathiotungstate precursor was a simpler process, requiring only a reducing atmosphere and an elevated temperature, while the sulfurization required hydrogen sulfide gas. However, the XRD pattern from the two sources showed a more crystalline composition for the particles derived from tungsten oxide (Figure 36). Further, the synthesis of the carbon fibers posed potential problems for the tungsten sulfide. In the case of the decomposition of the ammonium tetrathiotungstate precursor, the tungsten disulfide would be present for all of the subsequent growth steps. The processes that actually provide for the deposition of carbon and the growth of fibers utilize oxygen gas. The inclusion of oxygen allows for the possibility of oxidizing included tungsten sulfide particles. Tungsten oxide is thermodynamically favorable to tungsten disulfide, and as a result, if given the appropriate activation energy it will react. As a result, the use of tungsten oxide and sulfurization after all growth steps have been

completed would likely result in a greater yield of tungsten sulfide. This process is also identified in the literature as being a better method to produce inorganic fullerenes from tungsten oxide [19].

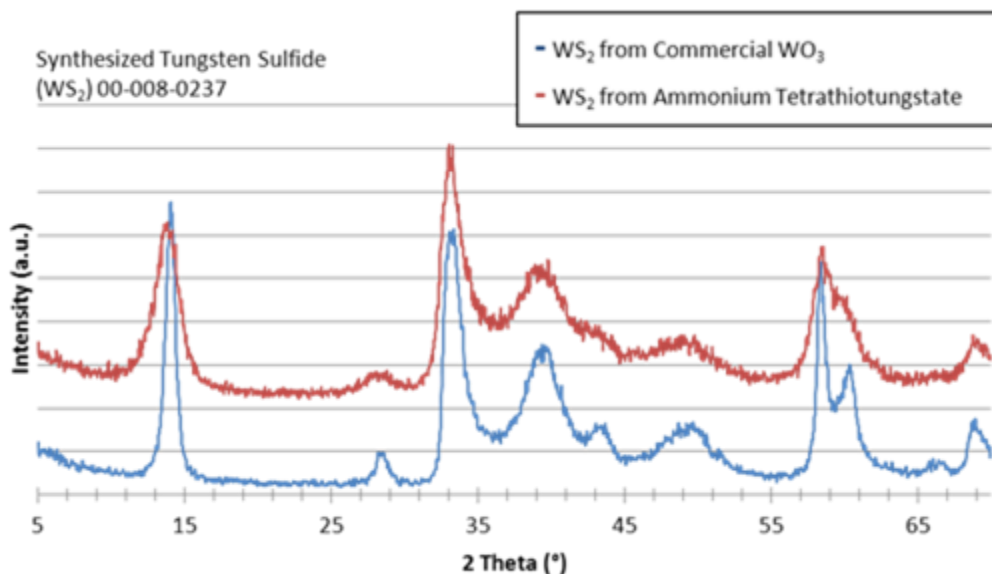


Figure 36. Offset XRD patterns from two different syntheses of tungsten disulfide. The lower came from tungsten oxide while the upper came from ammonium tetrathiotungstate.

### 3. Synthesis of Nanoparticle Composites

In order to achieve the desired properties for the shock absorbing personal protective system, it was necessary to find a method to combine the carbon nanofibers and the tungsten disulfide spheres. By creating a composite, the inherent properties of each of the materials could be conserved. There were several methods that were pursued in order to create a composite with the two materials. The first possibility was to mechanically mix the tungsten disulfide particles into a sample of carbon nanofibers. The other possibilities involved mixing the tungsten disulfide, or a tungsten precursor, into the nickel catalyst and then growing the carbon nanofibers afterwards.

If the tungsten disulfide was mechanically mixed into carbon nanofibers it would provide the largest degree of control over each of the constituents to the composite. The carbon nanofibers could be grown to be an optimal length without interference to the nickel catalyst from other materials. Likewise, the structure of the tungsten disulfide could be controlled externally to the construction of the composite. In this case however, the tungsten disulfide would not be homogeneously distributed at the nanometer scale into the carbon nanofibers. By growing the fibers *in situ* with the tungsten particles the composite would be more uniform in composition. Further, the carbon nanofibers would likely grow and intertwine around the tungsten particles, holding them into a type of matrix. The potential downside to the *in situ* growth is the possibility of the tungsten disulfide, or the tungsten disulfide precursors, interfering with the growth of the carbon nanofibers, or vice versa. For the purposes of this research, the mechanical mixing method was not pursued, opting instead for the *in situ* growth to maximize the entanglement and uniform distribution of the tungsten disulfide particles (Figure 37).

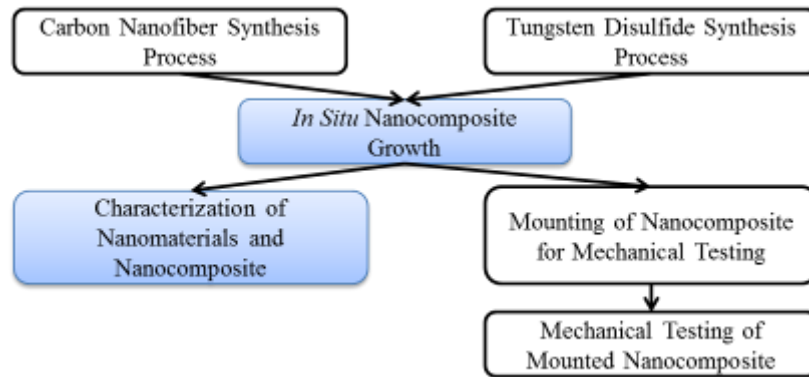


Figure 37. This section will discuss the characterization of nanoparticle composites.

**a. Carbon Nanofibers *in situ* with Tungsten Disulfide**

The two different types of tungsten disulfide were mixed with the nickel nanopowder catalyst in order to perform an *in situ* synthesis of carbon nanofibers. For these experiments, the commercial tungsten disulfide and the tungsten disulfide from the decomposition of ammonium tetrathiotungstate were utilized. Although the components were derived from different sources, the outcome of the synthesis was the same; carbon



nanofibers were not produced. In order to rule out the possibility of contamination or other procedural error, the syntheses were repeated with the same end result. To better understand what had occurred, XRD data was taken from the sample. (Figure 38) The analysis showed no evidence of graphitic peaks or other forms of crystalline carbon in the sample. The same reveal that very small quantities of two new species, tungsten oxide and nickel sulfide, were now present.

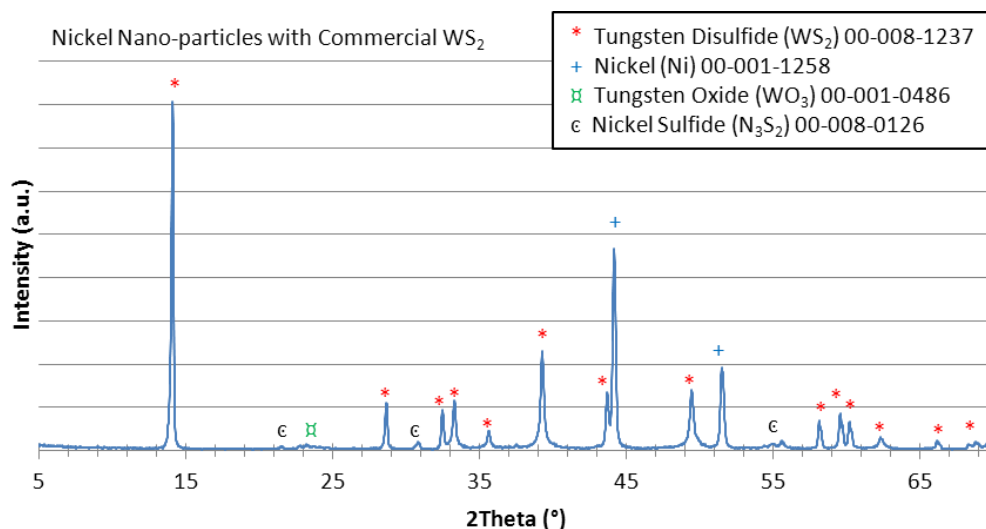


Figure 38. XRD pattern from the carbon growth with commercial tungsten disulfide. While the tungsten disulfide and nickel catalyst are still present, tungsten oxide and nickel sulfide are also present.

The inclusion of tungsten oxide is readily explained, as a result of the oxygen gas in the selected synthesis process. Nickel sulfide formation seems to be an outcome of nickel being exposed to a sulfur containing environment or a sulfide phase in the surroundings. Consulting the phase diagram, nickel sulfide, NiS, can be found in the appropriate environment at a temperature as low as 301.8 degrees Celsius (Figure 39). This means that at the initial 350 degree Celsius stage of the synthesis process, the formation of nickel sulfide is possible. At the operating temperature of 550 degrees Celsius, it is possible to form  $\text{Ni}_3\text{S}_2$ , as identified in the sample. While the inclusion of nickel sulfide is not necessarily detrimental to the development of a viable personal

protective armor, its appearance corresponded to a halt in the synthesis of carbon nanofibers. In order to better characterize what had occurred in these samples, additional experiments were conducted.

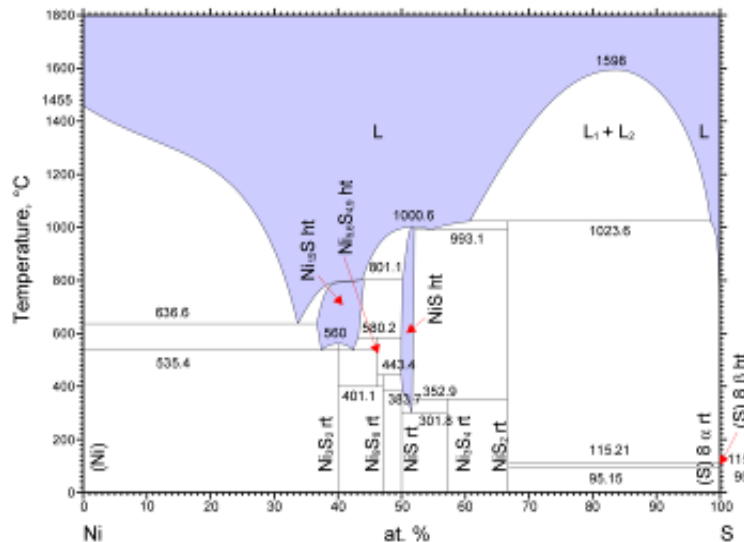


Figure 39. The binary phase diagram for nickel and sulfur. In the range of experimentation, nickel and sulfur will form into a nickel sulfide. Phase diagram courtesy of ASM Alloy Phase Diagrams Center. From [29].

In order to provide further characterization, the formation of nickel sulfide was reproduced in an experiment that raised the temperature of a nickel nanoparticle and tungsten disulfide mixture. The sample was heated to 350 degrees Celsius under nitrogen and argon-hydrogen gas for 60 minutes. This mirrors the initial treatment of the nickel nanopowder in the carbon nanofiber synthesis process. EDX spot analysis was conducted to confirm the existence of nickel sulfide in the sample. Analysis was conducted at both high and low magnification in order to identify regions of primarily tungsten disulfide and nickel sulfide, as well as to look for evidence of the transition in between the tungsten disulfide and the nickel nanoparticles. Lower magnification illustrated the divided regions of tungsten disulfide particles, as well as areas where nickel sulfide had formed (Figures 40, 41). The higher magnification images also gave insight into the processes at play through analysis of what appeared to be a small tungsten disulfide particle on the surface of a larger nickel sphere. Spot analysis showed a different ratio of

tungsten to sulfur that was noted in the bulk coupled with a high incidence of nickel (Figure 42). This combination of elements provided evidence that a transfer of the sulfur is occurring in between the two metals, resulting in the formation of nickel sulfide.

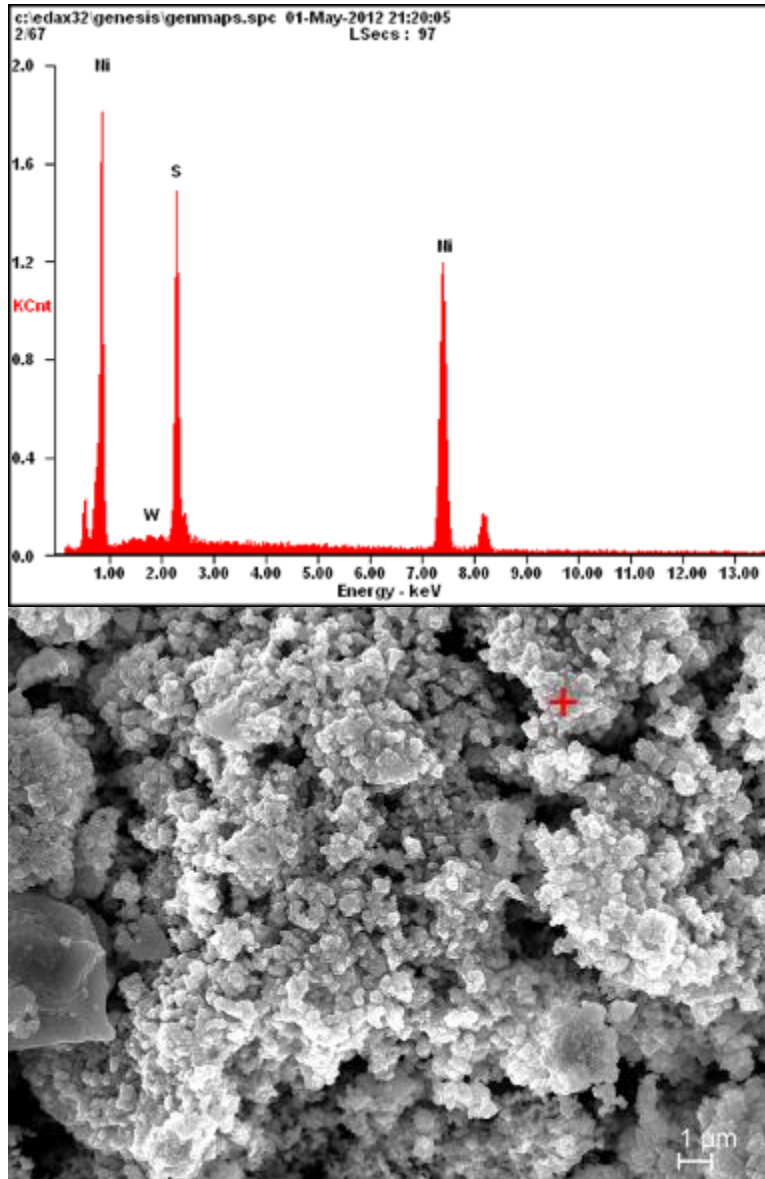


Figure 40. EDX illustrating the presence of nickel sulfide.

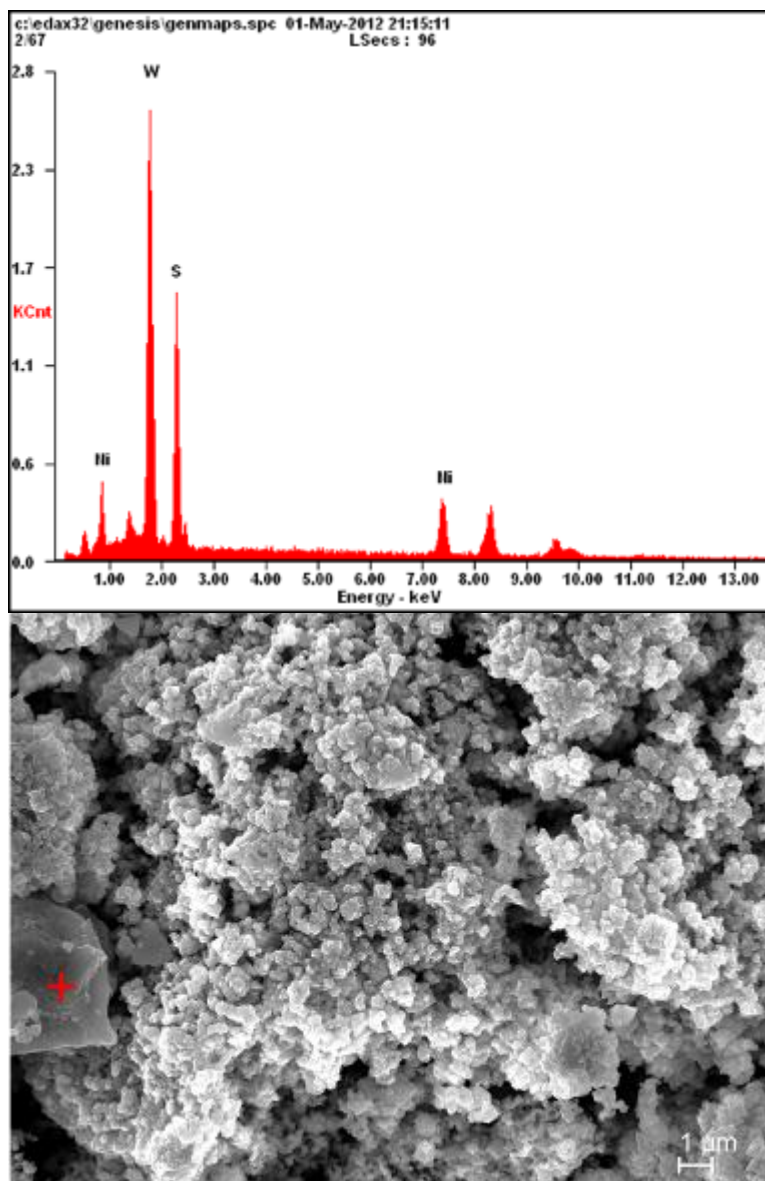


Figure 41. EDX illustrating the presence of tungsten sulfide.

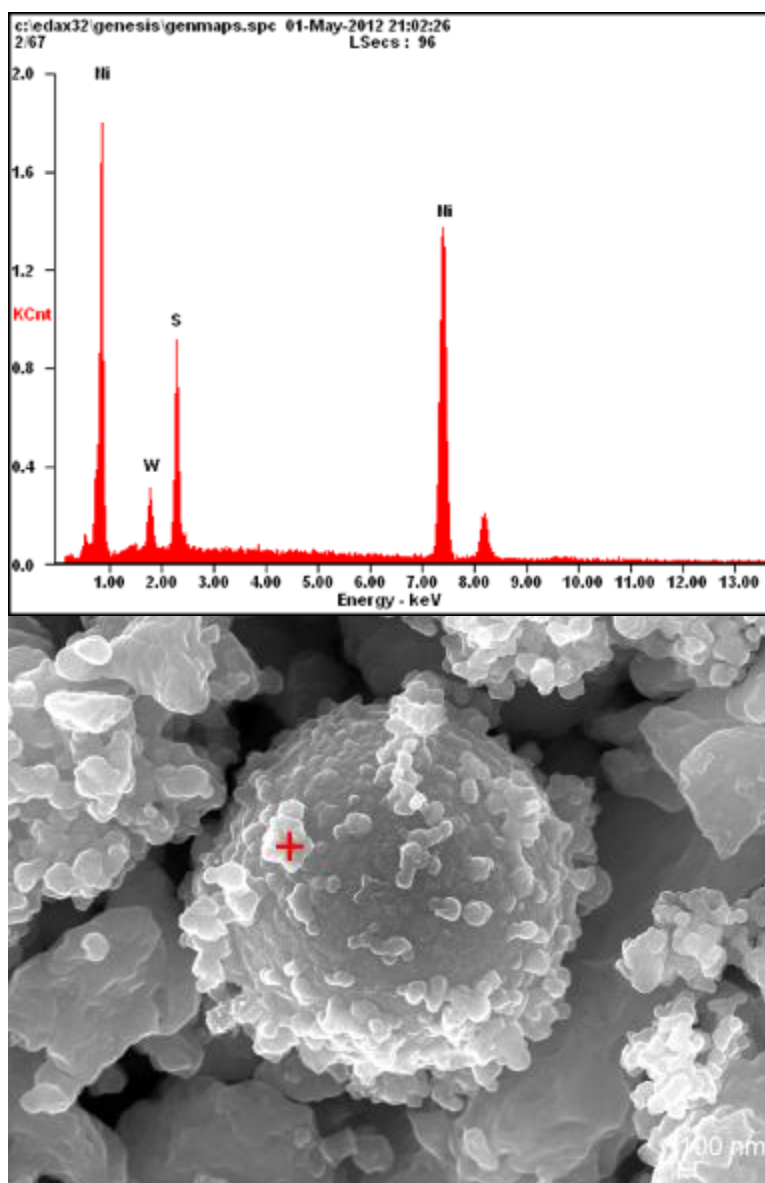


Figure 42. EDX illustrating the manner of formation of nickel sulfide from a tungsten disulfide particle.

The formation of nickel sulfide was clear on all of the exposed nickel surfaces (Figure 43). In the observed cases, the nickel sulfide agglomerated on the surface in protruding structures. The size of the nickel sulfide deposits varied, and seemed to depend on the nickel particles on which the sulfide formed. The larger spherical nickel particles formed larger globular deposits, while the smaller nickel particles formed nickel sulfide deposits that were much finer and fiber like. The

intricacies of the phase diagram show the possible formation of a variety of different species of nickel sulfide, especially given the reactive nature of the nickel nanoparticles. Low temperature, according to the phase diagram, i.e. 350 degrees, has more possibility to produce  $\text{Ni}_3\text{S}_2$  and higher atomic ratios of nickel and sulfur while higher temperatures are likely to produce  $\text{NiS}$ .

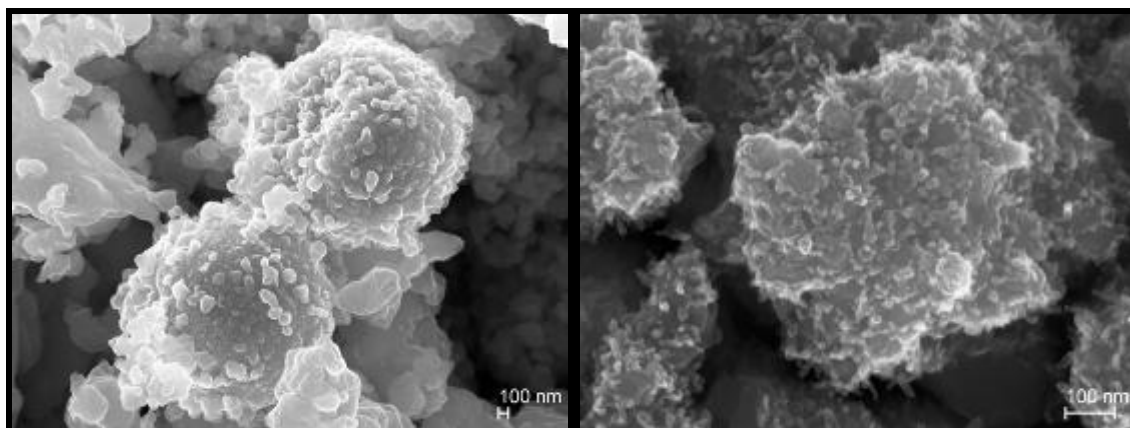


Figure 43. SEM images of nickel sulfide formations. The left image shows the agglomeration on sintered spherical nickel particles with nanoparticles in the background while the right image shows the nickel sulfide formation on sintered platelets of nickel particles.

As discussed before, the reason the synthesis process holds the sample at a temperature of 350 degrees Celsius, is first to provide a reducing atmosphere to eliminate the formation of any oxides, and then to coat the nickel nanoparticles with a layer of carbon. The second step is completed in order to prevent the sintering of the nickel into large particles, which would occur if the sample was raised directly to 550 degrees Celsius, without a surface layer of carbon. In this experiment, the SEM clearly shows that the initial heating stage in the reducing atmosphere provides the necessary energy for nickel sulfide to form on the surface of the samples. In this case, the nickel nanoparticles are coated with a layer of nickel sulfide prior to any exposure to the ethylene gas, which serves as the carbon source for the synthesis of fibers. No carbon deposits were formed on the surface of the samples with sulfur present, so the formation of the nickel sulfide layer can be directly identified as the reason for the prevention of the synthesis process.

This result had important implications to the course of the research. It was initially intended to pursue the decomposition of the ammonium tetrathiotungstate as the source of tungsten disulfide. While this process would provide the opportunity for the formation of tungsten oxide, it would prevent any secondary effects to the fibers or nickel particles in the latter sulfurization steps. Given that the nickel would sulfurize in the presence of the tungsten disulfide, this was no longer a viable option and further efforts would have to rely on the post treatment of tungsten oxide. In other words, the only viable *in situ* growth of carbon nanofibers and tungsten disulfide can be achieved using tungsten oxide as a tungsten source, nickel as a carbon growth catalyst and a sulfurization step to convert the former into tungsten disulfide once the fibers were grown from the catalyst particles. To summarize, the entire growth process from precursor to product can be found in Figure 44.

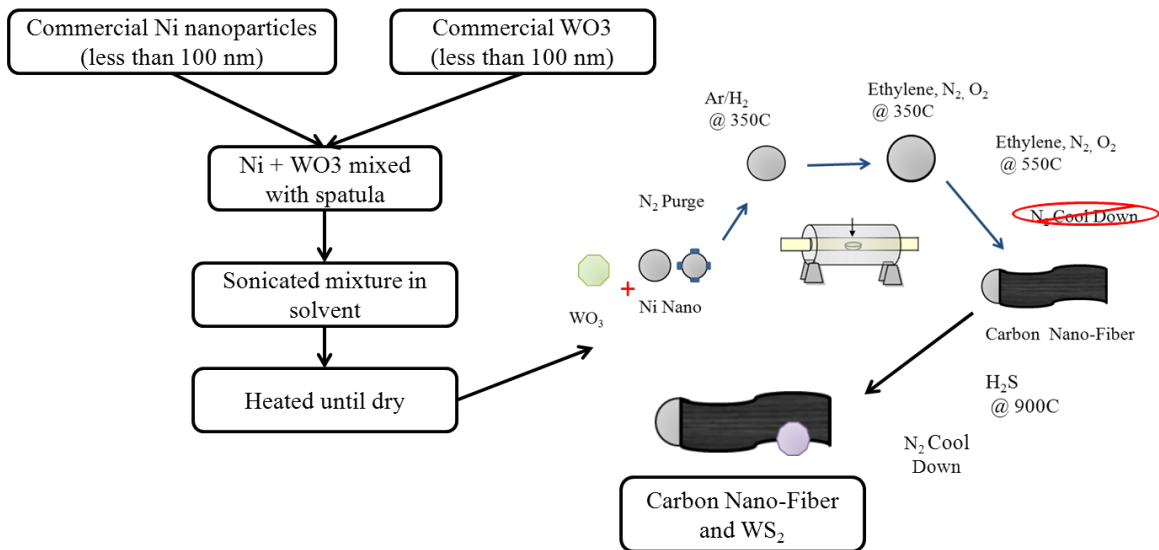


Figure 44. A flow diagram of the carbon fiber and tungsten disulfide composite synthesis.

***b. Sulfurized Carbon Nanofibers with a Nickel Nanoparticle Catalyst***

Once it was determined that the source of tungsten disulfide would be the conversion of tungsten oxide via a sulfurization process, it was prudent to analyze the

effects of the sulfurization process on the carbon nanofibers. In order to characterize this effect, carbon fibers were synthesized from nickel nanoparticles in the presence of oxygen as outlined in the experimental procedure. The fibers were then sulfurized in the sulfurization process outlined in the procedure. The resultant was then analyzed in both the SEM and the XRD. The SEM showed a fiber structure similar to that of the basic carbon fiber growth. The bulk of the fibers were in the 200 nm diameter range and there were pockets of smaller 10–15 nm diameter fibers as well (Figure 45). The images selected do not show the inclusion of the larger micron diameter fibers, but they were present in the sample. This result was expected, as the fibers were grown in the same manner as previous experiments and the sulfurization process was not completed at temperatures high enough to impact the fibers once they had been grown. At the same time, the images did show signs of microstructural features that had not been seen on other experiments.

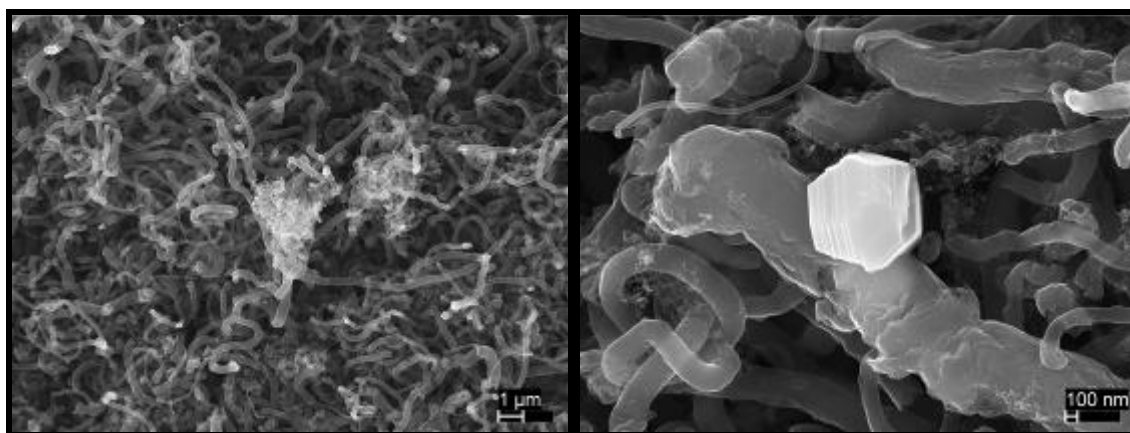


Figure 45. SEM images of sulfurized carbon nanofibers grown with a nickel nanoparticle catalyst. The left image shows the fiber distribution, while the right image shows the inclusion of a different type of nickel sulfide.

The purpose of the sulfurization is to sulfurize the tungsten oxide, but if the sulfur is present in the system, it is possible to sulfurize other species as well. While the bulk fibers were similar, there was a distinct change with the inclusion of three dimensional hexagonal crystalline structures. Utilizing the EDX capabilities of the SEM, it was possible to identify the presence of nickel and sulfur in these crystals. Reverting



once again to the phase diagram, there were a range of nickel sulfides that can be formed at the temperature of 900 degrees Celsius. The inclusion of nickel sulfide,  $NiS_2$  and  $Ni_{17}S_{18}$ , was determined from analysis using the XRD (Figure 46). While it was clear that both phases of nickel sulfide are present, it is difficult to determine which phase is predominant using only the XRD pattern. It was also possible that some of the sulfur present in the system became attached to the carbon fibers, but this effect was unconfirmed. Overall, the sulfurization process caused a 1.508 gram sample of carbon fibers, grown with a nickel nanoparticle catalyst, to gain 0.020 grams of sulfur.

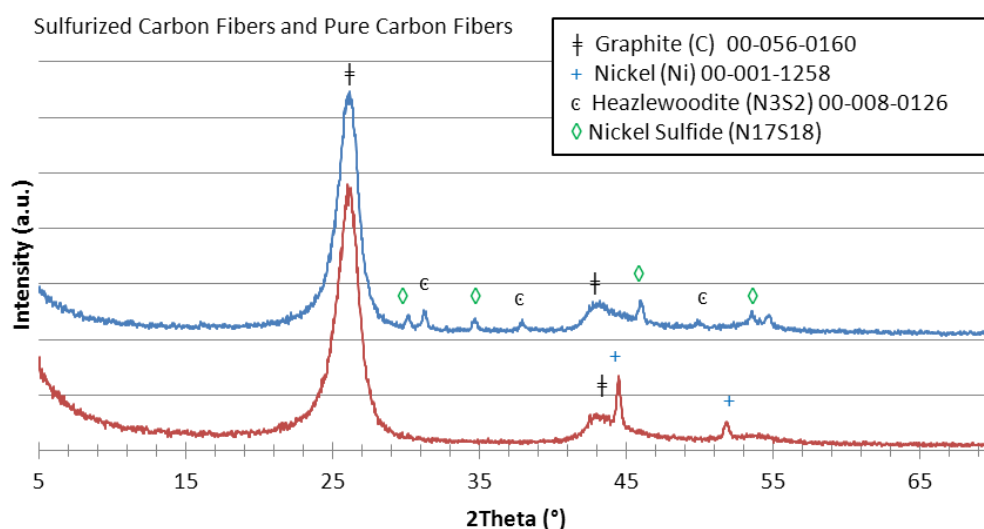


Figure 46. XRD pattern from carbon fibers and the sulfurized carbon fibers. While the predominant peaks are from the carbon nanofibers, two forms of nickel sulfide are also present.

*c. Sulfurized Carbon Nanofibers with Tungsten Oxide in situ with a Nickel Nanoparticle Catalyst*

Once it had been determined that the tungsten oxide could be successfully sulfurized and that the process required to do so would not have a detrimental effect on the carbon nanofibers, the next step was to form a full nanoparticle composite. The full synthesis of the composite would be a carbon nanofiber synthesis with a mixture of nickel nanoparticles and tungsten oxide and a subsequent sulfurization step. At this stage,

little information was known about the appropriate ratio of tungsten disulfide to carbon nanofibers. As a result, a survey of three different compositions was tested. The first composition utilized 0.050 grams of both nickel and tungsten oxide, the second was 0.050 grams of nickel to 0.025 grams of tungsten oxide, and the final composition was 0.050 grams of nickel to 0.0125 grams of tungsten oxide. Each of the three composites was tested using XRD and SEM.

The XRD analysis of the materials was indicative of the differing crystal structure in each case. As mentioned previously, the inclusion of tungsten oxide into the carbon nanofiber synthesis process modified the structure of the carbon fibers. This change is evidenced in the XRD patterns of the three samples (Figure 47). The highest loading of tungsten oxide resulted in the graphite peak with the lowest intensity, while the lowest loading of tungsten oxide showed the highest intensity peak. The difference in peak intensity could be correlated to a different extent of crystallinity in the structure. Also of note is the intensity of the peaks for the tungsten disulfide. The peak intensities correspond well to the level of tungsten oxide initially placed into the sample. Finally, the most notable difference is the nickel sulfide peaks. These peaks were evident in the middle and lowest loading, but have a much lower intensity in the highest loading case. There is also a transition from primarily  $N_{17}S_{18}$  in the lower loadings to primarily  $N_2S_3$  in the highest loading. The reasons for this transition were not fully understood and required further testing to quantify.

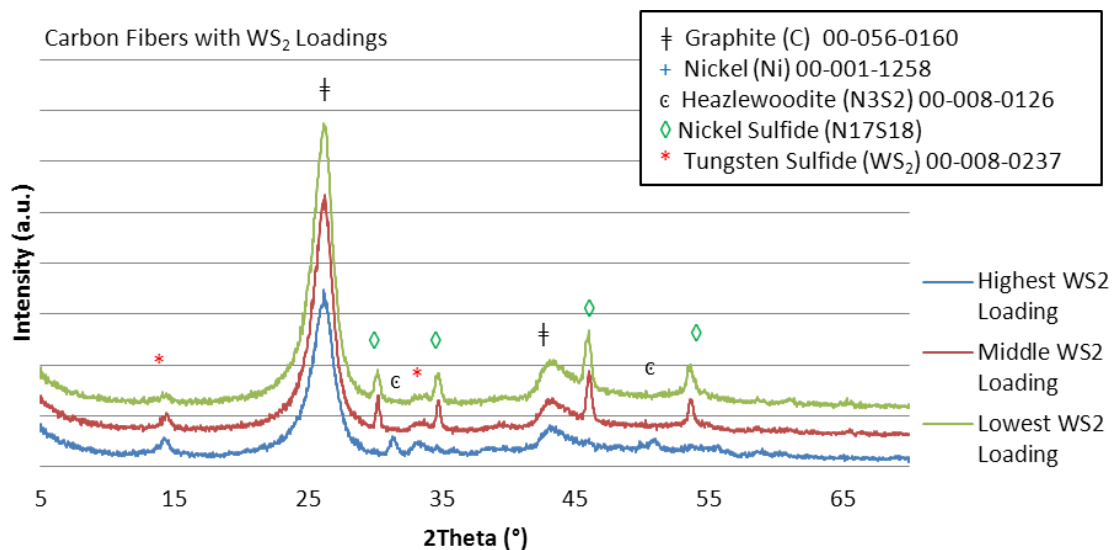


Figure 47. XRD patterns for each of the three loadings of tungsten disulfide and carbon nanofibers. The bottom line has the highest loading, the middle line the middle loading, and the upper line the lowest loading.

The presence of sulfides was also noted from the SEM images of these samples (Figure 48). While tungsten disulfide is not visible in the selected image of the lowest loading, it does have an excellent example of the formation of nickel sulfide. It can be seen in this image, as well as the image of the middle loading, that carbon fibers with similar diameters to that of the nickel sulfide particles appear in close proximity. These fibers seem to have been broken perpendicular to their length and given the relative positioning, were most likely attached to the nickel particles prior to the sulfurization. This suggests that when the nickel nanoparticles were sulfurized, they became detached from the carbon fibers which grew from the nickel. Again in the image of the middle loading, tungsten disulfide is not readily visible. In the highest loading however, tungsten disulfide is a clear constituent. In the upper right and center of the image flat, jagged edged shapes can be seen.

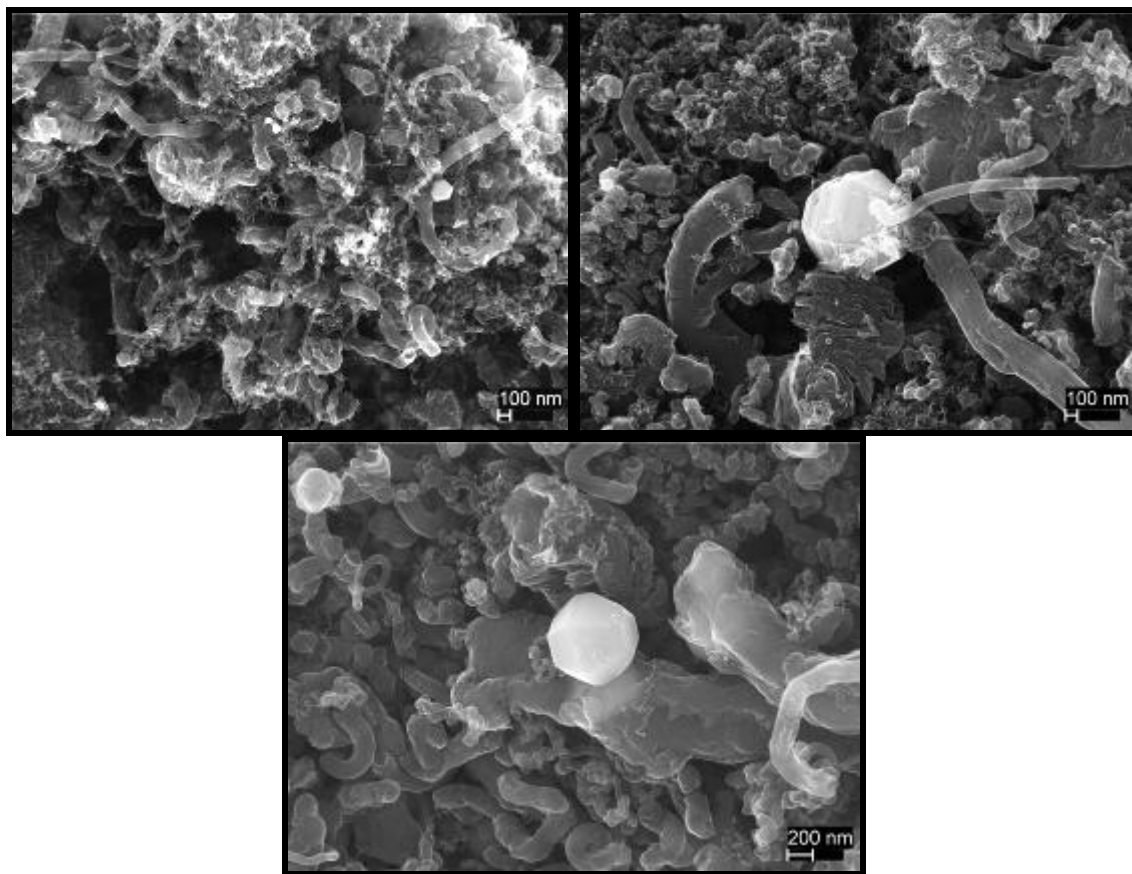


Figure 48. SEM images from the three different loadings of tungsten sulfide. The upper left image is the highest loading, the upper right image is the middle loading, and the lower image is the lowest loadings.

Another image, taken from a different region in the lowest loading, represents the structure of the tungsten disulfide particles (Figure 49). In order to make a finer analysis of the composites, the regions around the tungsten disulfide particles were reviewed more closely. The lowest loading was in large part comprised of carbon nanofibers with a size distribution akin to that of pure carbon fiber synthesis, but pockets of tungsten disulfide were found scattered throughout the sample. In the areas adjacent to the tungsten disulfide, the morphology of the carbon was different. This image is indicative of the state and effects of the tungsten disulfide in the samples. The first aspect noted was the lack of well-defined carbon fibers. Previous images showed that the bulk composition of the lowest loading was most closely akin to that of a pure carbon fiber synthesis. In this image, the left half is comprised of amorphous carbonaceous deposits

and the right half is mainly tungsten disulfide. This result is most likely a product of the proximity to the tungsten oxide particle during the carbon fiber synthesis. The effects of the inclusion of tungsten oxide as a precursor, was noted in all of the tested tungsten disulfide loadings. The effect also seemed to be more prevalent in the highest loading and was the least notable in lowest loading.

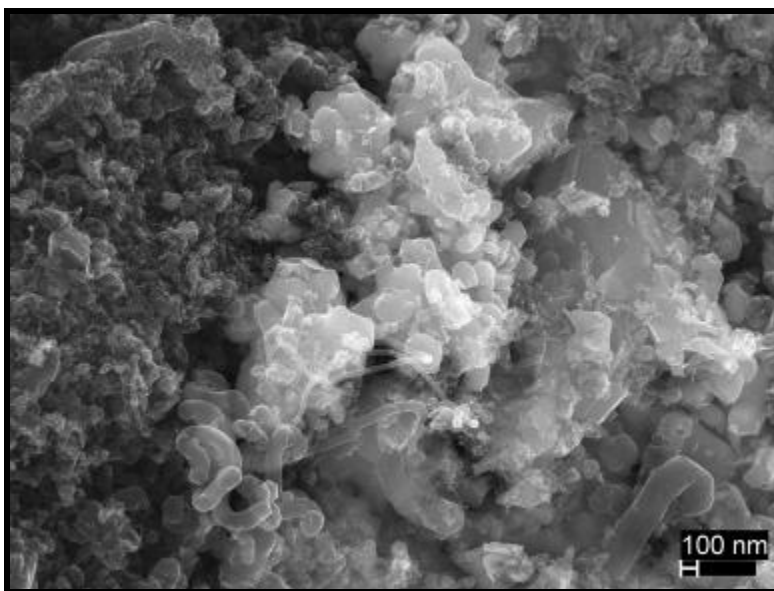


Figure 49. SEM image of tungsten disulfide particles present in the composite with the loaded loading of tungsten disulfide particles.

The SEM imagery of the tungsten disulfide particles also provided information about the morphology. There are a number of larger particles, most notably the partially covered micron size particle in the right-center (Figure 50). At the same time, there are a number of 100–200 nm diameter particles scattered throughout the center and right side of the image (Figure 50). While the conditions were appropriate for the formation of tungsten disulfide spheres, there is also evidence of the formation of platelets similar to what was found in the commercial product. It is also quite possible that, given the initiation site, the fine white fibers in the center of the image are actually comprised of tungsten disulfide. Further development will be required in order to refine a procedure for development of a consistent morphology.

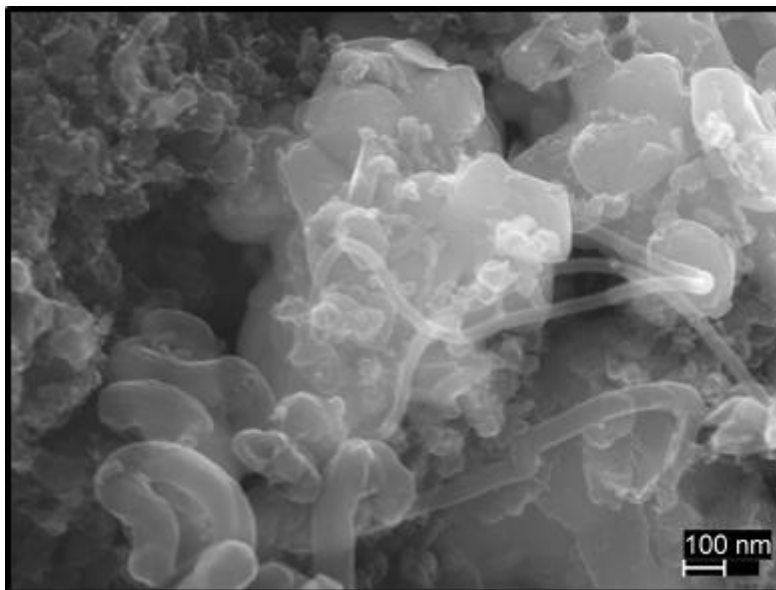


Figure 50. SEM image showing the variability of the morphology of the tungsten disulfide particles.

#### **4. TGA Testing**

Personal protective armor materials can often operate under conditions with elevated temperatures as a result of heating from the transfer of energy from a projectile. Consequently, it is important the nanocomposites are thermally stable. TGA testing was conducted to determine the properties of the pure carbon fibers, sulfurized fibers, and the tungsten disulfide and carbon fiber nanocomposite (Figure 51). The three tests were normalized to the pure carbon fibers for comparison purposes. In each case, thermal breakdown does not occur until approximately 500 degrees Celsius in an oxygen rich environment. After that point, the three samples breakdown at different rates. Conditions that effect thermal stability of the nanocomposite are carbon fiber burn-off, oxidation of tungsten disulfide to tungsten sulfide, and conversion of nickel sulfide to nickel oxide. While these processes are identified, the synthesized materials show a clear ability to maintain integrity at elevated temperatures.

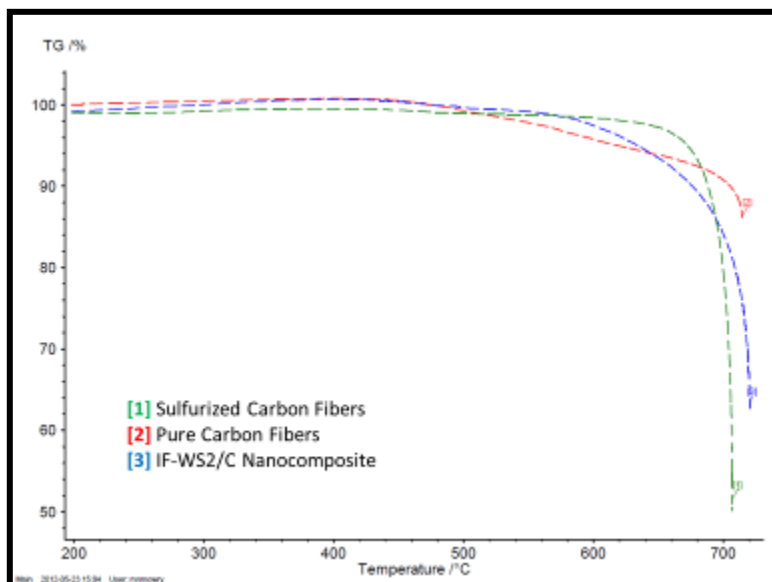


Figure 51. TGA analysis of pure carbon fibers, sulfurized fibers, and the tungsten disulfide and carbon fiber nanocomposite. All three are thermally stable until approximately 500 degrees Celsius.

## 5. Sample Selection for Continued Testing

In order to fully understand the effects of the different structures and compositions of the nanoparticles and nanocomposites for potential application in a shock absorbing system, a number of samples were selected for further testing. While there might be future possibilities to utilize the commercial tungsten disulfide and tungsten disulfide from the ammonium tetrathiotungstate, further efforts were discontinued. Likewise, the products from the attempts to synthesize carbon fibers from a blend of nickel nanoparticles and tungsten disulfide were not considered. This decision was based on the inability to form carbon fibers *in situ* with the sulfides. The only method in situ growth the proved to be viable was the inclusion of tungsten oxide with the nickel nanoparticles followed by a complete growth process and then subsequent sulfurization. In order to establish a baseline, the pure carbon nanofibers with no additional modifications were selected. To validate the utility of any efforts to this point, the nanocomposites must have performance characteristics superior to a pure carbon nanofiber. The impact of the inclusion of tungsten disulfide particles has not been well

defined and as a result the three different loadings were selected to test further. While the structure of the carbon in each of the samples differs, there is no clear indication from the characterization as to which of the three samples would provide the greatest benefit. Finally, the sulfurized carbon nanofibers were selected. The sulfurization of the tungsten oxide had secondary effects such as the deposition of sulfur and the formation of nickel sulfide in the pure carbon fibers. In order to distinguish the effects of the tungsten disulfide from the other modifications to the carbon nanofibers, this sample was required.

## B. SAMPLES FOR MECHANICAL TESTING

This section will discuss the development of mounting methods utilized to form a specimen containing the carbon nanofibers and tungsten disulfide nanocomposite for use in mechanical testing (Figure 52).

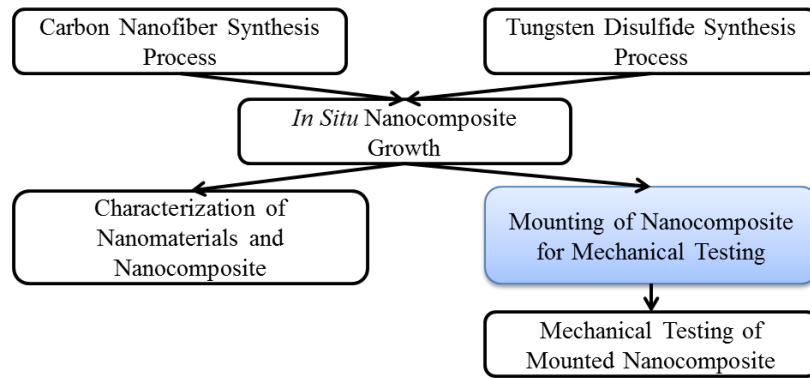


Figure 52. A discussion of nanocomposite mounting methods.

### a. Carbon Nanofiber and Tungsten Disulfide Pellets

By compressing the nanocomposite into a pellet, the mechanical properties of the materials could be directly tested without the need to account for any other medium. It would also be possible to identify the fracture mechanics of the nanocomposite in postmortem review of the gas gun testing. However, in each case the materials were not compacted well enough to form a pellet and they flaked away when gently prodded. Further attempts to form pellets were discontinued, as the elevated pressures deformed the structure of the nanocomposite. It is possible that increased



pressures on the samples would have resulted in more compacted pellets but this remains uncertain. It is also possible that further compaction of the materials would result in unwanted fracture or deformation of the constituent nanoparticles.

***b. Mounting Nanomaterials into an Epoxy Matrix***

Another approach was to embed the nanocomposites into a polymer matrix. The inclusion of nanoparticles into a polymer matrix is a widely pursued field of research. The improvement in the strength with the addition of the carbon nanofibers comes as a result of the structure and bonding mechanisms of the polymer chains. Polymer materials are comprised of a number of tangled and intertwined carbon chains with various functional groups attached. Within a carbon chain, the primary method of bonding is covalent bonding. In between chains, secondary bonding, such as Van der Waals, dominates. In contrast, carbon nanofibers are comprised of graphitic covalent bonds for the majority of the structure. With appropriate processing, the strengthening of the polymer comes as a result of load transfer [30]. When placed under tension or compression, the weaker polymer will alter its shape prior to that of the carbon nanofibers. As a result, the load will shift from the bulk polymer to the reinforcing agent. The carbon nanofibers are much stronger, so the overall strength of the material will improve. This process is limited by the ability of the carbon nanofibers and the polymer chains to cross-link with one another. This effect, known as interfacial strength, is notable in steel reinforced concrete. The concrete attaches to the steel rods resulting in improved properties over the base material and subsequently reinforced concrete enjoys widespread use. The tri-modal distribution of fibers should serve to provide a large surface area for adhesion to occur and consequently provide a higher interfacial strength than bulk fibers.

The inability to form pellets resulted in a shift in emphasis to determine a viable method to mounting the samples in epoxy. In instrumented indentation, it is common to mount a small sample into an epoxy in order to meet sample holder requirements in the indenter. In this case, instead of isolating the nanocomposite, a concerted effort was made to distribute the sample throughout the epoxy evenly. In this case, the impact of a particular nanocomposite could be identified by comparison to the

bulk epoxy resin. The major obstacles that were overcome were the loading of nanoparticle into the epoxy and the method to achieve the required dispersion.

The quantity of the nanoparticles to be added into the epoxy was determined through experimental testing. In [31], carbon nanotubes were added to an epoxy matrix to study the effects on mechanical properties. Given the amounts of carbon nanotubes added into the epoxies in that research, a nanoparticle loading of three weight percent was selected as an upper limit. As a test, a sample was prepared with a three weight percent loading of fibers corresponding to the case with the highest storage modulus. After proceeding through the epoxy puck forming process, two molds were poured. After a period of 24 hours, the epoxy was not set in either mold. The sample was then left for another 24 hour period, and after it had failed to harden again was placed under a vacuum and left for an additional 24 hour period. Once the sample had failed to set under the vacuum, it was determined that the curing process had been hampered and the samples were removed from the molds (Figure 53). Each of the samples exhibited similar physical attributes. The top and bottom surfaces of the samples were left in a viscous liquid state similar to that when the samples were initially poured. The middle of the sample hardened to an extent, but was still not of the same hardness shown by other epoxy pucks and could be easily dented or scratched by a human fingernail.

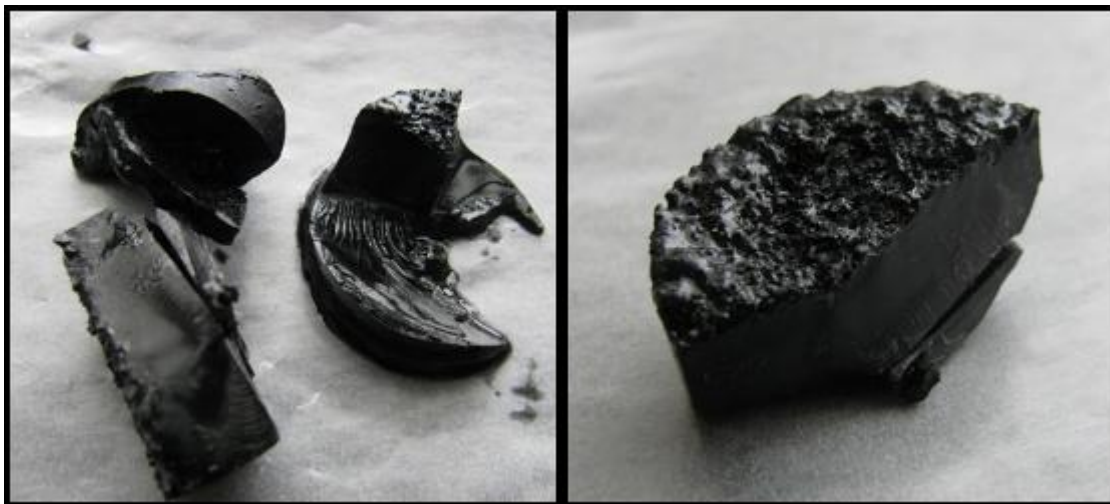


Figure 53. The attempt to form epoxy pucks with a three weight percent loading of nanoparticles. In this case the epoxy did not set correctly. The left image demonstrate the harder region of semi-set epoxy. The surface of puck in the right image shows a high density of carbon fibers and an unset epoxy.

As a result, the loading of the nanoparticles into the epoxy was reduced. The reduction in the weight percent of fibers is consistent with the results found in the paper published by [30]. Their research evaluated the performance change in nanotube reinforced epoxy composites for a different range of loadings. The weight percentage of the nanoparticles to the epoxy was ranged from 0.1 to 1.0 percent. Testing showed a decrease in modulus for the 0.1 and 0.5 weight percent cases, but an increase for the one percent case. Based on these results, the weight percent for future loading was set at a value of one percent of nanoparticles to epoxy.

There was also a disparity in between the stated working time and the experimentally observed working time. Once a one weight percent loading was selected, the focus shifted to achieving a uniform dispersion. In general, the best dispersions were achieved by leaving the epoxy and nanoparticle in the sonicator for the longest period of time possible. In the pursuit of the best dispersion possible, it was initially decided that the nanoparticle and epoxy mixture should be sonicated for a period of 15 minutes. This would result in a total working time of less than 20 minutes, one third of the total state working time. In the initial test of this method, the epoxy cured in the cup in the sonicator prior to the completion of the 15 minute mixing period. In order to maintain the benefits of sonicating the samples, the time of the second sonication was shortened to five minutes. The premature hardening of the epoxy was likely a product of the sonication process. In addition to mixing the nanoparticles into the epoxy, it is also providing for better dispersion of the hardening agent into the resin. This improved dispersion was credited in this case for the expedited curing of the epoxy.

At the conclusion of the polishing process, there were still polishing marks across the surface of the sample that could be seen under 10 x magnifications. These polishing marks were attributed to the mechanical properties of the epoxy matrix. The hardness of the epoxy is only a fraction of that expected from a metal and as a result, was not as capable of holding a mirror finish. As a result, the samples were used in the slightly rough state for mechanical testing.

## C. MECHANICAL TESTING OF NANOPARTICLES AND NANOPARTICLE COMPOSITES IN AN EPOXY MATRIX

The results of the mechanical testing will be discussed in this section (Figure 54). Both nanoindentation and gas gun testing was utilized for determination of mechanical properties.

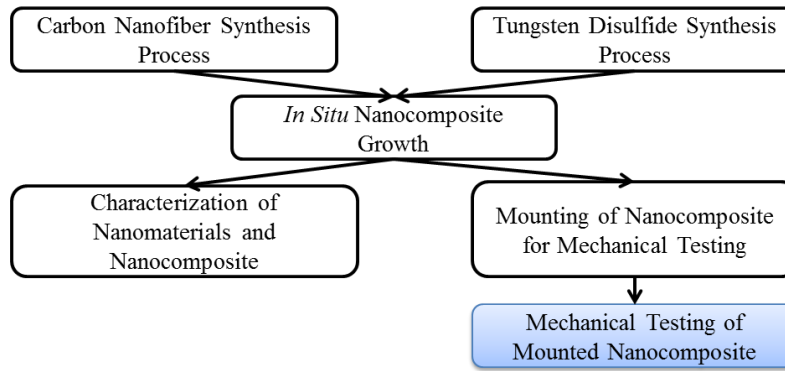


Figure 54. This section will discuss the mechanical testing of the mounted nanocomposites.

### 1. Nanoindentation

Testing from nanoindentation provided remarkable results. As expected, each of the loadings of nanoparticles or nanocomposites improved both the hardness and modulus of the base epoxy. While carbon nanofibers alone increased the modulus by 29% and the hardness by 114%, the addition of tungsten disulfide improved the modulus by 99% and the hardness by 247% over the base epoxy.

#### a. Flat Punch Complex Modulus

The flat punch testing was useful for two main reasons. First, the storage modulus testing from the complex modulus method demonstrated an increase in modulus from the addition of different nanocomposites and only minor effects from frequency dependence. However, many of the indents had to be discarded as a result of the surface characteristics and the spacing in between indents. The second notable result from the complex modulus testing was the determination of loss modulus. This value is important

because if the value is essentially zero, then the basic testing parameters can be used based on the assumption of elastic behavior. To illustrate the results, the middle frequency, 6.708 Hz, was selected as representative of the sample (Figure 55). The measure of the loss modulus as a function of the storage modulus is known as the loss factor. At this frequency, the largest loss factor was present in the pure epoxy and was approximately two percent. The small loss moduli, especially when compared to the values of storage moduli, illustrate a primarily mathematical phenomenon, not a material property. The loss modulus is dependent on the sine of the phase angle. As the phase angle goes to zero, this measurement becomes very sensitive to any deviation and will generate non-zero values. Overall, the minimal values of loss modulus verify the assumption that the loss modulus can be assumed to be zero and the complex modulus can be directly related to the reduced modulus.

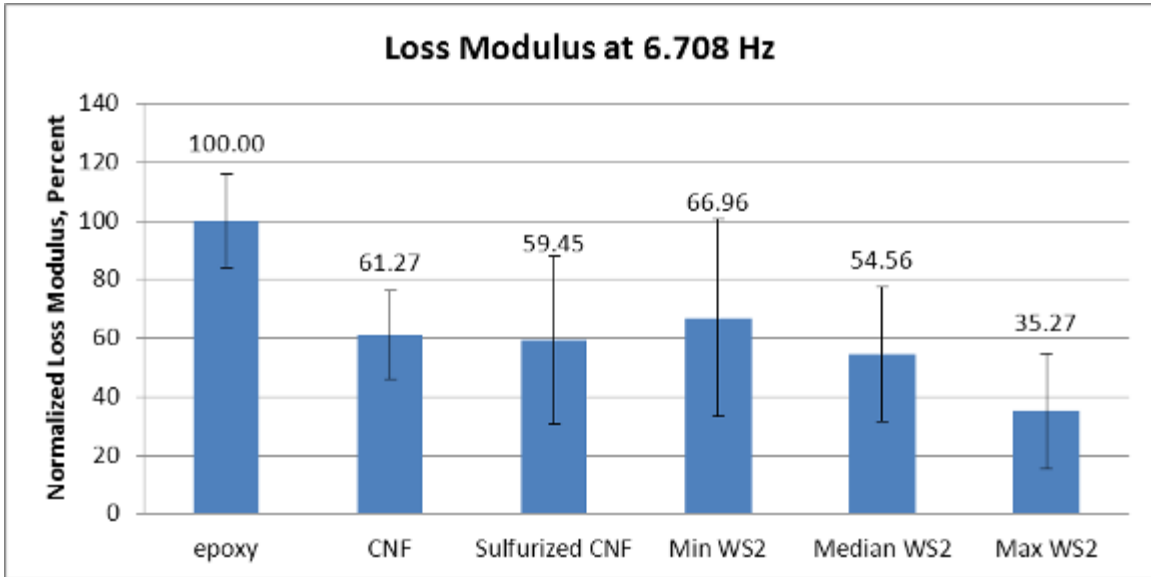


Figure 55. The loss modulus at a frequency of 6.708 Hz. The scale is normalized to the pure epoxy which has the largest loss factor of two percent.

There were a number of potential sources of error for the complex modulus measurements. Despite sonicating the samples, the dispersion of the nanocomposite on the surface of the samples was non-uniform. As a result, it was important to select an area on the sample that would provide a consistent dispersion in

order to collect comparable results. Given the size of the indenter tip, as well as the spacing in between indents, this was not always achievable. As a result, it was necessary to review the locations of the indents and to remove the indents that had fallen onto a dissimilar surface. An example would be that points lying in pure epoxy were discarded for testing on the samples with loadings. Further potential sources of error arose with the size of the indenter tip. Depending on the modulus of the material tested, it was possible that in order to form an indent in the sample, a higher load will be required than the machine can produce. The required loading was a result of the material's contact stiffness. Contact stiffness is the product of the area of the indenter in contact with the material and the storage modulus. This places bounds on the utility of different indenter tips, for example a 50 micron flat punch cannot be used to test the modulus of a high strength steel alloy. Larger values of contact stiffness required more force from the machine to create an indent. After the data had been taken, it was confirmed that the load bounds of the instrument had not been exceeded in these tests and the results were valid. However, the materials did approach the limit and any further increases in modulus could produce error from this effect.

***b. Modulus and Hardness at Depth***

The issues experienced in taking the data using the complex modulus testing were not present in the testing using the basic hardness and modulus. The use of a smaller Berkovich tip resolved the issues of contact stiffness and reduced the spacing in between points allowing for more accurate testing within a single continuous distribution of fibers. This improved accuracy led to more consistent results and smaller deviation in between measurements. The data taken from the complex modulus testing established that the loss modulus was near zero, especially for the samples with included fibers. This result confirms the validity of the assumptions for of the basic modulus and hardness testing method. While the complex modulus concerns were resolved, other sources of error were manifest in the testing. One of the primary concerns was residual viscoelastic effects. In the testing, the indenter tip was pushed into the material and then the position was maintained prior to the start of unloading. During this time, the viscoelastic

properties of the material allowed it to creep to return to a lower stress state. This small effect could manifest in the slope of the unloading curve. The elastic modulus is sensitive to this slope and these effects could result in a higher modulus than was actually present in the material. Fortunately, even if present these effects would be slight due to the highly elastic nature of the materials tested. The effect would also appear in all cases maintaining the validity in comparisons of the values. The hardness measurement could also be effected by a drift correction coefficient. Based on the testing method, this correction was automatically made to account for some of the effect of thermal drift. In this case, the impact of the correct was small and the calculations were left in the standard operating state.

Determining the properties of the epoxy matrix was not the focus of this research, but rather the improvement from the dispersed nanocomposites. To facilitate this comparison, the elastic modulus of the epoxy puck was normalized to be equivalent to a 100 percent value. Each of the different loadings was also normalized to this value in order to provide information about the change in properties as a result of the loading (Figure 56). The error bars are plotted to encompass a total range of two standard deviations. In every case, the included nanoparticles revealed an increase in the modulus of the epoxy puck. The carbon nanofibers showed the smallest increase of approximately 29 percent improvement, while the sulfurized fibers showed an improvement of nearly 52 percent. In the lowest loading of tungsten disulfide, the modulus increases further to almost 100% more than that of the pure epoxy. This was the highest modulus recorded with a value outside of the statistical deviation of the next highest value. While there is variance in the three loadings, even the lowest improvement in modulus is still a 71% increase over pure epoxy and a 20% increase over sulfurized fibers.

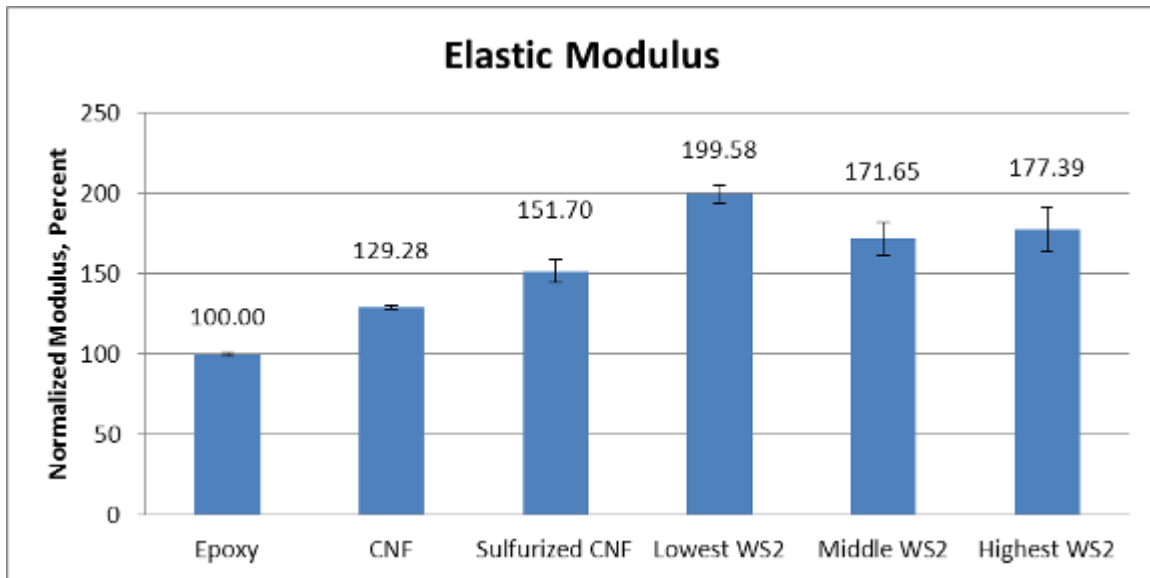


Figure 56. The elastic modulus from the basic modulus and hardness testing. The scale is normalized to the pure epoxy.

The nanoindentation results could also be used to find the hardness of the material. The hardness is simply the load on the indenter tip divided by the contact area. In order to compare the hardness of the materials, the epoxy was once again normalized to the 100 percent value (Figure 57). The error bars are plotted to encompass a total range of two standard deviations. The trends noted in the changing modulus are reflected in the hardness. The initial addition of carbon nanofibers had a large effect and increased the hardness by more than 114%. The addition of sulfurized fibers further increased the hardness but only by another 38%. When tungsten disulfide was present in the material, however, the hardness showed another significant increase. For the hardest case, the lowest loading of tungsten disulfide, there was a 247% improvement over the pure epoxy, or a 95% increase over the sulfurized fibers. While the three tungsten disulfide loadings vary, all three values demonstrate hardness values of at least an additional 211% over the hardness of the epoxy. The deviation of the measurements overlaps for the three loadings of tungsten disulfide, but the values were distinct from the deviation of other loading types.



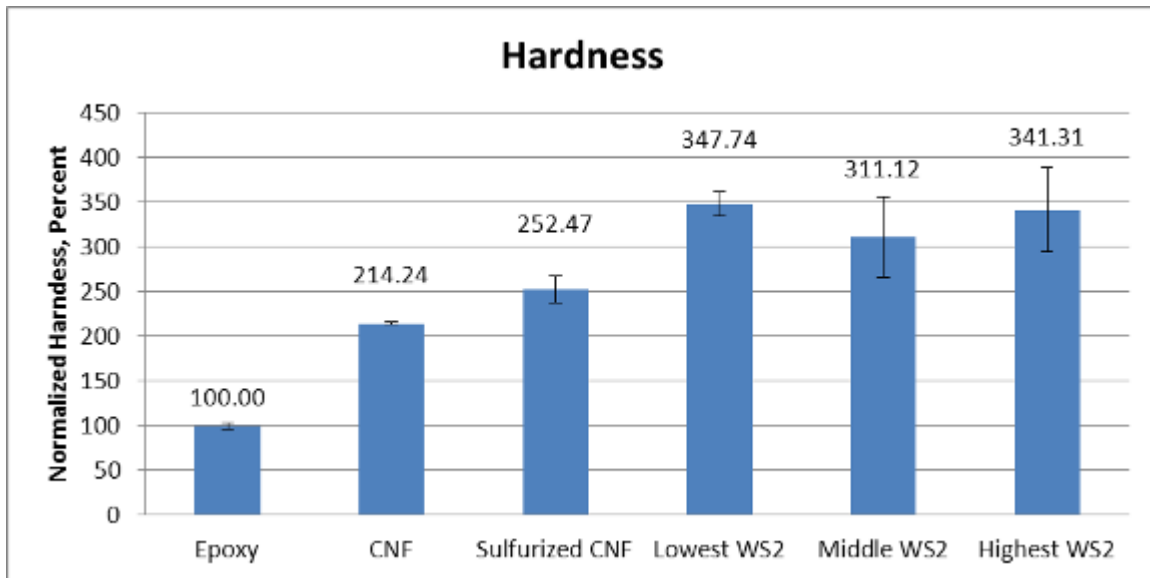


Figure 57. The hardness from the basic modulus and hardness testing. The scale is normalized to the pure epoxy.

There were a number of possible explanations for the increase in the modulus and the hardness of the different loadings. The principle of interfacial strength provided an answer for a good deal of the improvement. The pure carbon nanofiber loading showed improved performance primarily due to this factor. As with the example of reinforced concrete, the nanofibers are stronger than the surrounding composite and can maintain a higher stress state. The sulfurization of the fibers appears to improve the ability of the fibers to bond with the epoxy matrix, further improving the interfacial strength. The increase in hardness could also be partially due to the inclusion of nickel sulfide particles. While these particles contribute to an increase in performance in this case, it is possible that negative effects may appear under different situations. Nickel sulfide contamination is an ongoing concern for the tempered glass industry. Certain forms of nickel sulfide can develop in the glass manufacturing process and become included in tempered glass. This inclusion will result in a stress concentration and if the particle is of a certain size, the pane of glass will shatter under loading far below what is expected of the material [32]. Depending on the future inclusions of these materials into different matrixes, the possible impact of sulfide particles as stress concentrators should be considered.

The three different loadings of tungsten disulfide also provided a range of different results. The nanoindentation testing did not illustrate a clear trend in hardness or modulus as a result of loading. The lowest loading showed the greatest improvement, followed by the highest loading and then the middle loading. The lowest loading had the smallest deviation of the three cases, but for the hardness values, the deviations all overlapped. This suggested that the hardness values of all three loadings were not statistically different. At the same time, the modulus deviations did not all overlap and the lowest loading was outside of the deviation of the other two loadings. In this case, the middle and highest loading showed similar moduli. An underlying possibility to account for the difference in properties could be that the samples were not equally dispersed into the epoxy and that the tested regions were representative of local, not bulk, properties. It is also possible that these results indicate an optimal loading condition of the nanocomposite in the epoxy matrix.

While it was clear that the addition of tungsten disulfide improved the performance of the samples, the reason for the improvement was not apparent. It was possible that the inclusion of the tungsten disulfide actually served to improve the crystallization process of the resin, as was found to be the case with molybdenum disulfide in polyoxymethylene plastics [33]. The increase could also have been a product of hard, dispersed tungsten disulfide particles inhibiting the ability of the sample to deform. This process would mirror that of a precipitation or dispersion strengthened metallic alloy. The final possibility was that the tungsten disulfide has a greater interfacial strength with the epoxy, resulting in better load transfer similar to what was noted with the inclusion of sulfurized versus pure carbon fibers.

## **2. Gas Gun Testing**

The most relevant information that could be garnered from the gas gun testing would be the ability of the nanocomposites to dissipate an incident shock wave in the epoxy. This would require that sensors be placed on the back surface of the sample in order to determine the loss through the material. At this point, the facilities used are under development and will be instrumented to collect shock dissipation data in the

future. However, the postmortem of the epoxy pucks was still useful to empirically determine the effects of shock on the various loadings. The nanocomposites tested were the pure carbon nanofibers, the sulfurized carbon nanofibers, and carbon nanofibers with the highest and lowest loadings of tungsten disulfide.

The images of the epoxy slices provided a great deal of information about the manner in which fracture occurred. The aluminum sample holders were clearly deformed after impact and as a result could only be used once (Figure 58). While the surface of the sample holder was initially flat, after impact the slug deformed the surface to include a ring. This ring was elevated above the surface of the sample holder and indicates the displacement of the metal away from the site of the impact. To reiterate, the slug weighted 480 grams, impacted the sample holder at a velocity of 370 meters per second, and created a shock pressure of 700 MPa at the sample. Interestingly, none of the samples were completely broken after being fired upon in the gas gun. All of the samples did display signs of impact and most had small flakes of aluminum on the front surface. The images of the slices were taken of the surface closest to the slug (Figure 59). In the epoxy disk with pure carbon fibers, there were cracks throughout the surface. These cracks were divided into two different regions. The central area of the slice had a complex network of cracks running in all directions. In the outer region from the edge of the sample to the inner region, only radial cracks were present. This case was used as a baseline to compare other slices against. The nanoindentation testing showed that this case had the lowest modulus and hardness, so subsequent samples were expected to show improvement. The sulfurized fibers demonstrated performance only slightly improved. The central region of the puck was similar and axial cracks still formed. However, these cracks were restricted to sections of the sample and were not as widespread.



Figure 58. An image of the deform aluminum sample holder. The surface was initially flat, and the ring on the surface is a result of the displacement of metal from the impact of the 480 gram slug traveling at 370 meters per second.



Figure 59. Images of the epoxy slices with only carbon nanofibers, left, and sulfurized nanofibers, right, fired upon in the gas gun. The surfaces show signs of impact and provide information about the relative effectiveness of the nanocomposites.

The epoxy slices with the included tungsten disulfide showed mixed characteristics, yielding the least and most damaged samples. On the surface of the lowest tungsten disulfide loading, very little damage was visible. There was some evidence of cracking in the center of the sample, but most of the cracks appeared to be confined to the surface and did not penetrate into the sample (Figure 60). Additionally,

there were only a few radial cracks that propagated from the center of the slice. Of these surface cracks, only one was found to penetrate through the full thickness (Figure 61). The crack was straight, thin, did not branch out horizontally and instead propagated roughly perpendicular to the face of the slice. On the other hand, the highest loading of tungsten disulfide presented very different features. The surface of the slice showed the greatest number of deep cracks of any sample. While a larger number of small cracks were found in the center of the slice, these cracks formed into larger deeper structures nearer to the center of the sample than even the pure carbon nanofibers. Many of these cracks propagate to the edge of the sample, and were quite different than the thin straight crack found in the lowest loading. These cracks were wide, with distinct changes in direction and smaller cracks emanating from the junctions.

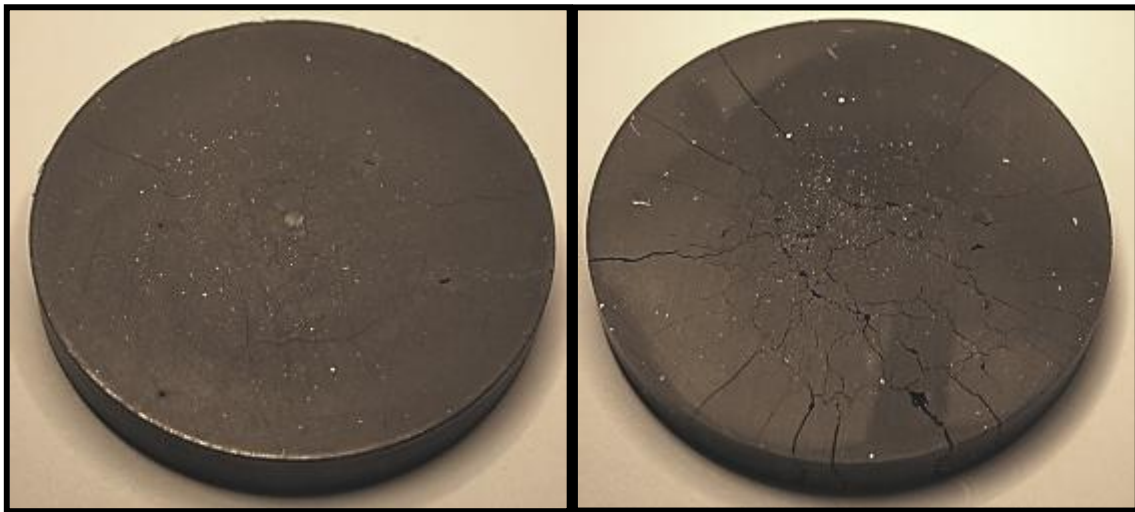


Figure 60. Images of the lowest and highest loadings of tungsten disulfide from left to right, respectively. The surface of the lowest loading shows little damage while the highest loading is heavily cracked.

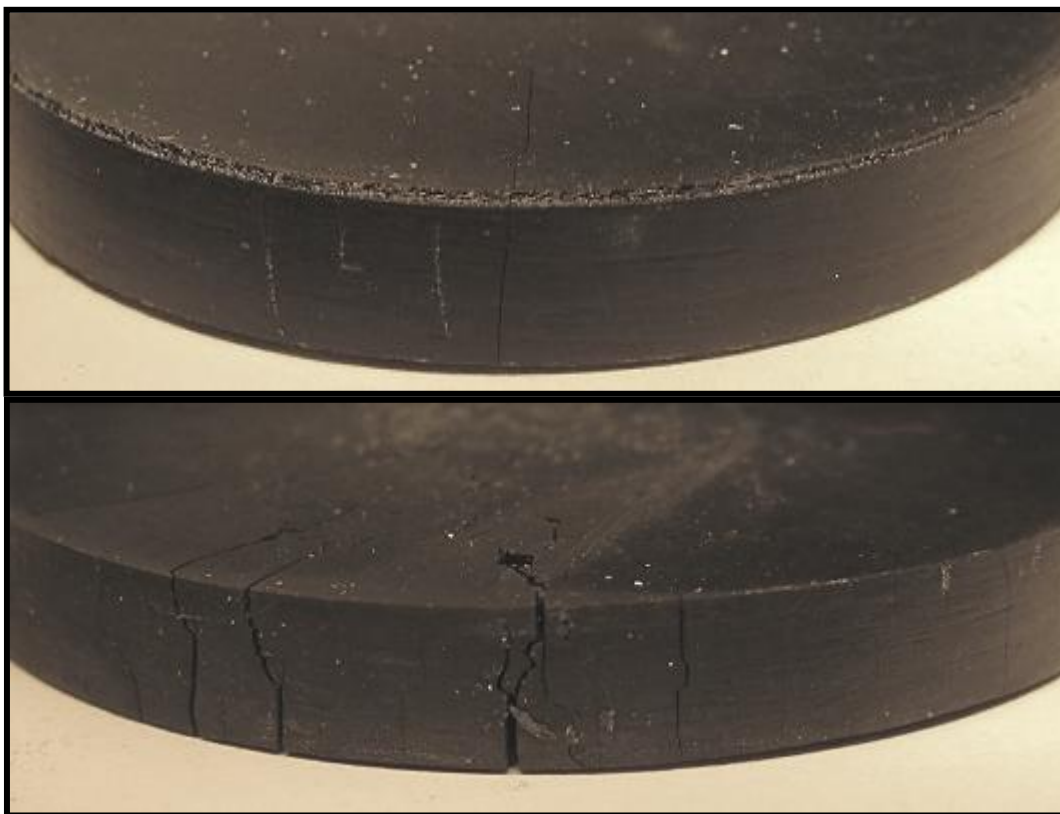


Figure 61. The upper image illustrates the crack that formed on the edge of the slice with the lowest loading of tungsten disulfide. The lower image illustrates the difference in the crack patterns found on cracks that reached the edge of the highest loading.

The improvement in the performance of the lowest loading could be a result of a number of different phenomenon or their combination. The inclusion of the carbon nanofibers could be providing a spring-like effect, absorbing the energy of the impact. While this effect relies heavily on interfacial strength, the sulfurization or inclusion of tungsten disulfide could increase adhesion between fibers and the epoxy. The bi-modal distribution of the fibers could also be playing an important role by inhibiting the propagation of shock waves through the material. The inclusion of tungsten disulfide also has a positive effect. The inclusion of multilayer hollow core inorganic fullerenes means that the structure can deform and reduce shock wave energy while at the same time shedding outside layers if the shear stress at the surface becomes too high. The ability to shed layers by breaking the weak inter-plane secondary bonding will increase the amount of energy that can be absorbed by the sample. This is in contrast to the strong covalent

bonds in-plane which maintain the integrity of the hollow cored structure. Finally, the small pockets of agglomerated tungsten disulfide particles may serve to dissipate lingering shock energy more effectively than a completely dispersed particle. The strengthening effects could also be tied to the modification of the crystalline structure of the epoxy as a result of the inclusion of a metallic sulfide as previously reported [33].

The difference in the two samples could be a product of many different factors. If the research showing that metallic sulfides promote the crystallization of epoxies can be applied in this case, it is possible that the differences in the materials were a result of a transition to a more brittle fracture mode. It was also possible that the reduction in the number of carbon nanofibers present in the sample, as a result of the larger mass fraction of tungsten disulfide, rendered the sample less able to transfer the load to the stronger nanofibers. Another option is that the tungsten disulfide particles are acting as stress concentrators. Finally, the impact of the nickel sulfide, despite evidence indicating an improvement in properties, still requires further study. XRD analysis of the two loadings showed that a transition in the morphology of the nickel sulfide occurs in between the highest and lowest loadings. This transition could lead to the formation of stress concentrations similar to what is found in tempered glass. SEM analysis of the cracks was conducted to gather more information about the fracture surfaces; however the nonconductive nature of the samples and the current inability to sputter conductive particles precluded this effort.

THIS PAGE INTENTIONALLY LEFT BLANK



## V. CONCLUSIONS

This research successfully synthesized a specifically engineered composite with demonstrated ability to maintain its integrity, while dissipating lingering shock fronts or pressure waves, by mechanisms related to the specific particulate structures and effects of mixed granularity. Overall, the addition of tungsten disulfide delivered a remarkable 70% contribution to the modulus and 133% contribution to the hardness over the values of the pure carbon nanofibers. As a result, this nanocomposite should continue to be explored. In particular, it is suggested that future research be focused on the determination of the mechanisms that are responsible for shock wave reduction.

Carbon nanofibers were successfully synthesized using a nickel nanoparticle catalyst. The main growth step occurred in a temperature of 550 degrees Celsius under an ethylene rich environment and the presence of oxygen. Additionally, a step at 350 degrees Celsius was added, under the same ethylene and oxygen environment, in order to plate the nickel with a thin layer of carbon preventing additional sintering of the catalyst. The carbon layer produced after the 350 degrees step was analyzed by SEM, EDX, and FIB milling cross-sections. Tungsten disulfide was grown and characterized using two synthesis methods, although only the growth using oxide precursors preserved the nanoscale features.

The direct inclusion of tungsten disulfide or tungsten salts *in situ* with the nickel nanoparticle catalyst resulted in the formation of nickel sulfide. This formation was experimentally observed to directly result in the cessation of the growth of carbon fibers.

The only viable *in situ* growth of carbon nanofibers and tungsten disulfide can be achieved using tungsten oxide as a tungsten source, nickel as a carbon growth catalyst and a sulfurization step to convert the former into tungsten disulfide once the fibers were grown from the catalyst particles.

Protocols were developed for the inclusion of the nanocomposites (carbon nanofiber and tungsten disulfide generated from Ni and tungsten oxide precursors) into an epoxy matrix. Carbon nanofibers mixed with tungsten disulfide acted as filler

materials. Dispersion of 1% weight of the filler into the epoxy was achieved through a combination of manual mixing and sonication. Three loadings of tungsten disulfide and carbon fiber nanocomposites were generated. These nanocomposites demonstrated mechanical properties and shock resistance greater than either of the constituent nanoparticles alone.

The nanocomposites were tested using nanoindentation while embedded into the epoxy matrix. For comparison, tested samples included an epoxy-only blank sample, one with only carbon fibers, one with fibers treated under sulfurization conditions but no tungsten oxide or sulfide, and the composites containing mixtures of carbon fibers and tungsten disulfide in 0.03%, 0.016% and 0.007% loadings by weight of the epoxy. Tests using two approximations (complex and basic modulus) under different operating conditions were used. These tests confirmed that the epoxy composites act in an elastic regime and the effects of frequency-dependent loss modulus can be neglected. As a result, the basic modulus and hardness testing was conducted using a Berkovich tip. The results illustrated increases in Young's modulus over the normalized epoxy (100%). The carbon fibers showed an increase of 29% over the epoxy, the sulfurized fibers a 52% increase, and the three loadings of tungsten disulfide a maximum increase of 99%. Likewise, and hardness increased with the addition of carbon nanofibers to 114% of the epoxy, the sulfurized fibers increased 152%, and the three loadings of tungsten disulfide a maximum increase 248%. It should be noted that the modulus for all three of the loadings of tungsten disulfide showed superior properties to any other tested variant.

High shock testing of the epoxy composites was also conducted and provided more insight into nanocomposite performance. In the epoxy with fibers only, and the epoxy with sulfurized fibers and not tungsten disulfide, a small region of distributed cracks was present in the center of the sample, while deeper radial cracks emanated from the central region. While the sulfurized fibers showed some reduction in cracking from the pure carbon nanofibers, the lowest loading of carbon fibers and tungsten disulfide composite showed marked improvement over any other tested sample. The majority of the cracks on the lowest loading appeared to be superficial and did not penetrate into the epoxy slice. Slight variability of results was observed for higher loadings.

## VI. RECOMMENDATIONS FOR FUTURE RESEARCH

Further work should also be conducted to quantify the change in morphology and the properties suffered by the carbon layers grown in the proximity of tungsten oxide particles. SEM images from this research provide evidence that there is a distinct growth mode in proximity to the tungsten oxide which needs to be further investigated.

A possible way to eliminate the complexity of the *in situ* growth and effects of nickel sulfide phases would be to grow the carbon nanofibers directly from a tungsten catalyst. At this point there is not a well-defined process to grow carbon fibers in this environment, but with future work the appropriate condition could be identified. If this is possible, the tungsten could be sulfurized via a process similar to the one used in the earlier sections.

The effect of the loadings of tungsten disulfide in the carbon nanofibers requires further quantification. While this research was conducted to determine a general viability, the few loadings tested do not provide an appropriate measure of the range of beneficial and detrimental effects or accurately identify a level of maximum performance. To find the optimal loading samples could be prepared by varying the loading at a predetermined interval and then subjected to analysis via nanoindentation.

A similar pursuit could be conducted while varying the amount of loading in the epoxy. While this research set the loading at one weight percent, there are a number of sources in the literature that used different loadings of materials into an epoxy matrix and achieved results across a wide range of loadings. It is very possible that modifying this loading slightly could result in a marked change in material performance.

The effects of nickel sulfide are also not well characterized. While it is known to be a contaminant in glass, it is also entirely plausible that its inclusion is providing a beneficial effect in epoxy matrixes. The sulfurized fibers did perform better than the pure fibers in nanoindentation and gas gun testing, which suggests that the inclusion of nickel sulfide is contributing to a larger modulus, hardness, and better shock absorption.

The gas gun testing in this research was only useful for the empirical determination of energy absorption via visible cracking. In the future, the gas gun will be instrumented to determine the change in the shock pressure after passing through a material. This will provide the most accurate measurement of the effectiveness of the shock absorbing characteristics of the material. The shock impedance for these materials is different from the utilized values on a fundamental level. In order to understand the conditions that the material is actually exposed to during testing, accurate values for these numbers are essential.

A final recommendation is to continue the postmortem analysis of epoxy materials subjected to gas gun tests to determine the effects of shock waves on the particles. This was attempted with SEM observation of the samples after gas gun tests, but charging issues prevented analysis. Once the correct conditions were met, this method could be used to identify why some regions cracked while others did not and also to determine if tungsten disulfide or nickel sulfide are acting as stress concentrators. This could also be accomplished by dissolving the epoxy and reviewing the damage to the nanocomposite in SEM or TEM.

## LIST OF REFERENCES

- [1] H. Robinson, *Oriental Armor*. New York: Dover Publications, 2002.
- [2] N. David, X.-L. Gao and J. Zheng, "Ballistic Resistant Body Armor: Contemporary and Prospective Materials and Related Protection Mechanisms," *Applied Mechanics Reviews*, vol. 62, no. 5, 2009.
- [3] Stanford Mechanical Engineering, "Army High Performance Computing Research Center," Stanford University, 1997–2012. [Online]. Available: <http://me.stanford.edu/research/centers/ahpcrc/TA1Images.html> [accessed 27 May 2012].
- [4] L. Wang, J. Lau, E. J. Thomas and M. C. Boyce, "Co-Continuous Composite Materials for Stiffness, Strength, and Energy Dissipation," *Advanced Materials*, no. 23, pp. 1524–1529, 2011.
- [5] E. W. Wong, P. E. Sheehan and C. M. Lieber, "Nanobeam Mechanics: Elasticity, Strength, and Toughness of Nanorods and Nanotubes," *Science*, vol. 277, pp. 1971–1975, 1997.
- [6] M. Treacy, T. Ebbesen and J. Gibson, "Exceptionally high Young's modulus observed for individual carbon nanotubes," *Nature*, vol. 381, pp. 678–680, 1996.
- [7] K. Mylvaganam and L. Zhang, "Ballistic resistance capacity of carbon nanotubes," *Nanotechnology*, vol. 18, 475701, 2007.
- [8] R. Tenne, "Inorganic Fullerene-Like Structures-IFS." Tel Aviv: The Israel Chemical Society.
- [9] R. Tenne, M. Homyonfer and Y. Feldman, "Nanoparticles of layered compounds with hollow cage structures," *Chemistry of Materials*, no. 10, pp. 3225–3238, 1998.
- [10] A. Margolin, R. Rosentsveig and A. Albu-Yaron, "Study of the growth mechanisms of WS<sub>2</sub> nanotubes produced by a fluidized bed reactor," *Journal of Materials Chemistry*, no. 14, pp. 617–624, 2004.
- [11] I. Kaplan-Ashiri and R. Tenne, "Mechanical Properties of WS<sub>2</sub> nanotubes," *Journal of Cluster Science*, no. 18, pp. 549–563, 2007.
- [12] R. Rosentsveig, A. Margolin, Y. Feldman, R. Popovitz-Biro and R. Tenne, "Bundles and Foils of WS<sub>2</sub> Nanotubes," *Applied Physics A*, no. 74, pp. 367–369, 2002.
- [13] M. Tehrani, C. C. Luhrs, M. Al-Haik, J. Trevino and H. Zea, "Synthesis of WS<sub>2</sub> nanostructures from the reaction of WO<sub>3</sub> with CS<sub>2</sub> and mechanical characterization of WS<sub>2</sub> nanotube composites," *Nanotechnology*, no. 22, 285714, 2011.
- [14] Y. Q. Zhu, T. Sekine, B. S. Kieren, S. Firth, R. Tenne, R. Rosentsveig, H. W. Kroto and D. R. Walton, "Shock-Wave Resistance of WS<sub>2</sub> Nanotubes," *Journal of the American Chemical Society*, vol. 125, pp. 1329–1330, 2003.

- [15] C. C. Luhrs, D. Garcia, M. Tehrani, M. Al-Haik, M. R. Taha and J. Phillips, "Generation of carbon nanofilaments on carbon fibers at 550 C," *Carbon*, vol. 47, pp. 3071–3078, 2009.
- [16] M. A. Atwater, J. Phillips and Z. C. Leseman, "Formation of Carbon Nanofibers and Thin Films Catalyzed by Palladium in Ethylene-Hydrogen Mixtures," *Journal of Physical Chemistry*, no. 114, pp. 5804–5810, 2009.
- [17] R. I. Walton and S. J. Hibbe, "A combined in situ W-ray absorption spectroscopy and X-ray diffraction study of the thermal decomposition of ammonium tertathiotungstate," *Journal of Materials Chemistry*, vol. 96, no. 6, pp. 1347–1355, 1999.
- [18] S. Sun, Z. Li and X. Chang, "Synthesis and Structural Characteristics of Tungsten Disulfide Nanomaterials," *Materials Letters*, vol. 65, no. 19–20, pp. 3164–3166, October 2011.
- [19] S. Sun, Z. Zou and G. Min, "Synthesis of tungsten disulfide nanotubes from different precursor," *Materials Chemistry and Physics*, no. 114, pp. 884–88, 2008.
- [20] S. Zhang, L. Li and A. Kumar, *Materials Characterization Techniques*. Boca Raton, FL: CRC Press, 2009.
- [21] Quantachrome Instruments, *NOVA Operation Manual; High Speed Gas Sorption Analyzer Version 11.02*. Boynton Beach, FL: Quantachrome Instruments, 2009.
- [22] G. Pharr, W. Oliver and F. Brotzen, "On the Generality of the Relationship among Contact Stiffness Contact Area and Elastic Modulus During Indentation," *Materials Research Society*, vol. 7, no. 3, pp. 613–617, March 1992.
- [23] "Nanoindenters From Micro Star Technologies," Mirco Star Technologies, [Online]. Available: <http://www.microstartech.com/> [accessed 25 April 2012].
- [24] J.L. Hay, "Measuring the Complex Modulus of Polyethylene Using Instrumented Indentation," Knoxville: Agilent Technologies, 2011.
- [25] G. Odegard, T. Gates and H. Herring, "Characterization of Viscoelastic Properties of Ploymeric Materials through Nanoindentation," *Society for Experimental Mechanics*, vol. 45, no. 2, pp. 130–136, April 2005.
- [26] C. C. Ho, "Assembly and commissioning of Naval Postgraduate School gas gun for impact studies," M.S. thesis, Naval Postgraduate School, Monterey, CA, 2009.
- [27] J. P. Hooper, Asst. Professor, Interviewee, *Shock Physics* [Interview]. 14 May 2012.
- [28] J. Sehested, J. A. Gletten and S. Helveg, "Sintering of nickel catalysts: Effects of time, atmosphere, temperature, nickel-carrier interatction, and dopants," *Applied Catalysis*, no. 309, pp. 237–246, 2006.

- [29] P. Waldner, "ASM International Alloy Phase Diagrams Center; Ni-S Phase Diagram," 2004. [Online]. Available from [www.asminternational.org](http://www.asminternational.org) [accessed 14 December 2012].
- [30] A. Dutta and D. Penumadu, "Nanoindentation Testing for Evaluating Modulus and Hardness of Single Walled Carbon Nantube-Reinforced Epoxy Composites," *Materials Research Society*, vol. 19, no. 1, pp. 158–164, January 2004.
- [31] Y. Zhou, F. Pervin, V. K. Rangari and S. Jeelani, "Fabrication and Evaluation of Carbon Nano Fiebr Carbon/Epoxy Composite," *Materials Science and Engineering:A*, vol. 426, no. 1–2, pp. 221–228, 2006.
- [32] K. Gromowski, "Glass Breakage - Nickel Sulfide Inclusions," Penn State, 2010. [Online]. Available: <http://failures.wikispaces.com> [accessed 30 April 2012].
- [33] C. Long and M. Hua, "Study of POM Composites Modified by Ekonol and Lubricant," *Journal of Thermoplastic Composite Materials*, vol. 18, no. 5, pp. 381–391, 2005.

THIS PAGE INTENTIONALLY LEFT BLANK



## **INITIAL DISTRIBUTION LIST**

1. Defense Technical Information Center  
Ft. Belvoir, Virginia
2. Dudley Knox Library  
Naval Postgraduate School  
Monterey, California